Linear and Nonlinear Waves in Magneto-granular Phononic Structures : Theory and Experiments

Florian Allein

UNIVERSITE BRETAGNE LOIRE

Université du Maine

Thèse de Doctorat

Florian Allein

Mémoire présenté en vue de l'obtention du
grade de Docteur de l'Université du Maine
sous le sceau de L'Université Bretagne Loire

École doctorale : SPIGA

Discipline : 60
Spécialité : Acoustique
Unité de recherche : Laboratoire d'Acoustique de l'Université du Maine - UMR CNRS 6613

Soutenue le 14 juin 2017
Thèse N°: 98676

Linear and Nonlinear Waves in Magneto-Granular Phononic Structures: Theory and Experiments

JURY

Rapporteurs :	**N. Boechler**, Assistant Professor, University of Washington (USA)
	V. Sánchez-Morcillo, Professor, Polytechnical University of Valencia (Spain)
Examinateurs :	**A.-C. Hladky-Hennion**, Directrice de recherche CNRS, IEMN - University of Lille 1
	S. Job, Maître de Conférences, SUPMECA Paris
	V. Magnanimo, Assistant Professor, University of Twente (Netherlands)
Invité :	**P. Béquin**, Maître de Conférences, LAUM - Le Mans University
Directeur de thèse :	**V. Tournat**, Directeur de recherche CNRS, LAUM - Le Mans University
Co-directeur de thèse :	**V. Gusev**, Professeur, LAUM - Le Mans University
Encadrant de thèse :	**G. Theocharis**, Chargé de recherche CNRS, LAUM - Le Mans University

Académie de Nantes

Université du Maine, Le Mans, France
École Doctorale Sciences pour l'Ingénieur, Géosciences, Architecture

Doctoral Thesis
Speciality : Acoustics

Presented by
Florian ALLEIN
submitted for the Doctoral degree

Linear and Nonlinear Waves in Magneto-Granular Phononic Structures: Theory and Experiments

---

Defended on June 14th, 2017
Members of the committee:

N. Boechler	Assistant Professor, University of Washington (USA)	*Reviewer*
V. Sánchez-Morcillo	Professor, Polytechnical University of Valencia (Spain)	*Reviewer*
A.-C. Hladky-Hennion	Directrice de recherche CNRS, IEMN - University of Lille 1	*Examiner*
S. Job	Maître de Conférences, SUPMECA Paris	*Examiner*
V. Magnanimo	Assistant Professor, University of Twente (Netherlands)	*Examiner*
P. Béquin	Maître de Conférences, LAUM - Le Mans University	*Examiner*
V. Tournat	Directeur de recherche CNRS, LAUM - Le Mans University	*Thesis supervisor*
V. Gusev	Professeur, LAUM - Le Mans University	*Thesis co-supervisor*
G. Theocharis	Chargé de recherche CNRS, LAUM - Le Mans University	*Thesis co-supervisor*

To Laura

Acknowledgements

This work achieved during this thesis cannot be carry out on its own, thus I would like to thank the people who have given me their support throughout this project. First of all, I would to thank my thesis advisors, Vincent Tournat, Vitali Gusev, and Georgios Theocharis for having proposed to me this thesis subject, their availability and given me the opportunity to shape my own PhD research. Although this work deals with ordered media, I would like to thank again Georgios Theocharis for having taught me disordered media, often unintentionally, in the experimental room.

I would like to acknowledge Nicholas Boechler and Victor Sánchez-Morcillo for having agreed to be reviewers of this thesis. I would also like to acknowledge Anne-Christine Hladky-Hennion, Stéphane Job, and Vanessa Magnanimo for having agreed to be member of my PhD committee as well as for giving me very pertinent comments on my work. I would like to thank Philippe Béquin and a second time Stéphane Job for having taken part of my "comité de suivi de thèse" and for the interesting discussion around the doctoral thesis in general.

This thesis is largely an experimental work so I would like to thank Emmanuel Brasseur, James Blondeau, and Stéphane Lebon for the help provided during the set-up of the experiments, their availability and their responsiveness to my requests (sometimes unexpected). I would also like to thank Antonin Novak for sharing with me his knowledge on signal processing. Most of the experimental devices have been built by Hervé Mézière, Éric Egon, and Jacky Maroudaye, I would like to thank them for the quality of their work.

Over the last four years, it was a real pleasure to work in great environment and I would like to thank all the LAUM members for the convivial atmosphere of work with a special acknowledgements to the granular team and the colleagues in the experimental room: Aurélien, Laurianne, Stephane, and Alejandro for their good moon and fruitful discussions.

I would also thank my (former and new) office mates: Ludovic, Jérémy, Wei, Xinxin, and Liyang "le beau gosse", for having shared great moments as well as Aroune, Jean-Philippe, Vicent, Olivier, Vassos, Gaëlle, Charlie, for the good vibes, daily motivation and discussions (sometimes scientific). I thank all the other PhD students and post-doc who have walked alongside me through my thesis.

I would like to acknowledge the active members of the acoustician network of Le Mans (RAmDAM): Thibaut, Julien, Margaux, Léo, Océane, Sylvain, Antoine, Léo, Elie, Thibault, Cédric, "captain" Rodrigue, Théo, Meryem for their great effort to create cohesion between acousticians.

To Murielle and Rachida, thank for all theses coffee breaks with the happiness and smile. This work would have been much harder without you.

To Thibaut and Cédric who are much more than colleagues but friends, I thank them warmly for their support and the fun they gave me. Get ready for business in *Tiger's Cheese Cie* and stay awesome!

I thank all my family for their support throughout all my graduate studies and especially for the last stressful and tremendous year since two doctors appeared in the family. I am truly proud to be able to say: "Chère consoeur!".

Last but not least, I would never thank Laura enough for her unwavering support, patience, and the force she gave me throughout this journey.

An expert is a man who has made all the mistakes
which can be made in a narrow field.
Niels Bohr

Contents

List of notations **v**

General Introduction **1**

1 Acoustic wave propagation in granular phononic crystals **5**
1.1 Introduction . . . 6
1.2 Periodic phononic structures . . . 7
1.2.1 Phononic granular crystals . . . 8
1.3 Importance of rotational degrees of freedom . . . 12
1.4 Mechanical description of the contact between particles . . . 14
1.5 One-dimensional granular crystals . . . 17
1.5.1 Near linear regime . . . 18
1.5.2 Weakly nonlinear regime . . . 18
1.6 Longitudinal normal modes in a one dimensional monoatomic granular crystal . . . 20
1.7 Magnetic description of the magneto-granular phononic crystal . . . 23
1.7.1 Magnetic field created by one magnet . . . 23
1.7.2 Magnetic field induced by several magnets and beads . . . 26
1.8 Conclusion . . . 29

2 Tunable magneto-granular phononic crystals **31**
2.1 Introduction . . . 32
2.2 Theory of infinite linear granular chain considering 6 degrees of freedom . . . 33
2.2.1 Equations of motion for sagittally polarized modes . . . 34
2.2.2 Equations of motion for horizontally polarized modes . . . 35
2.2.3 "Free" linear granular chain . . . 38
2.2.4 Linear granular chain coupled with a rigid substrate . . . 40
2.2.5 Summary . . . 43
2.3 Linear spectra : experimental results and discussion . . . 44
2.3.1 "Free" linear granular chain . . . 45
2.3.2 Tunable "Free" linear granular chain by external magnetic fields . . . 47
2.3.3 Linear granular chain coupled with a rigid substrate . . . 48
2.3.4 Summary . . . 51
2.4 Experimental and numerical dispersion curves . . . 53

2.4.1 Characterization of the experimental driver . . . 53
2.4.2 Modeling of the finite linear granular chain . . . 55
2.4.3 Experimental dispersion curve method and setup configuration . . . 56
2.4.4 Results and discussion . . . 58
2.4.5 Summary . . . 64
2.5 Conclusion . . . 66

3 Linear and nonlinear wave propagation 67
3.1 Introduction . . . 68
3.2 Linear propagation of packets and continuous harmonic waves . . . 69
3.2.1 Longitudinal wave propagation: experiments vs numerics . . . 69
3.2.2 Transverse-Rotational wave propagation: experiments vs numerics . . . 73
3.2.3 Summary . . . 79
3.3 Second harmonic generation in a finite granular chain . . . 81
3.3.1 Numerical analysis . . . 81
3.3.2 Experimental observation of the second harmonic generation . . . 84
3.3.3 Frequency analysis in different dynamical regimes . . . 87
3.3.4 Summary . . . 89
3.4 Γ-shaped granular chain: mode conversion and harmonic filtering . . . 91
3.4.1 Principle of conversion from longitudinal to coupled transverse-rotational modes . . . 92
3.4.2 Experimental Γ-shaped chain . . . 93
3.4.3 Summary . . . 98
3.5 Conclusion . . . 99

General conclusion 101

A Additional experiment and simulations of magnetic field 105

B Experimental dispersion curves for a linear granular chain coupled to a substrate 111

Bibliography 115

List of notations

x, y, z	Axes and coordinates
$\hat{e}_{x,y,z}$	Unit vectors
$\hat{\tau}$	Normal unit vector
D	Distance between magnet and the center of the beads (m)
R_c	Radius of the magnet (m)
m	Mass of the sphere (kg)
I	Momentum of inertia (kg·m^2)
R	Radius of the sphere (m)
h	Height of the magnet (m)
a	Lattice constant (m)
r_c	Radius of the contact surface (m)
δ_0	Relative normal displacement (static overlap) (m)
δ_t	Relative tangential displacement (static overlap) (m)
δ	Driven displacement (m)
μ_f	Friction coefficient
G	Shear modulus (Pa)
E	Young's modulus (Pa)
ν	Poisson's ratio
E^*	Normalized Young's modulus (Pa)
G^*	Normalized shear modulus (Pa)
R^*	Equivalent radius (m)
A	Coefficient representing the contact
ρ	Density (kg/m^3)
L_m	Half height of the magnet (m)
l_m	Half width of the magnet (m)
$B_{0x,y}$	Magnetic field by components (T)
B_0	Total magnetic field density (T)
$B_{1x,y_{out}}$	Magnetic field by components outside the permanent magnet (T)
$B_{1x,y_{in}}$	Magnetic field by components inside the permanent magnet (T)
B_1	Total magnetic field density considering a perturbation (T)
σ^*	Surface charge density of the magnet (T)
μ_0	Vacuum permeability constant
μ_{air}	Relative permeability of the air
μ_m	Relative permeability of the magnet
B_r	Remanent magnetization (T)
T_0	Static tangential force (N)
F_0	Static normal force between spheres (N)
F	Static normal force between spheres and magnets (N)

K_N	Normal stiffness between spheres (N/m)
K_S	Shear stiffness between spheres (N/m)
K_T	Torsional stiffness between spheres (N · m)
$\tilde{K}_N$	Normal stiffness between spheres and half-space (N/m)
$\tilde{K}_S$	Shear stiffness between spheres and half-space (N/m)
$\tilde{K}_T$	Torsional stiffness between spheres and half-space (N · m)
K_g, K'_g	Normal and shear stiffness fitted for the glue contact(N/m)
τ_g, τ'_g	Normal and shear dissipative parameter for the glue contact (s)
τ, τ'	Normal and shear dissipative parameter (s)
η_1	Ratio between stiffnesses: K_N/K_S
η_2	Ratio between stiffnesses: $\tilde{K}_S/K_S$
η_3	Ratio between stiffnesses: $\tilde{K}_N/K_S$
η_4	Ratio between stiffnesses: $K_T/(K_S R^2)$
η_5	Ratio between stiffnesses: $\tilde{K}_T/(K_S R^2)$
p	Mass distribution in the spherical particle : $(mR^2)/I$
q	Ratio between normal and shear rigidities : $ka/2$
u	Displacement from the equilibrium position (m)
$\dot{u}$	First time-derivative, Velocity (m/s)
$\ddot{u}$	Second time-derivative, Acceleration (m/s^2)
ϕ	Angle of rotation (rad)
$\mathbf{V}^{\mathbf{s},\mathbf{H}}$	Plane waves solution
$\mathbf{D}^{\mathbf{s},\mathbf{H}}$	Dynamical matrix
$\mathbf{v}^{\mathbf{s},\mathbf{H}}$	Amplitude vector
Ω	Normalized frequency
ω	Cyclic frequency (rad/s)
ω_0	Linear cutoff frequency (rad/s)
k	Wavenumber (rad/m)
k_r, k_i	Real and imaginary part of the wavenumber (rad/m)
λ	Elastic length, distance between asperities
φ, θ	Angle of the vibrometer with the chain
c_{L_ϕ}	Phase velocity of longitudinal waves (m/s)
$c_{L_{gr}}$	Group velocity of longitudinal waves (m/s)
c_{T_ϕ}	Phase velocity of transversal-rotational waves (m/s)
$c_{T_{gr}}$	Group velocity of transversal-rotational waves (m/s)
$\mathcal{L}_{\mathbf{s},\mathbf{H}}$	Lagrangian
$T_{\mathbf{s},\mathbf{H}}$	Kinetic energy
$V_{\mathbf{s},\mathbf{H}}$	Potential energy
α	Generalized coordinate
$\dot{\alpha}$	First time-derivative of the generalized coordinate
ΔL	Normal spring elongations
ΔS	Shear spring elongations
ΔT	Torsional spring elongations
$f_{L,TR,R}$	Cutoff frequency at $k = 0$ (Hz)
$f'_{L,TR,R}$	Cutoff frequency at $k = \pi/a$ (Hz)
$\Omega_{L1,T2}$	Normalized cutoff frequency in the Γ-shaped chain
$\Omega_{1,2,3}^{\mathbf{s},\mathbf{H}}$	Normalized cutoff frequency at $k = 0$
$\Omega_{1,2,3}^{\mathbf{s}',\mathbf{H}'}$	Normalized cutoff frequency at $k = \pi/a$
Δk	Detuning parameter

General introduction

The ability to control the propagation of elastic waves has been widely investigated in phononic crystals, a class of engineered media composed of periodic arrays of scattering inclusions in a homogeneous host material [1]. The propagation of sound in phononic crystals is driven by the interference between Bragg scattered waves. Similar to the electronic band structure of semiconductors and the electro-magnetic band structure of photonic crystals, the phononic crystal structure does not allow certain frequency ranges to propagate within it. The existence of these forbidden bands makes phononic crystals suitable for direct applications, such as mechanical frequency filtering and sound insulation. In addition, the removal of inclusions along some pathways produces acoustic waveguides, demultiplexers, and other elastic wave devices. To foresee the next generation of elastic devices, it would be necessary to introduce a certain degree of frequency tunability in the phononic properties. Greater interest has been shown along these lines over the last few years, and many solutions have been proposed by a number of authors; these include geometric changes to the structure by applying external stresses [2] and changes to the elastic characteristics of the constitutive materials through application of external stimuli, like an electric field [3], temperature changes [4], or a magnetic field [5].

Granular phononic crystals, namely ordered granular media made of elastic particles such as spheres, are a type of phononic crystals with some very interesting features. A key point when considering granular phononic crystals is the fact that contact forces between particles are applied at a radius distance from the center of mass, leading in many configurations to the application of moments to the particles, due to non central forces, in addition to central forces. Then, the rotational motion of the particles is excited and the associated degrees of freedom should be accounted for, together with the translational degrees of freedom, in the description of wave propagation and dispersion. Elasticity of granular materials differs from the classical elasticity due to the micro-structured characteristic of the assembly. In the classical elasticity of materials, the rotation of infinitesimal elements is not considered. A generalization of the classical theory of elasticity accounting for rotation, called Cosserat theory or micropolar theory, has been proposed by the Cosserat brothers in 1909 [6]. The Cosserat formalism has been adapted to the description of granular media only from the 1980s. Compared to the variety of theoretical developments, including rotational degrees of freedom where coupled rotational-translational modes have been predicted, experimental studies and evidence of the rotational and coupled rotational-translational modes of propagation are only very few. Transversal-rotational modes of propagation have been identified experimentally in a three-dimensional hexagonal compact arrangement of mm-size spheres in Ref. [7]. In this case, the propagation

along the high symmetry 6-axis of the crystal exhibits a specific dispersion with an isolated frequency band of propagation for rotational-transverse modes. Furthermore, the importance of micro-rotations has been recently theoretically and experimentally revealed also in colloidal-based metamaterials [8, 9] and in torsional waves in granular chains [10].

Another key point of the granular phononic crystals is their tunable dynamical response stemming from the contact nonlinearity. Not only their linear elastic properties are found dependent on the externally applied static force but also their elastic behavior can range from near linear to highly nonlinear, by modifying the ratio of static to dynamic inter-particle displacements [11]. Consequently, due to this especially appealing dynamic response, granular phononic crystals have recently played a key role in the study of fundamental wave phenomena, including solitary waves with a highly localized waveform in the case of uncompressed crystal, discrete breathers and others [12–17]. They have been also applied in various engineering devices, including among others shock and energy absorbing layers [18–20], acoustic lenses [21], and acoustic rectifiers [22, 23].

In this thesis, we extend the studies of granular phononic crystals by designing and studying magneto-granular phononic structures. These are composed of linear chains of spherical steel beads inside a designed magnetic field induced by permanent magnets. The external magnetic field offers not only a great advantage of straightforward construction but also a non-contact tunability via its magnetic field strength. For the theoretical description of the dynamics of the granular chains, we consider all the six degrees of freedom, i.e. three translations and three rotations. This modeling provides the dispersion relation of the modes showing the presence of coupled rotational-transversal modes. Linear and nonlinear wave propagation through such structures is studied by numerical simulations together with experimental measurements. Interesting wave phenomena, such as the elastic wave propagation in the presence of micro-rotations, the harmonic generation, the harmonic filtering with conversion from longitudinal to coupled transversal-rotational modes are experimentally demonstrated.

Parts of this presented work have been extracted from published articles in *Applied Physics Letters* [24] and *Extreme Mechanics Letters* [25].

This manuscript is composed of three chapters. A non-exhaustive review of the studies on periodic media as well as on granular phononic crystals is presented in the first chapter. Some basic notions useful for the understanding and the description of the wave propagation in a granular phononic crystal together with the importance of rotational degrees of freedom of the particles are also exposed. Finally, we present in details the magneto-granular experimental setup and we mention the advantage and the possibility to create attractive forces between particles via the application of an external magnetic field.

In the second chapter, a linear theory describing the three-dimensional dynamics of a granular chain is proposed by considering different coupling parameters between beads and the substrate providing the dispersion relation of the modes. Evidence of the elastic wave propagation with micro-rotation is experimentally demonstrated, confirming the theoretical model. In addition, tunability of the dynamical

response of the chain by external magnetic fields is also experimentally reported, and numerical and experimental dispersion curves are successfully derived.

In the third chapter, linear and nonlinear wave propagation through a one-dimensional granular chain and a Γ-shaped granular structures is numerically and experimentally studied. In the linear regime, the comparison between experimental and numerical results permits to better estimate the precompression force in the chain along with the estimation of the losses depending on the polarization of the wave propagation. In the weakly nonlinear regime, predictions and experimental observation of the second harmonic generation are performed. Finally, the filtering of harmonics along with conversion from longitudinal to coupled transversal-rotational modes in Γ-shaped granular structures, is also reported.

Chapter 1

Acoustic wave propagation in granular phononic crystals

Contents

1.1 Introduction 6
1.2 Periodic phononic structures 7
1.2.1 Phononic granular crystals 8
1.3 Importance of rotational degrees of freedom 12
1.4 Mechanical description of the contact between particles 14
1.5 One-dimensional granular crystals 17
1.5.1 Near linear regime 18
1.5.2 Weakly nonlinear regime 18
1.6 Longitudinal normal modes in a one dimensional monoatomic granular crystal 20
1.7 Magnetic description of the magneto-granular phononic crystal 23
1.7.1 Magnetic field created by one magnet 23
1.7.2 Magnetic field induced by several magnets and beads 26
1.8 Conclusion 29

1.1 Introduction

Granular phononic crystals are periodic arrangements of elastic particles in contact which can be made of different materials, shapes, and sizes. In general, granular media are biphasic since they are composed of a solid phase, the elastic particles, and a fluid phase saturating the pores between the particles. When one considers the elastic wave propagation in granular media, the coupling between the particles and the surrounding fluid is often neglected due to the large impedance and mass difference between the two media.

This first chapter introduces a set of notions, phenomena and behavioral description of granular materials useful for the understanding of theoretical and experimental results presented thereafter. First sections of this chapter presents a non exhaustive state of the art from researches on periodic structures and granular phononic crystals giving the context of this study. In particular, the importance of the rotational degree of freedom in the dynamical description of granular structure is discussed. The macroscopic behavior of a granular assemblies depends on the mechanical interaction at the microscopic scale between the particles. The modeling of this interaction by the Hertz-Mindlin theory, presented in the fourth section, is an essential basis of the physics of granular materials. The general equations for the longitudinal motion of a granular chain are described based on the full Hertzian model showing the potential nonlinear behavior of such structures. Then, the physical properties related to the periodic structure of a granular crystal are described in the simple case of a one-dimensional monoatomic chain showing basic behavior such as the dispersion of the wave velocity as a function of the frequency. Finally, the magneto-granular experimental setup is detailed by briefly introducing the advantage and the possibility to create attractive forces between particles via the application of an external magnetic field.

1.2 Periodic phononic structures

Major technological innovations in recent decades have been based principally on the ability to manipulate two particles: electrons and photons. The control of electrons in semi-conductor materials has given rise to considerable changes for electronic devices such as laptops, mobile phones, cameras. On another side, the control of photons has lead to wireless communication, use of optical fiber and microwaves. In addition to electrons and photons, another particle that we experience in our daily life is the phonon, which is responsible for the transmission of sound and heat. The verbal human communication is based on the propagation of audible acoustic waves while many imaging devices for medicine and industry are involving ultrasonic waves. Nevertheless, the control of waves remains a challenge in all these domains. Thus, in the aim of the control of waves, the design and engineering of artificial materials with more complex properties can provide unprecedented behaviors and functionalities. These artificial structures, usually periodic, are composed of elements that can behave like a continuous material with unconventional effective properties. Thenceforth, numerous studies have focused on the understanding of the propagation of classical waves through periodic structures. These periodic structures are called phononic crystals for elastic/acoustic (phonon) waves, and photonic crystals for electromagnetic (photon) waves. Example of a three dimensional phononic structure is presented in Fig. 1.1.

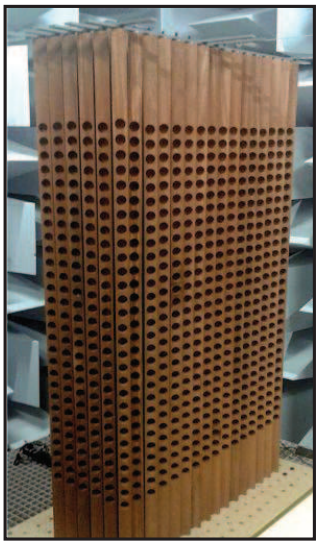

Figure 1.1: Example of a 3D phononic crystal made of square-rod rigid scatterers incorporating a periodic arrangement of quarter wavelength resonators [26].

The most common phenomenon presents in such structures is the presence of forbidden band of propagation, also called band gap. These band structures arise from the wave diffraction by the periodic structure and constructive or destructive interference as a function of the wave frequency. Waves with frequency inside a band gap can not propagate through the crystal, their energy is reflected by it. Band gap in photonic crystals is due to a periodic variation of the refractive index of the structured material whereas in phononic crystals the density and/or elastic constants of the material are varying periodically. There are important differences between mechanical and electromagnetic waves. Photons can propagate through vacuum while phonons can not. In addition, the light can have two independent polarizations whereas an elastic wave in a homogeneous solid has three independent polarizations: two transverse (shear waves) and one longitudinal (compressional wave). Nevertheless, since shear waves are not supported by liquids and gases, an acoustic wave has only one longitudinal polarization. One of the advantages of acoustics in comparison with optical and electronic domains lies in the possibility of observing the effects of elastic band gaps over wide frequency ranges, allowing the design of macroscopic devices and thus widening their field of application.

The concept of phononic crystals has been introduced quasi simultaneously by Kushawa et al. [27] and Economou and Sigalas [28, 29] in 1993. They have shown band structures due to the periodicity in two and three-dimensional structures leading to possible engineering applications such as acoustic insulator, anti-seismic structures or filtering... The first experimental demonstration of the effect of a phononic structure on the propagation of sound was carried out on a minimalist sculpture created by the Spanish artist Eusebio Sempere exposed in Madrid (Spain) [30]. This structure is composed of a two-dimensional periodical arrangement of steel tubes in air. They have observed a decrease in the level of the transmitted signal at the output of the sculpture (at a certain range of frequencies) not due to absorption but due to multiple scattering of sound waves due to the arrangement of the tubes in a periodic square array. They have found band gaps which are existing only for a defined direction of the wave propagation through the structure. Thus this work was followed by further experimental studies, on designed two-dimensional periodic composite, where complete band gaps are exhibited [31–33] meaning that band gaps are present for all directions of the wave propagation in the structure. Besides the band gap effect, other wave guide phenomena can occur in phononic structures as for example negative refraction [34], focusing [35] and cloaking effects [36, 37]. All these phenomena in phononic structures are studied in the linear regime of propagation, however as the amplitude of the wave excitation is increased the response can become nonlinear leading to more complex phenomena with no analogs in linear theory.

Nonlinearity in phononic materials can originate from two kinds of sources. The first one, called intrinsic, is a nonlinearity coming from the material constitutive response such as for example interatomic forces, nonlinear elasticity, or plasticity. The second one, called extrinsic, originates from the geometry of the designed structure as for example contact force between particles [38], deformation of micromechanical and nanomechanical oscillators and resonators [39], or geometric instabilities. A classical type of nonlinear periodic phononic structures is the granular crystals which are arrays of elastic particles in contact. The next section focuses on these granular structures.

1.2.1 Phononic granular crystals

Granular materials are composed of elastic particles exchanging forces and momenta through their geometric contact interactions. The particles can be made of different materials, sizes, and shapes which affect the particle interactions and thus the bulk mechanical response of this material. These materials are found in many industrial sectors such as in civil engineering (concrete), in chemical industry (fuels and catalysts are often in the form of grains to maximize exchange), in pharmaceutical industry (manipulation of powders for the manufacture of medicines), in food-processing (cereals, animal feed). In all these sectors there are problems of storage, transport, flow, mixing, transformation (grinding), to which the industries have responded by clever but often empirical methods. Another area where granular media are present is geophysics, the soil being mainly a medium formed of grains. Situations involving this environments include: dunes, landslides, snow avalanches. The description of these events and the prediction of disasters such as landslides require a good understanding of the flow properties of these media. In order to high-

light the complexity in the description of granular media, we can give one simple example; a teaspoon of powdered sugar can contain about one hundred thousand grains. To describe such media, the number of particles becomes problematic and the need to find averaged quantities and link between the discrete nature of granular system and a continuum description have strongly motivated investigations. In addition, granular media can behave as a solid (e.g. wet sand), a liquid (e.g. flow of grains in a sandglass) or a gas (e.g. collisions of moving beads in a box) [40]. Finally, this medium is highly dissipative, several engineering applications are using granular matter to damp vibrational waves but still using empirical methods. Several numerical models have been developed in order to describe the dynamical behavior of granular packing showing for example the tunability of the bulk properties in bidisperse granular mixtures [41–43].

By defining the grains (shape, size, materials) and the geometry of the granular structure, we can reduced the number of parameters needed to describe the material. Artificial periodic assemblies, also called granular crystals, enable the direct control of the number of interactions between particles leading to a better handling of the dynamical behavior. Therefore, granular crystals are really singular materials because they combine both properties of periodic media with properties of granular media. Fig. 1.2 presents different structures of granular crystals in 1D, 2D, and 3D configurations. The 2D configuration presents possible arrangements of the particles where the diagrams of the interaction between particles are superimposed.

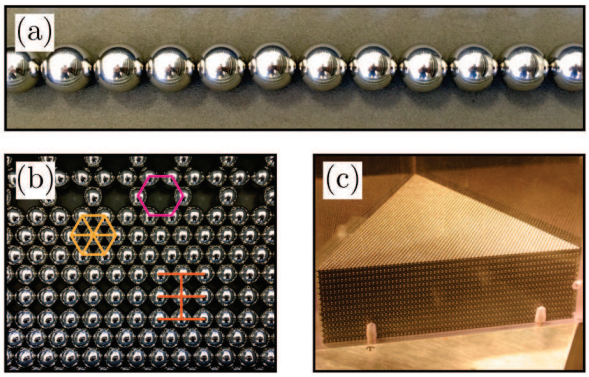

Figure 1.2: Example of a phononic granular structures: (a) 1D, (b) 2D, and (c) 3D [7].

Strong interest for granular media comes from a particular nonlinearity originating from the geometry of the contact between adjacent particles where the contact model have been developed by Hertz [38] (and presented in the section 1.4). The Hertz theory points out a strong nonlinear relation between the force applied to the particles and their displacements. The Taylor development of this normal force/displacement relation includes quadratic and cubic terms (higher order terms are often neglected). These quadratic and cubic nonlinearities are called classical nonlinearities. Thus, phenomena occurring in granular crystals have received considerable interest and are now the subject of very active researches.

The study of granular crystals emerged in 1983 with the work of Nesterenko and Lazaridi on monodisperse granular chains where they predict and experimentally observe highly nonlinear solitary waves [12, 44]. In general, solitons are caused by the counterbalance of the nonlinear effect by the effect of the energy dispersion. The wave profile is constant along the propagation and its velocity depends on the amplitude. A soliton can propagate in an uncompressed chain (zero compressional force between particles) where the linear traditional wave equation does not support a characteristic wave speed of sound [17, 45]. This phenomenon is called *sonic vacuum* [11].

The dynamical response of granular crystals can be tuned from near-linear to weakly nonlinear and highly nonlinear regime by linearizing the system through the application of variable static load [13, 46, 47]. This broad range of dynamical regimes supported by granular crystals has been extensively studied. In the near-linear regime, the possibility of tunable band gaps have been experimentally demonstrated in one-dimensional diatomic chain composed of spheres [48] and cylinders [49]. In the weakly nonlinear regime, phenomena such as harmonic generation, self-demodulation effect, and discrete breathers have been studied [16, 50–53]. Experimental, numerical and analytical methods have been developed to describe the interaction of solitary waves with an interface [54], with a mass defect [17], their dynamics at the interface between two granular crystals [55] and in a disordered diatomic chain [56]. Finally, the study of the highly nonlinear regime has resulted in the proposition of shock absorbers [18], the study of anomalous wave reflection (*acoustic diode* effect) [57], and compact solitary waves [12].

In granular media, besides the classical nonlinearities (quadratic and cubic) discussed above, a non-classical nonlinearity called hysteretic can be also observed when one studies the nonlinear transverse force/displacement relation, or the nonlinear torque/angle relation. This nonlinearity can be taken into account by phenomenological or analytical models [58, 59]. In a recent work, the propagation of hysteretic torsional pulses in a vertical chain composed of magnetic beads has been theoretically and experimentally studied [10]. Another non-classical nonlinearity can originate from the gap opening between particles which can occur when the acoustic strain becomes large enough. When gaps open, the signal is truncated leading to harmonics or even noise [60, 61]. Chaotic behaviors can provide for example bifurcation and period doubling phenomena. Fig. 1.3 depicts example of nonlinear stress/strain relation existing in granular media.

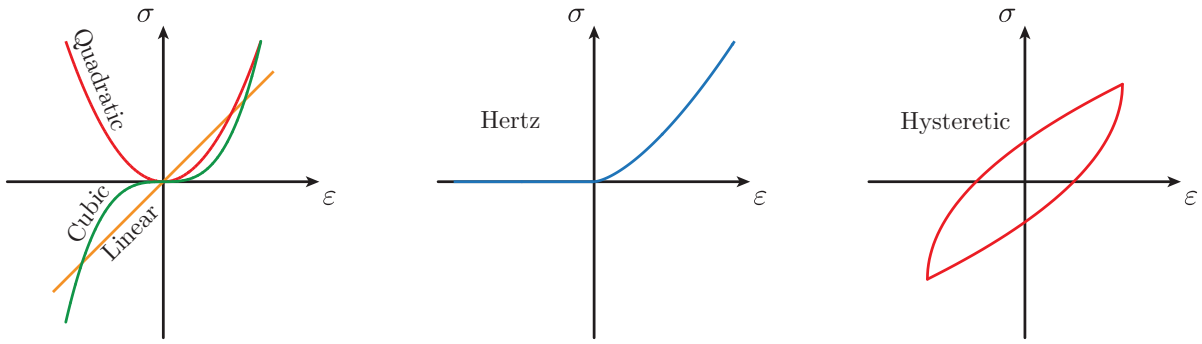

Figure 1.3: Representation of some existing stress/strain relationships in granular media.

In the solid state physics, it is well known that the presence of boundaries or defects breaks the crystal symmetry which can lead to localized vibrational modes. Such modes have been revealed in the linear regime by considering boundary limits to a chain of cylinders [62]. Localized modes have been also experimentally and theoretically studied in diatomic linear chains with glued [15] and welded [63] particles. Other deviations from a one-dimensional translational symmetry include the granular chain with grafted

stubs. These structures support the existence of stub modes. In particular, the presence of these extra-sites leads to dip in the spectral response of the chain [64]. Following these results, side branches considering different materials are periodically grafted to a one dimensional chain [65]. The authors of these works have shown, by numerical and experimental analysis, that the band structure of such systems clearly depends on the material properties of the side branches, thus allowing tunable band structure. In the weakly nonlinear regime, localized modes have been demonstrated considering a mass defect [17, 66]. The combination of nonlinear effects and localized modes enables interesting phenomena employing frequency filtering and asymmetrically excited bifurcations phenomena to provide rectification [22].

The study of two-dimensional and three-dimensional granular phononic structures are less developed due to the difficulty to build a perfect crystal. However, the recent manufacturing progress has stimulated studies in micro/nano-granular structures [9, 68, 69]. Such structures are expected to present a variety of novel dynamic phenomena. The study of square lattice of elastic particles including rotational degrees of freedom have been presented in Ref. [70]. In addition, the theoretical analysis of a granular membrane, composed of a hexagonal lattice, has described the dispersion relations of such system by including bending and shear rigidities at the contact between particles [71]. Some experimental studies in two-dimensional structures have been realized on photoelastic particles [72, 73] and a recent study has shown the effect of disorder on granular contact force chain [67], see Fig. 1.4. The presence of defects can lead to the loss of contact between particles or to local compression in the surrounding particles. Few studies have explored in two-dimensional granular structures the effect of imperfection on stress wave propagation [74–76].

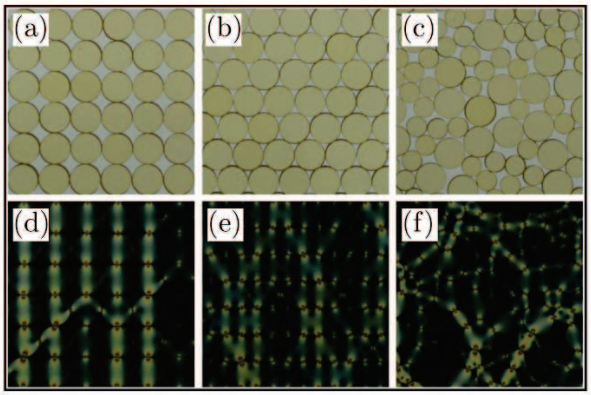

Figure 1.4: (a-c) Two-dimensional structures composed of photoelastic particles submitted to vertical tapping. (d-f) The obtained contact chain forces [67].

An experimental work has also demonstrated the control of wave propagation direction leading for example to acoustic lenses (i.e. concentration of acoustic pulses at a focal point) [21]. The possibility of redirection of nonlinear wave via pulse splitting has been investigated in curved or y-shaped granular networks [77–80]. Moreover, the presence of solitary wave in uncompressed two-dimensional granular crystals have been experimentally and numerically demonstrated [81].

1.3 Importance of rotational degrees of freedom

Rotational degrees freedom are usually neglected as a first approximation but several works have demonstrated that the elastic wave propagation can be modified by taking into account the rotational motion of inclusions [82–84]. The idea to take into account these additional degrees of freedom in the description of the mechanical properties of a material comes from the Cosserat brothers [6]. In 1909, they developed a generalization of the elastic theory, called Cosserat theory or theory of micropolar elasticity, in order to describe the effect of material microstructure on the wave propagation. This model applies not only to the displacements but also to the rotations of structural elements which have to be considered. As described in Ref [85], the application of the Cosserat theory in granular media comes from simple observations. In a classical material, the size of the vibrating particles (nucleus of atoms) is negligible in comparison with the distance between the atoms. The simplest modeling consists in considering the material as a chain of punctual masses linked with springs. The rotational degrees of freedom are not taken into account due to their negligible influence. On the other hand in a granular media, the dimension of the masses are comparable with the distance between the two particles. The forces are applied at the contact and the contact behavior leads to a rigidity perpendicular to the axis formed by the center of the particles in contact. Thus the rotational degrees of freedom must be treated at the same level as the translational degrees of freedom. Neglecting the rotation in granular assemblies leads to artificially stiffen structure which could provide incorrect results. These considerations are the starting point of theoretical studies in granular media following the micropolar theory [86–91]. The presence of rotational degrees of freedom leads to the appearance of rotational modes [70, 88, 92, 93] and affects in particular the velocity and the dispersion of shear waves [71, 94–99].

Despite of the amount of theoretical works including rotational degrees of freedom in granular structures, very few experimental observations of these modes have been realized. The significance of microrotations has been recently revealed experimentally for torsional waves within granular chains [10] as well as for coupled translational-rotational waves in colloidal-based metamaterials [8]. The latter is composed of a two-dimensional monolayer of micron-sized spheres on an elastic substrate as presented in Fig. 1.5(a.1). They predict the resonance frequencies of such system in Ref. [9] considering normal and shear interactions between beads and between bead and substrate (including rotation). The system supports one pure vertical mode of vibration (f_N) and two coupled horizontal-rotational modes (f_{RH}/f_{HR}). By measuring the transmission of surface acoustic waves (SAW) propagating across the interface between the blank sample region and the monolayer they observe an attenuation of the SAWs at the predicted resonance frequencies, presented in Fig. 1.5(a.2). Finally to identify the modes, they tune the interparticle stiffness, which shifts the frequency of the horizontal-rotational resonances while leaving the vertical resonance unaffected and they found reasonable agreement between experiment and theory.

Coupled rotational-translational (TR/RT) elastic waves were first experimentally observed in three-dimensional, hexagonal closely packed granular crystals [7], Fig. 1.5(b.1), the dispersion relation of which

is described by a three-dimensional discrete lattice model that includes the rotational degrees of freedom [100]. The theoretical comparison of the propagation of the waves in a granular crystal with that in a Cosserat medium has demonstrated that the Cosserat theory fails to correctly take into account the inhomogeneities of the material [7]. However, this work has shown that this generalized theory could describe the behavior of granular media at long wavelengths, Fig. 1.5(b.2).

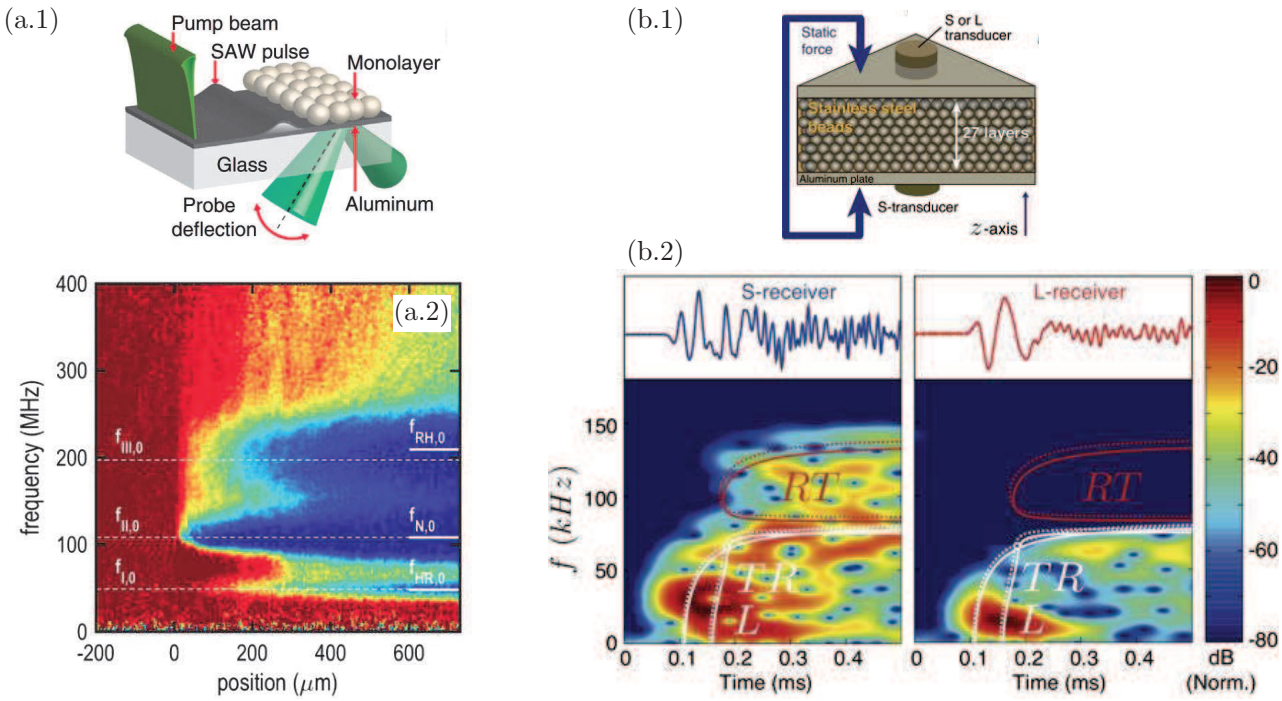

Figure 1.5: (a.1) Schematics of the laser ultrasonic experimental setup of [8]. (a.2) Transmission spectra for surface acoustic waves propagating across the interface between the blank sample region and the monolayer regions [8]. (b.1) Experimental setup for the experimental evidence of coupled rotational-translational (TR/RT) and longitudinal (L) modes [7]. (b.2) Received signals from a shear transducer (left) and a longitudinal transducer (right) after transmission through the crystal [7].

1.4 Mechanical description of the contact between particles

In order to study the acoustic wave propagation in granular media, a mechanical description of the contact between two elastic spheres is essential. Indeed, the macroscopic behavior of granular media is directly controlled by the microscopic behavior at the contact, even for complex media (three-dimensional, heterogeneous, ...).

The elastic deformation of the contact between two elastic beads submitted to a normal stress (directed along the axis formed by the centers of the two beads) has been described by Hertz in 1881 [38]. For this description, he was investigating fringes of light interferences between two glass lenses as a function of the elastic deformation at the contact surface due to axial stress. This relation between the contact deformation and the normal applied stress has been experimentally validated in [46] and numerically investigated in [101]. Mindlin has extended this theory with the application of tangential forces between two elastic spheres [102–105].

The Hertz-Mindlin theory involves assumptions described in the following. The contact area is small compared to the radius of the particle (small deformations) and is planar which allows to decouple the mechanical behavior in the contact zone and the global stress inside the sphere. For the calculation of the local deformations, each sphere is considered as an elastic linear half-space constrained on a small region (elliptical in general) of its planar surface. The theory gives a maximum of normal stress in the center of the contact and a stress equal to zero on its rims. Fig. 1.6 represents a schematics of the contact between two spheres.

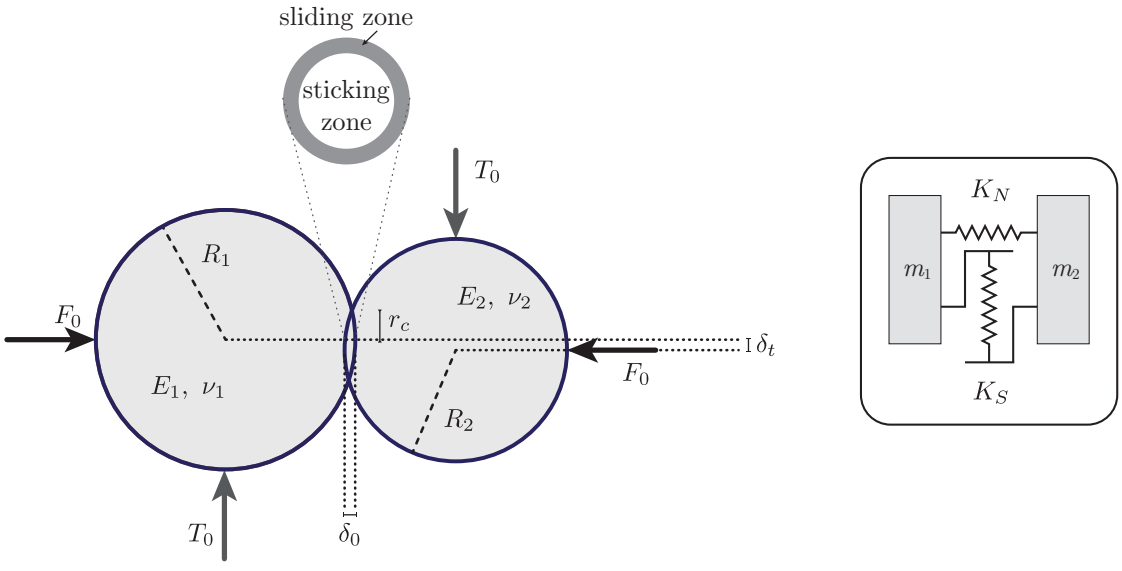

Figure 1.6: Schematics of the contact between two spheres with a representation of the contact surface which depicts the phenomenon of stick/slip. The inset shows the linearized problem allowing a modeling of the system by two masses linked by two springs.

First considering only normal forces, F_0, directed along the centers of the two different beads (different radius and material), the assumptions made lead to define the radius of the contact surface, r_c, between

two spheres as:

$$r_c = \left(\frac{3R^* F_0}{4E^*}\right)^{1/3}, \text{ with } \frac{1}{R^*} = \frac{1}{R_1} + \frac{1}{R_2} \text{ and } \frac{1}{E^*} = \frac{1-\nu_1^2}{E_1} + \frac{1-\nu_2^2}{E_2}, \tag{1.1}$$

where indices 1 and 2 refer to the first and the second particle with R the radius, ν and E the Poisson's ratio and Young's modulus of the particle material, respectively. The relation between the applied normal force F_0 and the relative axial displacement δ_0 of the particles is written as:

$$\delta_0 = \left(\frac{9F_0^2}{16R^* E^{*2}}\right)^{1/3}. \tag{1.2}$$

This force-displacement relation is nonlinear since $\delta_0 \propto F_0^{2/3}$. This nonlinearity comes exclusively from the geometry of the problem and is induced by the increase of the contact surface with the normal force. It can be shown that in the acoustic context, the contact system becomes more nonlinear as F_0 becomes smaller [11].

Because of friction at the contact area, a tangential force T_0 can be applied in addition to the normal force still keeping the particles in contact. As said before, the assumption of planar contact surface allows to decouple the relative normal and tangential displacements. Considering the Coulomb's law, if $T_0 < \mu_f F_0$ where μ_f is the friction coefficient, the beads remain in contact while after this limit the beads slide relative to each other. The tangential stress applied to the surface is zero in the center of the contact but increases away from the center. Thus, the contact area can be separated in a stick zone in the center and an external ring of sliding zone, as presented in Fig. 1.6. The relative tangential displacement δ_t as a function of the tangential force T_0 and the normal force F_0 is given by:

$$\delta_t = \frac{3\mu_f F_0}{4r_c}\frac{1}{G^*}\left[1 - \left(1 - \frac{T_0}{\mu_f F_0}\right)^{2/3}\right], \text{ with } \frac{1}{G^*} = \frac{2-\nu_1}{4G_1} + \frac{2-\nu_2}{4G_2}, \tag{1.3}$$

where $G_1 = E_1/[2(1+\nu_1)]$ and $G_2 = E_2/[2(1+\nu_2)]$ are the shear modulus of each particle. Eq. (1.3) is also nonlinear, here the possibility of sliding could lead to hysteresis effect [103, 105].

Finally in the case of a system in equilibrium considering a static force F_0 and $T_0 \ll \mu_f F_0$, the Hertz-Mindlin relations can be linearized and each contact can be modeled as two rigidities; one for normal interactions and another for transverse interactions. In the particular case where the spheres are identical ($R_1 = R_2$, $E_1 = E_2$ and $\nu_1 = \nu_2$), we obtain for the normal rigidity,

$$K_N = \left(\frac{3R}{4}F_0\right)^{1/3} {E_1}^{2/3}(1-{\nu_1}^2)^{-2/3}, \tag{1.4}$$

and for the transverse rigidity,

$$K_S = (6F_0R)^{1/3}{E_1}^{2/3}\frac{(1-{\nu_1}^2)^{1/3}}{(2-\nu_1)(1+\nu_1)}. \tag{1.5}$$

For this manuscript, we will be interested also in studying the coupling between a sphere and an elastic half-space made of different materials. Thus, considering that the radius of the second particle tends to infinity ($R_2 \to \infty$), and that a static force F is applied at the contact, the rigidity of normal interactions can be explicitly given as,

$$\tilde{K}_N = \frac{3}{2}\left[\frac{4E_1E_2\sqrt{R}}{3E_2(1-{\nu_1}^2)+3E_1(1-{\nu_2}^2)}\right]^{2/3} F^{1/3}, \tag{1.6}$$

and for the transverse interactions,

$$\tilde{K}_S = (6FR)^{1/3}\left[\frac{E_2(1-{\nu_1}^2)+E_1(1-{\nu_2}^2)}{E_1E_2}\right]^{1/3} \times \frac{2E_1E_2}{E_2(2-\nu_1)(1+\nu_1)+E_1(2-\nu_2)(1+\nu_2)}. \tag{1.7}$$

We now turn our attention to the mechanical contact interaction between two elastic spheres submitted to a torsional moment directed around the axes formed by the center of the spheres. From the mechanical point of view, a torsional stress at the contact is close to a tangential stress described by the Hertz-Mindlin theory. When two elastic spheres in contact are submitted to tangential stress, the friction allows to transmit this stress and stick/slip phenomena occurs at the contact. Same phenomena are occurring by considering torsional stress, thus the Hertz-Mindlin theory remains valid in this case [105]. The general expression for the torsional stiffness can be written as:

$$K_T = \frac{16}{3}\frac{(2-\nu_1)(2-\nu_2)}{(2-\nu_1)+(2-\nu_2)}G^* r_c^3. \tag{1.8}$$

If the two particles are identical (same dimension and material) the linear torsional stiffness can be explicitly expressed as:

$$K_T = (2R)\,(1-\nu_1)\,F_0. \tag{1.9}$$

Considering now that the radius of the second particle tends to infinity leading to a contact between a sphere and an half-space, the torsional stiffness becomes:

$$\tilde{K}_T = \frac{4RF_0G^*}{E^*}\frac{(2-\nu_1)(2-\nu_2)}{(2-\nu_1)+(2-\nu_2)}. \tag{1.10}$$

In this section, the linearized rigidities of the contact between particles have been presented for normal, shear, and torsional interactions. We now turn to the description of the dynamical equations of a monoatomic granular chain considering longitudinal displacements.

1.5 One-dimensional granular crystals

This section presents the equations of motion of a one dimensional granular crystal for different dynamical regimes. The notation used in this section is related to the one presented in Ref. [1].

Considering that the applied frequency range remains considerably less than the individual bead resonances and the contact area is very small compared to particle size, the granular crystals can be modeled as a system of masses linked by nonlinear springs, see Fig. 1.7.

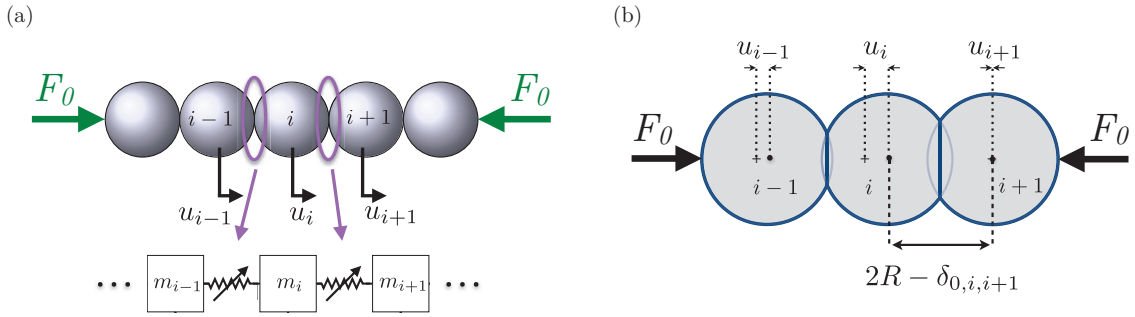

Figure 1.7: (a) Schematics of the one-dimensional granular chain, a mass-nonlinear spring lattice. (b) Schematics of the statically compressed granular chain by a static force F_0. The crosses represent the initial positions of the particle centers in a statically compressed chain while the black circles denote the current positions [11].

This kind of nonlinear lattices has been described by Fermi, Pasta, Ulam and Tsingou (FPU lattices). Such system compressed by a constant static load F_0 is described by the general coupled nonlinear differential equations:

$$m_i\ddot{u}_i = A_{i-1,i}\left[\delta_{0,i-1,i}+u_{i-1}-u_i\right]_+^{3/2} - A_{i,i+1}\left[\delta_{0,i,i+1}+u_i-u_{i+1}\right]_+^{3/2}, \tag{1.11}$$

where u_i is the displacement from the equilibrium position of the ith particle and $\ddot{u}_i$ is its second time-derivative. The mass of a spherical particle is defined by $m_i = \frac{4}{3}\pi R_i^3\rho_i$ with ρ_i the density of the material. The coefficient $A_{i,i+1}$ is defined from the Hertz relation as,

$$A_{i,i+1} = \frac{4E_iE_{i+1}\sqrt{\dfrac{R_iR_{i+1}}{R_i+R_{i+1}}}}{3E_{i+1}(1-\nu_i^2)+3E_i(1-\nu_{i+1}^2)}, \tag{1.12}$$

and the static overlap $\delta_{0,i,i+1}$ can be rewritten as,

$$\delta_{0,i,i+1} = \left(\frac{F_0}{A_{i,i+1}}\right)^{2/3}. \tag{1.13}$$

It should be noticed that Eq. (1.12) is equivalent to the Eq. (1.2). In the Eq. (1.11), the sign $[s]_+$ means that there is no force between the particles when they are separated; for $s \leqslant 0$, the bracket $[s]$ takes the value 0 and if $s > 0$, the bracket takes the value s. We note that the dissipation is neglected in the presented model.

For the particular case of monoatomic granular crystals, i.e considering the same elastic particles in dimension and material in the chain, it follows that $R_i = R$, $m_i = m$, $m = \frac{4}{3}\pi R^3 \rho$, the coefficient $A_{i,i+1}$ can be simplified to,

$$A_{i,i+1} = A = \frac{E\sqrt{2R}}{3(1-\nu^2)}, \tag{1.14}$$

and the static overlap $\delta_{0,i,i+1}$ becomes,

$$\delta_{0,i,i+1} = \delta_0 = \left(\frac{F_0}{A}\right)^{2/3}. \tag{1.15}$$

Finally, the equations of motion Eq. (1.11) can be reduced to:

$$m\ddot{u}_i = A\left[\delta_0 + u_{i-1} - u_i\right]_+^{3/2} - A\left[\delta_0 + u_i - u_{i+1}\right]_+^{3/2}. \tag{1.16}$$

1.5.1 Near linear regime

These nonlinear equations Eq. (1.16) can be linearized assuming the approximation of very small amplitude of displacement in comparison with the static overlap: $|u_{i-1} - u_i| \ll |\delta_0|$. An expansion in power series can be realized keeping only the first order. In this case, the force/displacement relation can be considered as linear and the granular chain can be approximated as a linear lattice.

The linearized differential equations for a monoatomic granular crystal take the following form,

$$m\ddot{u}_i = K_2\left(u_{i-1} - u_i\right) - K_2\left(u_i - u_{i+1}\right), \tag{1.17}$$

where $K_2 = \dfrac{3}{2}A\delta_0^{1/2}$ is the spring constant and is explicitly given by,

$$K_2 = \frac{E\sqrt{2R}}{3(1-\nu^2)} \cdot \sqrt{\delta_0} = \left(\frac{3R}{4}F_0\right)^{1/3} E^{2/3}(1-\nu^2)^{-2/3}. \tag{1.18}$$

It is worth mentioning that Eq. (1.18) is equivalent to Eq. (1.4), i.e. $K_2 \equiv K_N$.

1.5.2 Weakly nonlinear regime

Considering now that the amplitude of the relative displacement is small comparatively to the static load i.e $|u_{i-1} - u_i| < \delta_0$, the expansion in power series is developed up to the fourth order term. The regime can be considered as weakly nonlinear. Finally, the equations of motion can be written in the following form:

$$m\ddot{u}_i = \sum_{k=2}^{4} K_k\left[(u_{i+1} - u_i)^{k-1} - (u_i - u_{i-1})^{k-1}\right], \tag{1.19}$$

where $K_2 = \frac{3}{2}A\delta_0^{1/2}$, $K_3 = -\frac{3}{8}A\delta_0^{-1/2}$, $K_4 = \frac{3}{48}A\delta_0^{-3/2}$.

Eq. (1.19) is an example of the FPU model. This type of nonlinear lattice has been used in many theoretical studies revealing nonlinear periodic waves, solitary waves [106], and discrete breathers [16, 107, 108].

1.6 Longitudinal normal modes in a one dimensional monoatomic granular crystal

Let us consider the linear dynamics of a monoatomic granular chain for longitudinal displacement. As it has been presented thanks to the linearization of the Hertz theory, the granular chain can be modeled as a linear mass-spring lattice represented in Fig. 1.8.

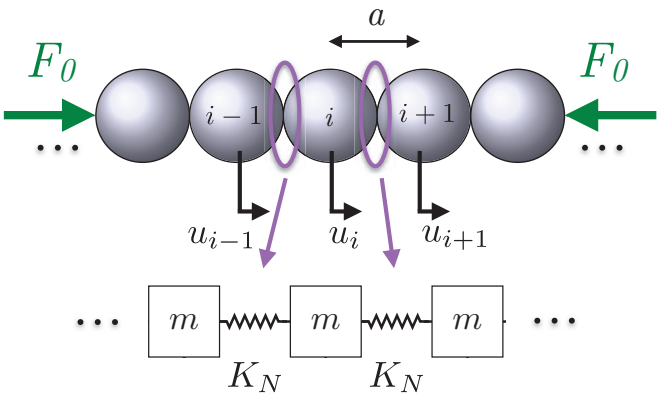

Figure 1.8: Schematics of a one-dimensional granular chain and its representation by a linear mass-spring lattice.

The equations of motion of the i-th particle have been already presented in the previous section and can be rewritten as:

$$m\ddot{u}_i = K_N \left(u_{i-1} - 2u_i + u_{i+1}\right). \tag{1.20}$$

Looking for solutions of equations Eq. (1.20) in the form:

$$u_n = B\, e^{i(\omega t - kna)}, \tag{1.21}$$

where ω is the wave pulsation, k the wave number, and $a = 2R$ the lattice constant, the following dispersion relation is obtained:

$$\omega^2 = \frac{4K_N}{m} \sin^2\left(\frac{ka}{2}\right). \tag{1.22}$$

This relation is represented in Fig. 1.9. This relation is periodic and thus we can limit the representation between values of k from 0 to π/a. This wave number interval is called first Brillouin's zone [109]. From Eq. (1.22), the cut-off pulsation ω_c is defined by the relation

$$\omega_c = 2\sqrt{\frac{K_N}{m}}, \tag{1.23}$$

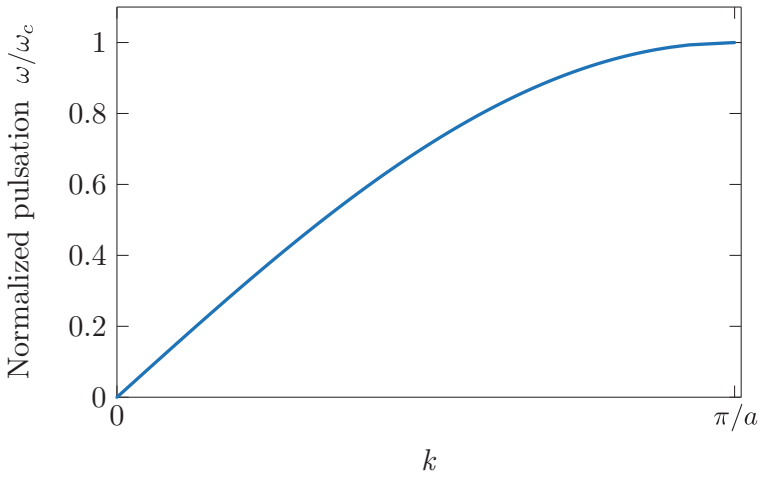

Figure 1.9: Dispersion relation for the longitudinal mode in one-dimensional granular chain.

Under this cut-off pulsation $\omega < \omega_c$, the wave number is real and written as

$$k = \pm\frac{2}{a}\arcsin\left(\frac{\omega}{\omega_c}\right). \tag{1.24}$$

The sign *plus* corresponds to the wave propagating toward the increasing i. Oppositely, the sign *minus* corresponds to the wave propagating toward the decreasing i. When $\omega > \omega_c$, the wave number becomes complex which implies that harmonic waves are evanescent. The zone above this cut-off pulsation is a forbidden band of propagation also called band gap. The wave number in the forbidden band is decomposed in a real and imaginary part:

$$k = \frac{\pi}{a} - j\frac{2}{a}\text{arccosh}\left(\frac{\omega}{\omega_c}\right), \tag{1.25}$$

where $j = \sqrt{-1}$.

The dispersion relation (1.22) allows to define the phase velocity c_{L_ϕ} which is written as,

$$c_{L_\phi} = \frac{\omega}{k} = \frac{a\omega}{2\arcsin(\omega/\omega_c)}, \text{ when } \omega < \omega_c, \tag{1.26}$$

and the group velocity $c_{L_{gr}} = \dfrac{\partial\omega}{\partial k}$,

$$c_{L_{gr}} = \frac{\partial\omega}{\partial k} = a\sqrt{\frac{K_N}{m}\left(1 - \frac{\omega^2}{\omega_c^2}\right)}. \tag{1.27}$$

In general, the phase velocity describes the velocity at which the phase of the wave with (ω, k) propagates. The group velocity is the velocity at which the amplitude envelope of a wave packet propagates. The wave packet is the superposition of propagating waves with different values of k. Generally, the group velocity corresponds to the velocity at which the energy is transmitted by the signal. Fig. 1.10 shows the phase

and group in a monoatomic granular chain considering longitudinal modes. The velocities are normalized by the maximum of the phase velocity $c_{L_{\phi c}} = a\omega_c/2$.

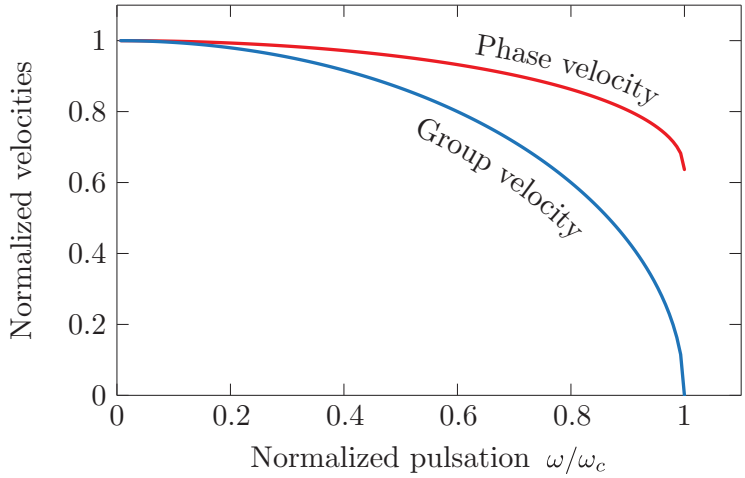

Figure 1.10: Phase and group velocities for the longitudinal mode in a one-dimensional granular chain.

For the low frequency range, phase and group velocity are equal meaning that the wave is propagating without dispersion. As long as the frequency increases, phase and group velocity are decreasing and the difference between the velocities is increasing. The group velocities is decreasing more rapidly than the phase velocity and at the Brillouin's limit $k = \pi/a$ the group velocity is equal to zero.

The next section focuses on the utility and ability of an external magnetic field to design a magneto-granular structure.

1.7 Magnetic description of the magneto-granular phononic crystal

The use of magnetic elements to control wave propagation in discrete systems has received a growing interest the last decades. Nonlinear magnetic potential between particles has been explored via repelling magnetic oscillators showing existence of solitary waves [110], chaotic behavior [111], moving breathers [112], and second harmonic generation [113]. Magnetic field has been also used as an external stimulus in order to introduce contactless tunability of band gap structure [5, 114, 115]. Finally, magnetism could provide attractive forces, thus chains of magnetic beads can be formed without the need of an external load [10, 116].

The designed structure studied here, Fig. 1.11, is composed of a chain of spherical steel beads inside a properly designed magnetic field. This field is induced by an array of permanent neodymium magnets (NdFeB) located at a given distance from the granular chain or in direct contact with the chain. Since ferromagnetic materials (as steel) can be strongly magnetized in the presence of a magnetic field, changing the magnetic field strength allows tuning the interparticle forces and consequently the dynamic response of the granular crystal. This setup offers the advantages of straightforward construction and non-contact tunability via external magnetic fields.

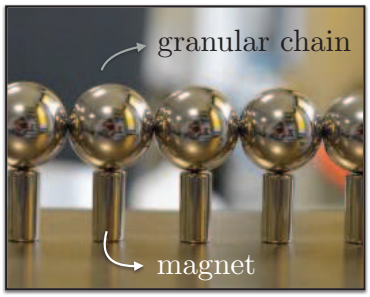

Figure 1.11: Picture of the experimental setup of the granular chain in direct contact with the magnets.

The aim of this section is to describe the role of the permanent magnets for the creation of attractive forces between particles by analytical, numerical and experimental means. The interaction force between soft magnetic particles, in the presence of uniform and non-uniform applied magnetic fields, was investigated in Ref. [117]. Fujita and Mamiya in Ref. [118] have presented an analytical model for the interaction forces between two non-magnetic spheres in the presence of a uniform magnetic field. In our case, due to the highly non-unifom form of the magnetic field and the interactive magnetization between spheres, analytical formulas of the magnetic forces between spheres are not available. Thus, we will turn to numerical simulations using the ACDC module from Comsol multiphysics (solving through the finite element method (FEM)). Simple configurations will be studied analytically and experimentally in order to verify the numerical simulations. In particular, numerical simulations can be used to calculate the magnetic flux density of our complete configuration, while experimental measurements estimate the attractive forces between two adjacent spheres.

1.7.1 Magnetic field created by one magnet

The non-uniform magnetic field created by a permanent magnet has been analytically presented by Yonnet in Ref. [119] in two and three dimensions. In this section we consider the 2D configuration. The rectangular magnet has a height $2L_m = 10$ mm, width $2l_m = 4$ mm and an infinite dimension along z-axis. The

analytical expressions of the magnetic field components in air $B_0(x, y)$ for such a magnet are:

$$B_{0x} = \frac{-\sigma^*}{4\pi\mu_0} \sum_{i=0,1} \sum_{j=0,1} (-1)^{i+j} \ln\left\{[l_m + (-1)^i x]^2 + [L_m + (-1)^j (y + L_m)]^2\right\}, \tag{1.28a}$$

$$B_{0y} = \frac{-\sigma^*}{4\pi\mu_0} \sum_{i=0,1} \sum_{j=0,1} (-1)^{i+j} 2\text{atan}\left(\frac{l_m + (-1)^i x}{L_m + (-1)^j (y + L_m)}\right), \tag{1.28b}$$

where $\sigma^* = B_r \mu_0 \mu_{air}$ is the surface charge density of the magnet with the remanent magnetization B_r, $\mu_0 = 4\pi 10^{-7}$ is the vacuum permeability and $\mu_{air} = 1$ is the relative permeability of the air. Inside the magnet, the field is calculated using the same expressions of Eqs. (1.28) considering now $\sigma^* = B_r \mu_0 \mu_m$ where μ_m is the relative permeability of a permanent neodymium magnet. For our configuration, we use a permanent neodymium magnet with $\mu_m = 1.05$. Then, the density of the magnetic field is given by $B_0 = \sqrt{B_{0x}^2 + B_{0y}^2}$. The left panel of Fig. 1.12 shows analytical results from Eqs. (1.28) for the magnetic field density B_0.

We turn now to finite element simulations. The magnetic flux lines created by a permanent magnet are circular and thus we chose a surrounding box of air with circular shape in order to minimize the boundary problem which can appear with a square box. Finally, the studied domain consists of a disk with air characteristics ($\mu_{air} = 1$), and a rectangle corresponding to the permanent magnet with $\mu_m = 1.05$ and $B_r = 1.32$ T. The direction of the polarization has to be defined. In our case the polarization is along y-axis. Moreover, a surrounding domain with *infinite elements* is created leading to an unbounded domain, mimicking a free space case, see Fig. A.2. The mesh is built with triangles, for the study domain, and with quadrangle, in the *infinite domain*. The total density of magnetic field is presented on the center panel of the Fig. 1.12. In order to compare analytical and numerical results, we define a relative error as

$$Error = 100 \frac{|B_a - B_n|}{B_n}, \tag{1.29}$$

where the indexes a and n correspond to analytical and numerical results respectively. The error on the total density of magnetic filed is shown on the right panel of the Fig. 1.12.

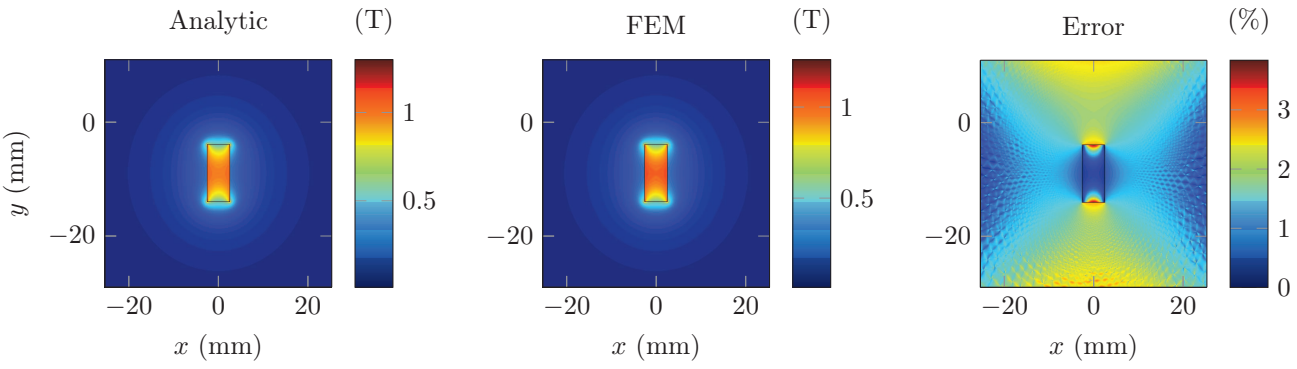

Figure 1.12: Density of the magnetic field created by a rectangular magnet. Left panel analytical, central panel numerical results. Right panel, the error between analytical expression and finite element simulations.

We can notice that the global error on the magnetic field density B_0 is less than 4% and as a conclusion, the 2D simulated magnetic field for a permanent magnet is well numerically simulated. So we can extend the numerical simulation to three dimensions. The way to simulate in 3D is the same than in 2D but now we consider a surrounding sphere of air and the magnet becomes a cylinder (with finite dimension in the z-direction, see Fig 1.13). The spacial decrease of the magnetic field from the upper surface of the magnet is studied. Analytically, a simple expression for this decrease of magnetic field in 3D configuration along the symmetry axis of a cylinder axially magnetized (y-axis in our case) is given by:

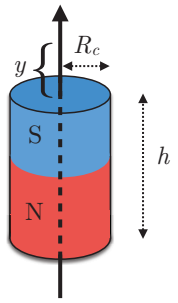

Figure 1.13: Representation of the magnet.

$$B = \frac{B_r}{2}\left(\frac{h+y}{\sqrt{R_c^2+(h+y)^2}} - \frac{y}{\sqrt{R_c^2+y^2}}\right), \tag{1.30}$$

where B_r is the remanent magnetization which is independent from the geometry, y is the distance from the pole surface on the axis of symmetry, h is the height of the cylinder and R_c is the radius of the cylinder. Measurement using a Gauss-meter *F.W. Bell 5180* allows to estimate experimentally the magnetic field from our neodymium magnets. Analytical, numerical and experimental results are presented in Fig. 1.14 for two different magnets with the permanent magnetization $B_1 = 1.32$ T and $B_2 = 1.37$ T given by the manufacturer.

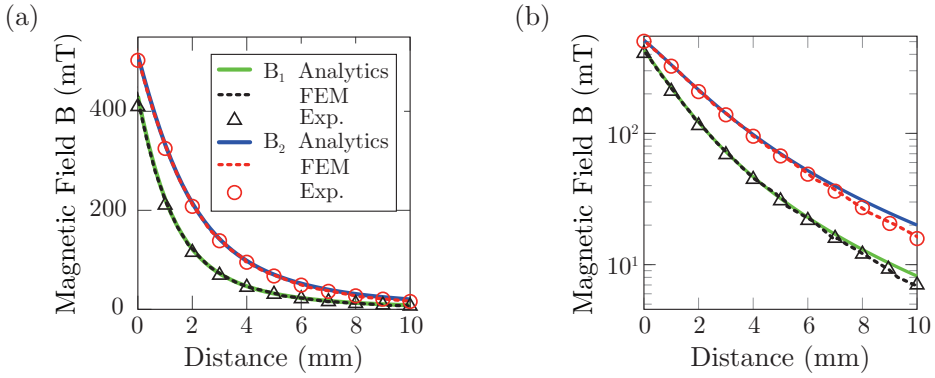

Figure 1.14: Magnetic flux density as a function of the distance from the upper surface of magnets for $B_1 = 1.32$ T and $B_2 = 1.37$ T from Eq. (1.30) (solid line), from 3D finite element simulations (dashed line) and experiments (marks) (a) in linear scale and (b) in log scale.

A very good agreement is found between analytical, FEM simulations and experimental results. Only far from the upper magnet surface it seems that analytical results deviate from from numerical and experimental results that are still in very good agreement. It can be observed that major variations in magnetic field strength are possible by either placing the permanent magnets at different distances or changing their remanent magnetization. For example, by using the B_1 permanent magnets, the magnetic field at $D = 10$ mm from the upper surface of the magnet is reduced by 42% compared to B_2 permanent magnets (see Fig. 1.14(b)). As we will see in the next section, this effect influences the strength of the static normal forces between spheres F_0 (see Fig. 2.12), induced by the external magnetic field. It should

be noticed that analytical results with 2D configuration from Eqs (1.28) completely over-estimated the magnetic field. That clearly demonstrated the need to go from 2D to 3D simulations in order to have quantitative results consistent with experiments.

In the next section, we study the forces between between magnets and beads as well as between beads.

1.7.2 Magnetic field induced by several magnets and beads

The objective of this section is to obtain the interaction forces between beads, and between magnets and beads. First we check what happens when magnets are put in a linear array and in a configuration where poles of the magnets are alternatively oriented. Numerical and experimental results are performed with a chain of 15 magnets. Experimentally, a Gauss-meter *F.W. Bell 5180* is used to measure the magnetic field. It is attached to a 3D moving robot *PI*. This robot is programmable and allows to scan by planes choosing the spatial step between two measured points. The schematics of the experimental setup is presented on Fig. 1.15. We scan the plane (x,z) just above the top of magnets considering a spatial step of 0.5 mm and numerical simulations using COMSOL are performed for this configuration. Results are shown in Fig. 1.16. Experimental measurements on the plane (x,y) are presented in the appendix A.

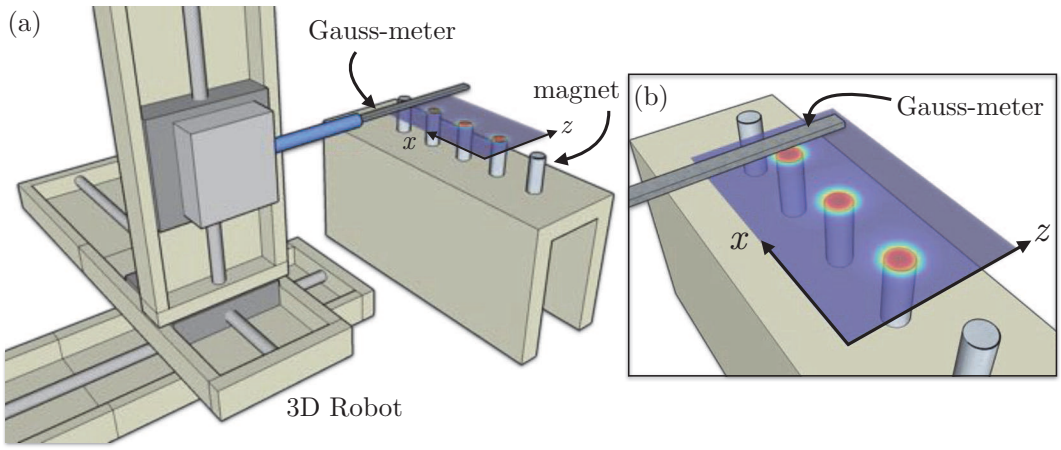

Figure 1.15: (a) Experimental setup to measure the magnetic field created by a linear array of magnets. (b) Zoom on the Gauss-meter. The experimental magnetic field measured by the Gauss-meter is superimposed on both panels.

From Fig. 1.16(a-b), we can see red spots corresponding to high intensity of the magnetic field when the probe is just above the top of magnets. We can observe some differences in the size of spots. These differences are confirmed on panel (c), where we see that along the line $z = 1$ cm the experimental data falls close to zero. This effect comes from the sensitivity range of the probe which is very low leading to less accuracy when the magnetic field becomes small. We can also notice from panel (c), looking at the maxima of the magnetic field, that the field decreases along the chain of magnets. This could be happening because experimentally, magnets are not perfectly aligned with the plot line $z = 1$ cm and not exactly at the same distance from the probe (in the y-direction). Numerically, in order to simulate this misalignment we deviate very slightly the plot line in order to obtain identical plot line between both

results. Thus good agreement is found for the large value of the magnetic field.

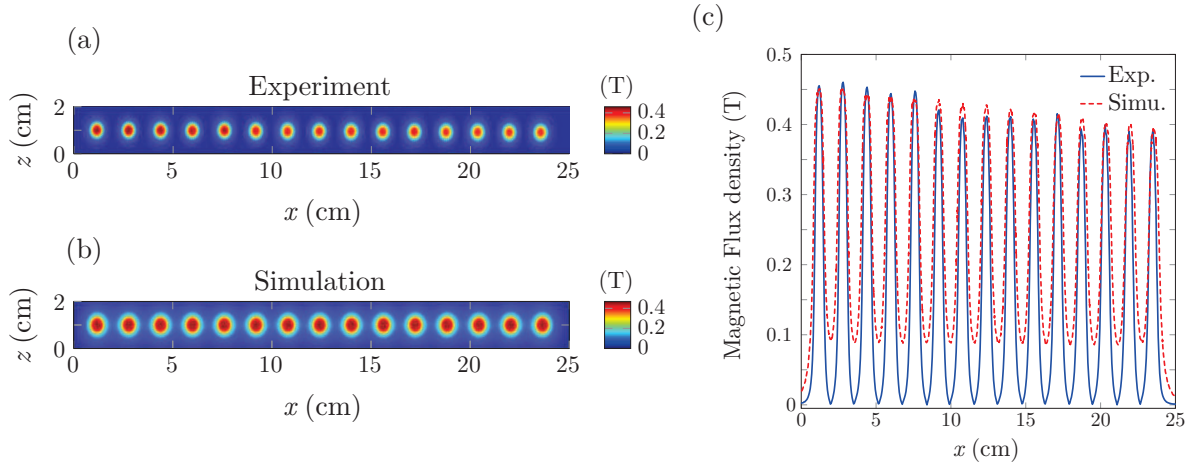

Figure 1.16: Magnetic field created by a chain of 15 magnets from (a) experiments and (b) simulations. (c) Magnetic field on the line $z = 1$ cm from experiments (solid line) and simulations (dashed line).

Then, we add a stainless steel bead above each permanent magnet in order to determine attractive forces into the chain of beads. Just to understand qualitatively the magnetization of the bead by the presence of a permanent magnet, Fig 1.17 depicts simple cases where we can see how the magnetic field (calculated by FEM simulations) creates attractive forces between the beads of the chain.

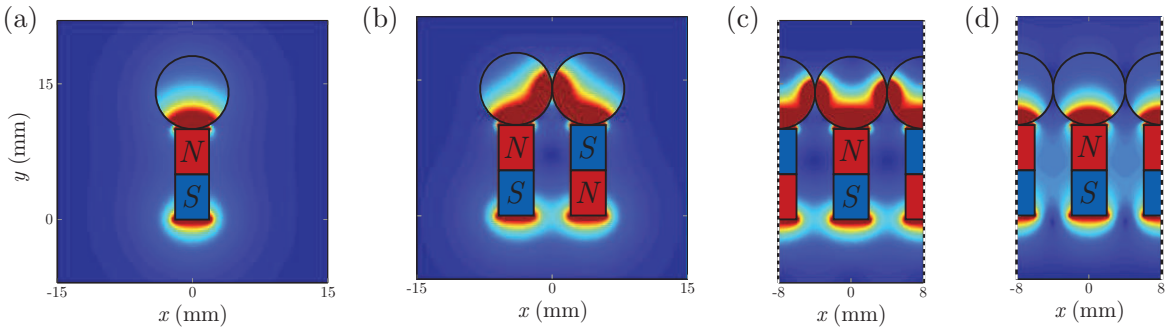

Figure 1.17: Simulated magnetic field created by (a) one magnet, (b) two magnets with poles alternatively oriented. (c) Simulated magnetic field using periodic conditions for alternatively and (d) identically orientations of the poles.The colormap is saturated to see clearly the magnetization into the beads. Red to blue color means high to low density of magnetic field respectively.

Fig. 1.17(a) shows that the bead is magnetized due to the presence of the permanent magnet which is in contact with it. Analytical and numerical simulations in 2D configuration for the case of one bead / one magnet are presented in the appendix A. Panel (b) shows the magnetic field created by 2 permanent magnets with alternatively oriented poles. As we can see beads are densely magnetized around the contact between them. If we look at real values of the magnetic field, beads are polarized with opposite sign leading to attractive forces between particles. The case of an infinite chain of beads and magnets alternatively oriented is shown in Fig. 1.17(c). The high density of magnetic field at the contact point between particles leads to attractive forces into the chain. If the magnets are oriented in the same direction (Fig. 1.17(d)),

there is no more high density of magnetic field and thus beads are not attracted by each other. It should be noted that in all the cases, dense magnetic field is present at the bead/magnet contact leading as well to attractive forces of these two particles. For these reasons, experimentally the magnet will be placed with alternate orientation in order to obtain attractive forces between particles into the chain.

Thanks to these numerical simulations, we can try to determine the attractive forces between beads and magnets. We consider two beads in direct contact with magnets (alternatively oriented) surrounded by a sphere of air. The distance between the two beads is varying from 1mm to zero (beads in contact), see Fig. 1.18. Parametric analysis is performed on the mesh to ensure the convergence of the results. Using magnets with $B_1 = 1.32$ T remanent magnetization and beads with diameter 15.875 mm and with a 1 mm distance between each other, we obtained a variation of the force: 6 N $< F <$ 6.4 N. Decreasing the element size of the bead mesh, leading to an increase of the element numbers, we obtained a variation on the force equal to 0.02 N. The calculation of the force F between beads and magnets converges to a constant value. When the beads are in contact, the force between magnets and beads is found to be $F \approx 6.4$ N. So, small variation of the distance between the spheres do not dramatically change the magnetic density at the contact between beads and magnets and thus the resulting attractive force takes similar values. We also tested other cases. For example, by using magnets with $B_1 = 1.32$ T remanent magnetization but smaller beads of 8 mm diameter, we calculated from FEM simulations an attractive force of $F \approx 5$ N. For both cases, we also measured experimentally the resulted forces. We found for the magnet B_1 the force to be $F = 4.5$ N for a 8 mm bead and $F = 5.5$ N for a 15.875 mm bead. Thus, numerical and experimental results are in good agreement. Another case that we studied was the one of magnets with stronger remanent magnetization, namely $B_2 = 1.37$ T. FEM simulations give an attractive force of $F \approx 10.5$ N for beads of 15.875 mm in diameter. Experimentally, we found $F > 7$ N, since the dynamometer limit is 7 N so we cannot confirm this estimated value by direct measurements. However in section 2.3.3, the comparison between theoretical prediction using $F = 10$ N and experimental results will indirectly confirm this estimated value. If more unit cells are simulated, the estimated values are still the same.

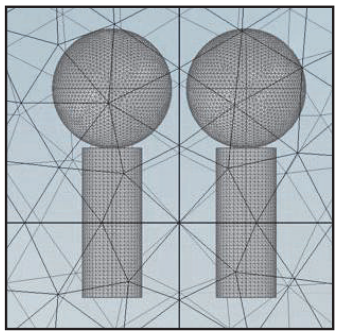

Figure 1.18: Simulated mesh in FEM, non contact case.

Let us examine now the force between spheres F_0. Considering identical protocol, we start the simulation by two unit cells varying the distance between them from 1 mm to 0, i.e. contact between spheres. When the beads are not in contact we observe an increase of the attractive force from 0.28 N to 7.15 N approaching the two cells. When the beads are in contact the force becomes 3.1 N. Making a parametric analysis on the mesh, creating an adaptive mesh as a function of the distance of separation, the results do not converge. We can find values from $F_0 = 0.2$ to 20 N and if the particles are very densely mesh at the contact, the precompression force can reach values up to 330 N. Since this work is not focused on the simulation problem and because this force can be experimentally measured, we decide to use the numerical simulation only to estimate the force between beads and magnets.

1.8 Conclusion

Granular phononic crystals are interesting engineered structures that combine both properties of periodic media with properties of granular media. They exhibit tunable dynamic behavior that leads to particular phenomena on the acoustic wave propagation such as tunable band gaps, energy localization, or wave guiding. The acoustic wave propagation in granular media depends on periodicity (e.g. monoatomic or diatomic chain), on the dimensionality (1D, 2D or 3D structures), and the interaction between particles (including rotational degrees of freedom, nonlinearity) for example. Consequently, the diversity of phenomena occurring in granular media have strongly motivated this present work.

The possible realization of an experimental granular device using an external magnetic field has been proposed in the latest section. In order to describe the dynamical behavior of such structure, the following chapter is devoted to the theoretical description of the linear dynamics of a monoatomic granular chain including all the degrees of freedom in translational and rotational bead motions. In addition, the effect of the coupling between the granular chain and a substrate is theoretically and experimentally studied.

Chapter 2

Tunable magneto-granular phononic crystals

Contents

2.1 Introduction 32
2.2 Theory of infinite linear granular chain considering 6 degrees of freedom . . 33
2.2.1 Equations of motion for sagittally polarized modes 34
2.2.2 Equations of motion for horizontally polarized modes 35
2.2.3 "Free" linear granular chain 38
2.2.4 Linear granular chain coupled with a rigid substrate 40
2.2.5 Summary 43
2.3 Linear spectra : experimental results and discussion 44
2.3.1 "Free" linear granular chain 45
2.3.2 Tunable "Free" linear granular chain by external magnetic fields 47
2.3.3 Linear granular chain coupled with a rigid substrate 48
2.3.4 Summary 51
2.4 Experimental and numerical dispersion curves 53
2.4.1 Characterization of the experimental driver 53
2.4.2 Modeling of the finite linear granular chain 55
2.4.3 Experimental dispersion curve method and setup configuration 56
2.4.4 Results and discussion 58
2.4.5 Summary 64
2.5 Conclusion 66

2.1 Introduction

This chapter is devoted to the study of the linear dynamics of one-dimensional magneto-granular phononic crystals composed of a chain of spherical steel beads inside a properly designed magnetic field. First, the theoretical description of the three-dimensional dynamics of the chain is presented. A linear model taking into account all degrees of freedom of the beads (three translations and three rotations) as well as all elastic couplings (longitudinal, shear and torsional), between the beads and between the beads and the substrate is developed. This model provides the dispersion relation of the modes in the system for different coupling parameters.

The associated experiments confirm the elastic propagation of modes with micro-rotation of beads and demonstrate the pertinence of the model for the system description. Several interesting effects on the dispersion are observed and discussed, like zero group velocity modes. Moreover, tunability of the dynamical response of the granular chain is demonstrated by changing the strength of the external magnetic field. Finally, experimental dispersion curves are performed by measuring each particle velocity of the chain and are successfully compared to numerical simulations including boundary conditions and the experimental driver characteristics.

2.2 Theory of infinite linear granular chain considering 6 degrees of freedom

To describe the three-dimensional dynamics of a linear granular chain and its mechanical coupling to a rigid substrate, we consider the model as shown in Fig. 2.1. The possible motions are presented in two decoupled planes, a "sagittal" plane (x,y) and a "horizontal" plane (x,z). The model considers all 6 degrees of freedom for each n-th sphere of the chain; 3 displacements along $j = x, y, z$-direction ($u_{n,j}$) and 3 rotations ($\phi_{n,j}$). The linear model assumes infinitely small displacements and angular displacements. Between two adjacent spheres, we consider normal, shear and torsional couplings characterized by constant rigidities K_N, K_S and K_T respectively. The coupling of the linear granular chain with the substrate is characterized by the normal, shear and torsional constant rigidities $\tilde{K}_N$, $\tilde{K}_S$, $\tilde{K}_T$, respectively. Note that in this study we ignore a possible bending coupling between the particles verified to be very weak [99].

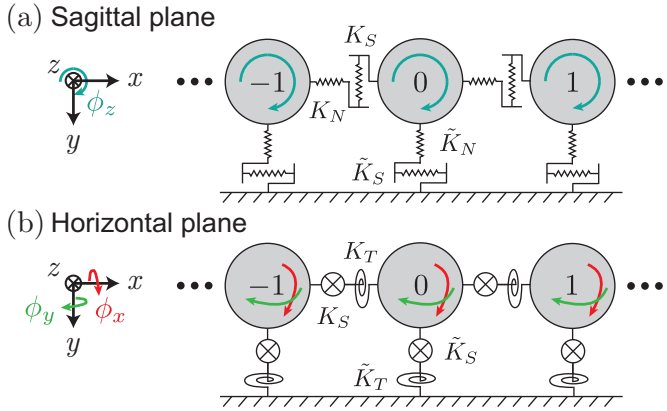

Figure 2.1: Representation of the infinite granular chain coupled with a rigid substrate. Displacement and rotation motions are separated in (a) the sagittal plane (displacements along x and y, rotation relative to z-axis) and (b) the horizontal plane (rotations relative to x and y-axes, displacement along z).

In order to obtain the equations of motion of our system, the Lagrangian formalism is used [91]. For a system of N degrees of freedom described by N generalized coordinates α, the lagrangian $\mathcal{L}$ is expressed from the generalized coordinates α_i and their time-derivative $\dot{\alpha}_i$ as the difference between the kinetic energy T and the potential energy V.

$$\mathcal{L} = T - V \tag{2.1}$$

Equations of motion in Lagrangian mechanics are Lagrange's equations of the second kind (also called Euler-Lagrange equations) and are written as follows:

$$\frac{\partial \mathcal{L}}{\partial \alpha_i} - \frac{d}{dt}\left(\frac{\partial \mathcal{L}}{\partial \dot{\alpha}_i}\right) = 0, \tag{2.2}$$

where $i = 1, 2, ...N$ corresponds to the i-th degrees of freedom.

For our system, we can obtain the equations of motion using the Lagrangian formalism for modes polarized in the sagittal and horizontal plane.

2.2.1 Equations of motion for sagittally polarized modes

In the sagittal plane, there are 3 degrees of freedom (2 displacements u_x, u_y and 1 rotation ϕ_z). The system is presented in Fig. 2.2, where we show the zero-th particle which is in contact with the neighboring particles -1, 1 and the substrate, denoted by particle 2. For each contact, we consider normal and shear couplings.

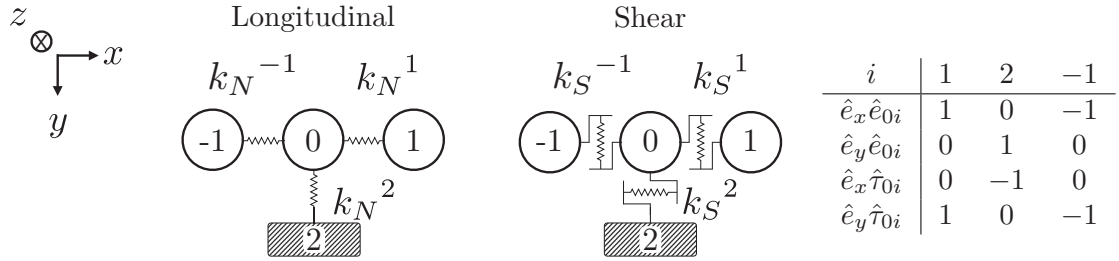

i	1	2	-1
$\hat{e}_x\hat{e}_{0i}$	1	0	-1
$\hat{e}_y\hat{e}_{0i}$	0	1	0
$\hat{e}_x\hat{\tau}_{0i}$	0	-1	0
$\hat{e}_y\hat{\tau}_{0i}$	1	0	-1

Figure 2.2: Representation of the studied system for the sagittal plane.

The Lagrangian of the particle "0" is described as follows:

$$\mathcal{L}_{\mathbf{s}}^{(0)} = T_{\mathbf{s}}^{(0)} - V_{\mathbf{s}}^{(0)}, \tag{2.3}$$

where the indices "S" refers to the sagittal plane. The kinetic energy $T_{\mathbf{s}}$ and the potential energies $V_{\mathbf{s}}$ are given by:

$$T_{\mathbf{s}}^{(0)} = \frac{1}{2}m_0\left(\dot{u}_{0,x}^2 + \dot{u}_{0,y}^2\right) + \frac{1}{2}I_0\dot{\phi}_{0,z}^2, \tag{2.4a}$$

$$V_{\mathbf{s}}^{(0)} = \frac{1}{2}\sum_{i=-1,2,1}\left({k_N}^i{\Delta L_i}^2 + {k_S}^i{\Delta S_i}^2\right), \tag{2.4b}$$

where $i = \{-1, 2, 1\}$, m_0 is the mass and I_0 is the particle's momentum of inertia (for the particular case of homogeneous spheres $I = \frac{2}{5}mR^2$). The normal and shear rigidities are ${k_N}^i = \{K_N, \tilde{K}_N, K_N\}$ and ${k_S}^i = \{K_S, \tilde{K}_S, K_S\}$ for the interaction between the zero-th particle and the i-th particle, respectively. Normal ΔL_i and shear ΔS_i spring elongations can be explicitly written as:

$$\Delta L_i = (u_{i,x} - u_{0,x})\,\hat{e}_x\hat{e}_{0i} + (u_{i,y} - u_{0,y})\,\hat{e}_y\hat{e}_{0i}, \tag{2.5}$$

$$\Delta S_i = (u_{i,x} - u_{0,x})\,\hat{e}_x\hat{\tau}_{0i} + (u_{i,y} - u_{0,y})\,\hat{e}_y\hat{\tau}_{0i} - (R_i\phi_{i,z} + R_0\phi_{0,z}), \tag{2.6}$$

where we denote by $\hat{e}_{0i}$ the unit vector in the direction from the zero-th particle center to the i-th particle center. $\hat{e}_x$, $\hat{e}_y$ and $\hat{e}_z$ correspond to the unit vector along x, y and z-axis, respectively. $\hat{\tau}_{0i}$ is the unit vector normal to $\hat{e}_{0i}$ and $\hat{e}_z$: $\hat{\tau}_{0i} = [\hat{e}_z \cdot \hat{e}_{0i}]$. Then, the Lagrange's equations are:

$$\frac{\partial\mathcal{L}_{\mathbf{s}}^{(0)}}{\partial\alpha_{\mathbf{s}}} - \frac{d}{dt}\left(\frac{\partial\mathcal{L}_{\mathbf{s}}^{(0)}}{\partial\dot{\alpha}_{\mathbf{s}}}\right) = 0, \tag{2.7}$$

where $\alpha_{\mathbf{s}} = (u_x, u_y, \phi_z)$ denote the generalized coordinates for the sagittal plane, while $\dot{\alpha}_{\mathbf{s}} = \left(\dot{u}_x, \dot{u}_y, \dot{\phi}_z\right)$ the generalized velocities.

Considering the case of a granular chain coupled to a rigid substrate, namely considering fixed boundary conditions for particle 2, we obtain $u_{2,x} = u_{2,y} = \phi_{2,z} = 0$, and then the equations of motion of a monodisperse chain, $m_0 = m$ and $R_0 = R$, take the following form:

$$m\ddot{u}_{0,x} = K_N(u_{1,x} - 2u_{0,x} + u_{-1,x}) - \tilde{K}_S(u_{0,x} - R\phi_{0,z}), \tag{2.8a}$$

$$m\ddot{u}_{0,y} = K_S(u_{1,y} - 2u_{0,y} + u_{-1,y}) - \tilde{K}_N u_{0,y} + K_S R(\phi_{-1,z} - \phi_{1,z}), \tag{2.8b}$$

$$I\ddot{\phi}_{0,z} = K_S R(u_{1,y} - u_{-1,y}) - K_S R^2(\phi_{1,z} + 2\phi_{0,z} + \phi_{-1,z}) + \tilde{K}_S R(u_{0,x} - R\phi_{0,z}). \tag{2.8c}$$

Considering the case of a free granular chain, namely considering free boundary conditions for particle 2, we obtain $u_{2,x} = u_{0,x}$, $u_{2,y} = u_{0,y}$, $\phi_{2,z} = -\phi_{0,z}$, and then the equations of motion of a monodisperse chain, $m_0 = m$ and $R_0 = R$, take the following form:

$$m\ddot{u}_{0,x} = K_N(u_{1,x} - 2u_{0,x} + u_{-1,x}), \tag{2.9a}$$

$$m\ddot{u}_{0,y} = K_S(u_{1,y} - 2u_{0,y} + u_{-1,y}) + K_S R(\phi_{-1,z} - \phi_{1,z}), \tag{2.9b}$$

$$I\ddot{\phi}_{0,z} = K_S R(u_{1,y} - u_{-1,y}) - K_S R^2(\phi_{1,z} + 2\phi_{0,z} + \phi_{-1,z}). \tag{2.9c}$$

2.2.2 Equations of motion for horizontally polarized modes

In the horizontal plane, there are also 3 degrees of freedom (1 displacement u_z, and 2 rotations ϕ_x, ϕ_y). The system is presented in Fig. 2.3, where we show the zero-th particle which is in contact with the neighboring particles -1, 1 and the substrate, denoted by particle 2. For each contact, now we consider shear and torsional couplings.

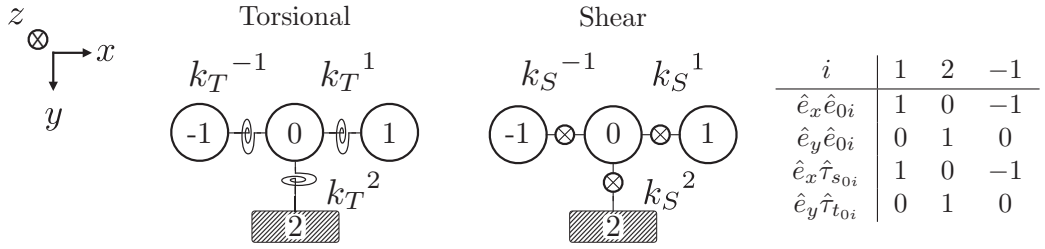

i	1	2	-1
$\hat{e}_x\hat{e}_{0i}$	1	0	-1
$\hat{e}_y\hat{e}_{0i}$	0	1	0
$\hat{e}_x\hat{\tau}_{s_{0i}}$	1	0	-1
$\hat{e}_y\hat{\tau}_{t_{0i}}$	0	1	0

Figure 2.3: Representation of the studied system for the horizontal plane.

The Lagrangian of the particle "0" is described as follows:

$$\mathcal{L}^{(0)}_{\mathbf{H}} = T^{(0)}_{\mathbf{H}} - V^{(0)}_{\mathbf{H}}, \tag{2.10}$$

where the indice "H" refers to the horizontal plane. The kinetic energy $T_{\mathbf{H}}$ and the potential energies $V_{\mathbf{H}}$

are given by:

$$T_{\mathbf{H}}^{(0)} = \frac{1}{2}m_0\dot{u}_{0,z}^2 + \frac{1}{2}I_0\left(\dot{\phi}_{0,x}^2 + \dot{\phi}_{0,y}^2\right), \tag{2.11a}$$

$$V_{\mathbf{H}}^{(0)} = \frac{1}{2}\sum_{i=-1,2,1}\left({k_S}^i\Delta {S_i}^2 + {k_T}^i\Delta {T_i}^2\right), \tag{2.11b}$$

where $i = \{-1, 2, 1\}$, the torsional and shear rigidities are ${k_T}^i = \{K_T, \tilde{K}_T, K_T\}$ and ${k_S}^i = \{K_S, \tilde{K}_S, K_S\}$ for the interaction between the zero-th particle and the i-th particle, respectively. Shear ΔS_i and torsional ΔT_i spring elongations can be explicitly written:

$$\Delta S_i = (u_{i,z} - u_{0,z}) - (R_i\phi_{i,x} + R_0\phi_{0,x})\,\hat{e}_z\hat{\tau}_{t_{0i}} - (R_i\phi_{i,y} + R_0\phi_{0,y})\,\hat{e}_z\hat{\tau}_{s_{0i}}, \tag{2.12}$$

$$\Delta T_i = (\phi_{i,x} - \phi_{0,x})\,\hat{e}_x\hat{e}_{0i} + (\phi_{i,y} - \phi_{0,y})\,\hat{e}_y\hat{e}_{0i}, \tag{2.13}$$

where $\hat{\tau}_{s_{0i}}$ is the unit vector normal to $\hat{e}_{0i}$ and $\hat{e}_y$: $\hat{\tau}_{s_{0i}} = [\hat{e}_y \cdot \hat{e}_{0i}]$ and identically $\hat{\tau}_{t_{0i}} = [\hat{e}_x \cdot \hat{e}_{0i}]$. Then, the Lagrange's equations in the horizontal plane have the following form:

$$\frac{\partial\mathcal{L}_{\mathbf{H}}^{(0)}}{\partial\alpha_{\mathbf{H}}} - \frac{d}{dt}\left(\frac{\partial\mathcal{L}_{\mathbf{H}}^{(0)}}{\partial\dot{\alpha}_{\mathbf{H}}}\right) = 0, \tag{2.14}$$

where $\alpha_{\mathbf{H}} = (u_z, \phi_x, \phi_y)$ denote the generalized coordinates for the horizontal plane, while $\dot{\alpha}_{\mathbf{H}} = \left(\dot{u}_z, \dot{\phi}_x, \dot{\phi}_y\right)$ the generalized velocities.

Similar to the sagittal case, considering the case of a granular chain coupled to a rigid substrate, namely considering fixed boundaries conditions for particle 2, we obtain $u_{2,z} = \phi_{2,x} = \phi_{2,y} = 0$, and then the equations of motion of a monodisperse chain, $m_0 = m$ and $R_0 = R$, take the following form:

$$m\ddot{u}_{0,z} = K_S(u_{1,z} - 2u_{0,z} + u_{-1,z}) - \tilde{K}_S\,(u_{0,z} - R\phi_{0,x}) + K_SR(\phi_{-1,y} - \phi_{1,y}), \tag{2.15a}$$

$$I\ddot{\phi}_{0,x} = K_T(\phi_{1,x} - 2\phi_{0,x} + \phi_{-1,x}) + \tilde{K}_SR(u_{0,z} - R\phi_{0,x}), \tag{2.15b}$$

$$I\ddot{\phi}_{0,y} = -K_SR^2(\phi_{1,y} + 2\phi_{0,y} + \phi_{-1,y}) + K_SR(u_{1,z} - u_{-1,z}) - \tilde{K}_T\phi_{0,y}. \tag{2.15c}$$

Considering the case of a free granular chain, namely considering free boundaries conditions for particle 2, we obtain $u_{2,z} = u_{0,z}$, $\phi_{2,x} = -\phi_{0,x}$, $\phi_{2,y} = -\phi_{0,y}$, and then the equations of motion of a monodisperse chain, $m_0 = m$ and $R_0 = R$, take the following form:

$$m\ddot{u}_{0,z} = K_S(u_{1,z} - 2u_{0,z} + u_{-1,z}) + K_SR(\phi_{-1,y} - \phi_{1,y}), \tag{2.16a}$$

$$I\ddot{\phi}_{0,x} = K_T(\phi_{1,x} - 2\phi_{0,x} + \phi_{-1,x}), \tag{2.16b}$$

$$I\ddot{\phi}_{0,y} = -K_SR^2(\phi_{1,y} + 2\phi_{0,y} + \phi_{-1,y}) + K_SR(u_{1,z} - u_{-1,z}). \tag{2.16c}$$

Solutions of the set of Eqs. (2.8)-(2.15) are plane waves propagating in x-direction for each family of

modes, the indices "S" and "H" respectively referring to the sagittal and to the horizontal plane:

$$\mathbf{V_n^S} = \begin{pmatrix} u_{n,x}(x,t) \\ u_{n,y}(x,t) \\ \Phi_{n,z}(x,t) \end{pmatrix} = \mathbf{v^S} e^{i\omega t - ikx_n}, \tag{2.17a}$$

$$\mathbf{V_n^H} = \begin{pmatrix} u_{n,z}(x,t) \\ \Phi_{n,x}(x,t) \\ \Phi_{n,y}(x,t) \end{pmatrix} = \mathbf{v^H} e^{i\omega t - ikx_n}, \tag{2.17b}$$

considering the new variables $\Phi_x = R\phi_x$, $\Phi_y = R\phi_y$ and $\Phi_z = R\phi_z$. Here, k is the wave number in the x-direction, $\mathbf{v}$ the amplitude vector and ω is the angular frequency. For both the horizontal and the sagittal plane, Eqs. (2.17) are developed around the equilibrium position x_0 of the central particle $\mathbf{V_n} = \mathbf{v}e^{i\omega t - ikx_0}e^{-ik\Delta x_n}$, where $\Delta x_n = x_n - x_0$ is the relative coordinate between the central particle and the n-th particle. Substituting Eqs. (2.17) into the set of Eqs. (2.8)-(2.15) leads to two eigenvalue problems:

$$\mathbf{D^S v^S} = -\Omega^2 \mathbf{v^S}, \tag{2.18}$$

$$\mathbf{D^H v^H} = -\Omega^2 \mathbf{v^H}, \tag{2.19}$$

where $\Omega = \omega/\omega_0$ is the reduced frequency with $\omega_0 = \sqrt{K_S/m}$. Elements of the 3×3 dynamical matrices $\mathbf{D^S}$ for the sagittal plane and $\mathbf{D^H}$ for the horizontal plane are

$$\mathbf{D^S} = \begin{pmatrix} -4\eta_1 \sin^2(q) - \eta_2 & 0 & \eta_2 \\ 0 & -4\sin^2(q) - \eta_3 & 4i\sin(q)\cos(q) \\ \eta_2 p & -4ip\sin(q)\cos(q) & -4p\cos^2(q) - \eta_2 p \end{pmatrix}, \tag{2.20}$$

$$\mathbf{D^H} = \begin{pmatrix} -4\sin^2(q) - \eta_2 & \eta_2 & 4i\sin(q)\cos(q) \\ \eta_2 p & -4\eta_4 p\sin^2(q) - \eta_2 p & 0 \\ -4ip\sin(q)\cos(q) & 0 & -4p\cos^2(q) - \eta_5 p \end{pmatrix}, \tag{2.21}$$

where $\eta_1 = \dfrac{K_N}{K_S}$, $\eta_2 = \dfrac{\tilde{K}_S}{K_S}$, $\eta_3 = \dfrac{\tilde{K}_N}{K_S}$, $\eta_4 = \dfrac{K_T}{K_S R^2}$, $\eta_5 = \dfrac{\tilde{K}_T}{K_S R^2}$, $p = \dfrac{mR^2}{I}$ and $q = \dfrac{ka}{2}$, where $a = 2R$ corresponds to the lattice constant. Solutions to these eigenvalue problems Eqs. (2.18)-(2.19) yield the $\Omega(k)$ dispersion relation. The ratio p characterizes the mass distribution in a spherical particle. In our model we consider homogeneous particle ($p = 2.5$) but by modifying this ratio the dispersion curves could be strongly modified. Two cases are studied, the first where the chain is not coupled to a substrate, denoted as " free " chain and the second when the coupling with a substrate is taken into account, denoted as "coupled" chain.

2.2.3 "Free" linear granular chain

In this section we consider the case where the chain is not coupled to a substrate, namely $\tilde{K}_N = \tilde{K}_S = \tilde{K}_T = 0$. Particles are interacting only via normal K_N, shear K_S and torsional K_T stiffnesses. Solving eigenvalue problems Eqs. (2.18)-(2.19) gives the $\Omega(k)$ dispersion relation for each of the two planes, and the analysis is restricted to the first Brillouin zone for waves propagating to the right ($k > 0$). In Fig. 2.4, theoretical dispersion curves are presented for each plane, the sagittal with u_x, u_y and ϕ_z components and the horizontal with u_z, ϕ_x and ϕ_y. The characteristics of the particles and pre-compressional force are related to experimental relevant values. The pre-compressional force between spheres is equal to the experimentally measured one, $F_0 = 1$ N, and particles are chosen to be stainless steel beads with a diameter of 15.875 mm (material characteristics are presented in section 2.3). Eqs. (1.4)-(1.9) therefore yield $K_N = 6.60{\cdot}10^6$ N/m, $K_S = 5.44{\cdot}10^6$ N/m, $K_T = 1.12{\cdot}10^{-2}$ m·N and $K_S R^2 = 3.42{\cdot}10^2$ m·N $\approx 3{\times}10^4\ K_T$.

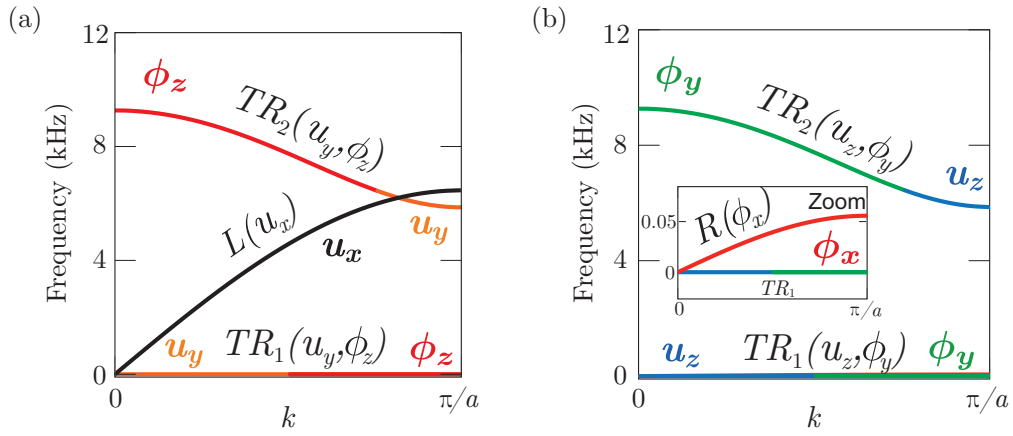

Figure 2.4: Dispersion curves for the infinite free granular chain considering the static force $F_0 = 1$ N and $\tilde{K}_N = \tilde{K}_S = \tilde{K}_T = 0$ for (a) modes polarized in the sagittal plane and (b) modes polarized in the horizontal plane.

The dispersion relation for the sagittal plane, see Fig. 2.4(a), contains three branches: one corresponds to the longitudinal mode with displacement just along the x-axis, denoted as $L(u_x)$, while the other two correspond to transverse-rotational mode, denoted as $TR_{1,2}(u_y, \phi_z)$ with displacements along the y-axis and rotations along the z-axis. TR_1 is a zero-frequency branch resulting from the counterbalance between rotational and transverse motions; further details on zero-frequency TR branches can be found in Refs. [88] and [62]. The component predominance in the TR branches is determined by identifying the largest component of the calculated eigenmodes of Eq. (2.18), as denoted in 2.4(a). For example, in the lower part of the TR_2 branch, the predominant component is u_y, while it is ϕ_z in the upper part.

The dispersion relation for the horizontal plane, see Fig. 2.4(b), contains two TR branches, denoted $TR_{1,2}(u_z, \phi_y)$, and one branch corresponding to torsional modes, denoted as $R(\phi_x)$. This branch is at very low frequencies due to the small value of the torsional stiffness K_T, compared to the effective rotational stiffness $K_S R^2$ provided by shear interactions. TR_1 is also a zero-frequency branch due to the counterbalance between rotational and transverse motions, while $TR_2(u_z, \phi_y)$ is similar to the $TR_2(u_y, \phi_z)$ of the sagittal plane. This result stems from the symmetry of the rotational ϕ_z, ϕ_y and transverse u_y, u_z motions

of the free-standing granular chain, Fig. 2.1.

Fig. 2.5 presents the presence of one component in comparison with the two others for each mode by plane. The presence of the component is displayed in grey scale. Colors white and black correspond to absence and pure existence of the component, respectively.

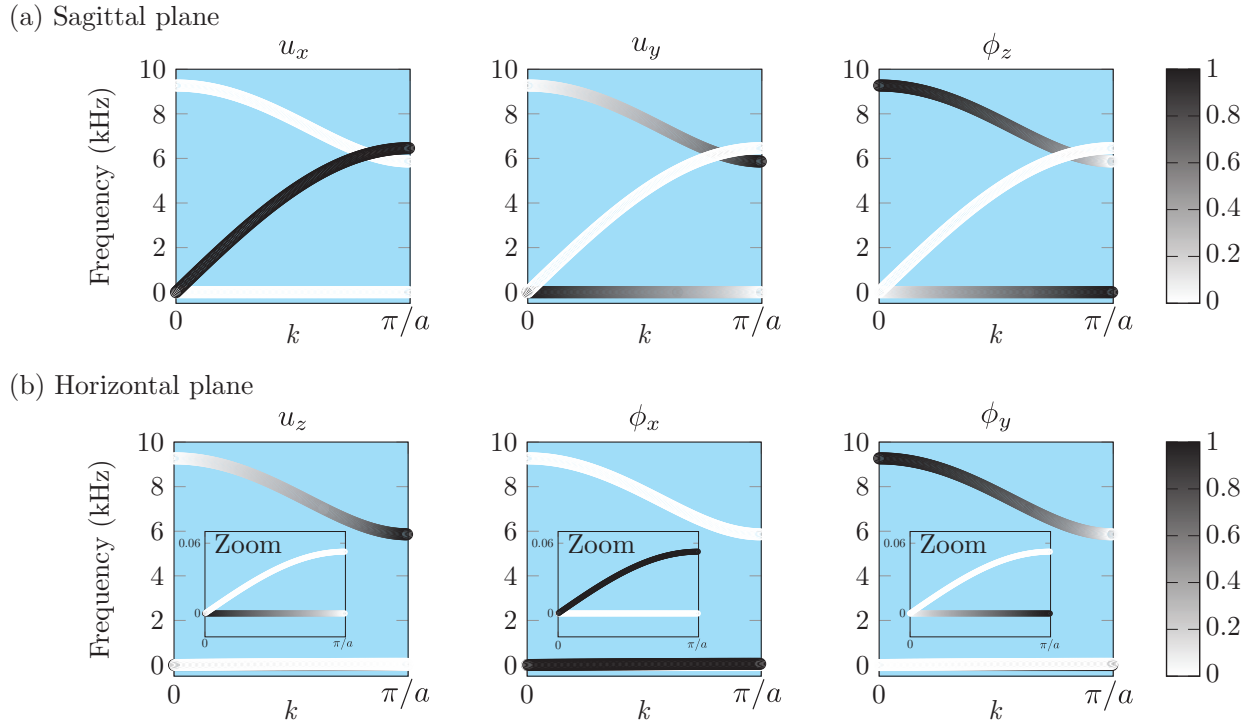

Figure 2.5: Relative amplitude of the components for each mode polarized in (a) sagittal and (b) horizontal planes for the free granular chain. Colors white and black correspond to absence (0) and pure existence (1) of the component, respectively.

Fig. 2.5(a), depicts the predicted branches; one pure $L(u_x)$ and two coupled $TR(u_y, \phi_z)$. The upper part of the higher TR branch becomes more and more rotational meanings that experimentally it will be more difficult to detect translational motion in this part. From Fig. 2.5(b), identical conclusions can be made, we see the pure rotational branch $R(\phi_x)$ and the two other $TR(u_z, \phi_y)$ branches with the same behavior.

In order to quantitatively express the interplay between transverse (u) and rotation (ϕ) components in the upper branches TR_2, Fig. 2.6 presents the relative amplitude of each component as a function of the frequency. We can clearly see that the transverse component is quickly reducing as the frequency is increasing.

Analytical values of cutoff frequencies of modes are explicitly given for modes polarized in the sagittal plane (u_x, u_y, ϕ_z) as follows for $k = 0$:

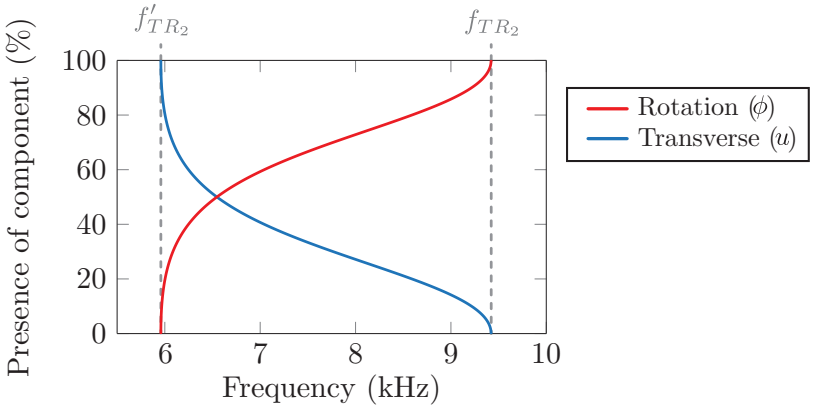

Figure 2.6: Relative amplitude (in percentage) of transverse (u) and rotation (ϕ) in the TR_2 branch as a function of the frequency. Dashed line corresponds to the lower and higher cutoff frequencies for the TR_2 branch.

$$f_L = 0, \tag{2.22}$$

$$f_{TR_1} = 0, \tag{2.23}$$

$$f_{TR_2} = \frac{1}{2\pi}\sqrt{\frac{4K_S R^2}{I}}, \tag{2.24}$$

while for $k = \pi/a$:

$$f'_L = \frac{1}{2\pi}\sqrt{\frac{4K_N}{m}}, \tag{2.25}$$

$$f'_{TR_1} = 0, \tag{2.26}$$

$$f'_{TR_2} = \frac{1}{2\pi}\sqrt{\frac{4K_S}{m}}. \tag{2.27}$$

For modes polarized in the horizontal plane (u_z, ϕ_x, ϕ_y), cutoff frequencies of the TR branches are identical than in the sagittal plane due to symmetry consideration. The cut-off frequency of the pure rotational branch $R(\phi_x)$ for $k = 0$ is $f_R = 0$ and for $k = \pi/a$:

$$f'_R = \frac{1}{2\pi}\sqrt{\frac{4K_T}{I}}. \tag{2.28}$$

After the study of freely-standing chain, the theoretical study of the granular chain coupled with a rigid substrate is now considered.

2.2.4 Linear granular chain coupled with a rigid substrate

This section focuses on the linear chain coupled with a rigid substrate, the normal $\tilde{K}_N$, shear $\tilde{K}_S$ and torsional $\tilde{K}_T$ are now activated. Fig. 2.7 shows some cases of the dispersion relation of the structure within the first Brillouin zone for waves propagating to the right ($\Re(k) > 0$), varying the η_2 ratio, which

corresponds to modifying the shear rigidity $\tilde{K}_S$ between bead and substrate. The choice to consider $\tilde{K}_S$ as a free parameter is discussed in the experimental section 2.3.3. Values of other parameters are $\eta_1 = 1.21$, $\eta_3 = 1.89$, $\eta_4 = 8.18 \cdot 10^{-5}$ and $\eta_5 = 2.14 \cdot 10^{-4}$. These correspond to experimental relevant values taking into account the Hertzian theory (see section 1.4) and estimated forces between spheres equal to $F_0 = 4$ N and between sphere and substrate $F = 10$ N. In panels presented in columns 1 and 3, we plot the dispersion relation of sagittally polarized waves that include longitudinal motion (u_x), transversal motion along y-direction (u_y) and rotational motion around z-axis (ϕ_z), while in panels in columns 2 and 4, we display the dispersion relation of horizontal polarized waves that include transversal motion along z-direction (u_z) and rotational motions around x-axis (ϕ_x) and y-axis (ϕ_y). The predominance of each motion is labeled in Fig. 2.7.

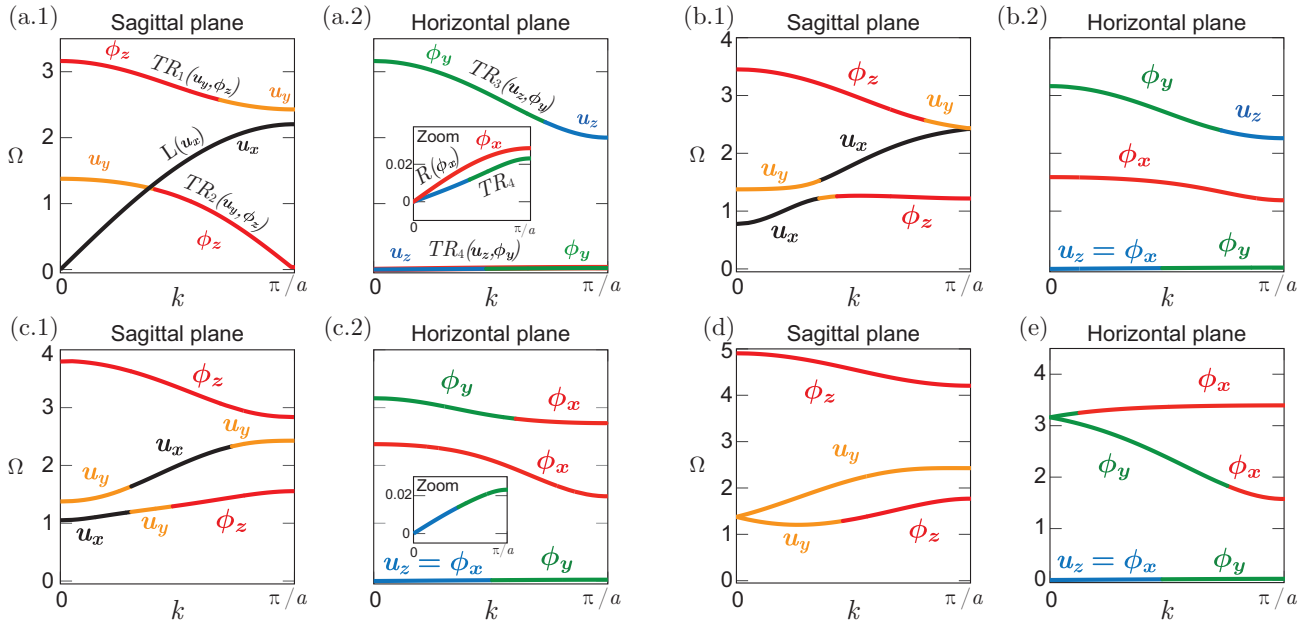

Figure 2.7: Dispersion curves of an infinite granular chain coupled to a rigid substrate, as a function of the free parameter $\eta_2 = \tilde{K}_S/K_S$. (a) $\eta_2 = 0$, no shear coupling, (b) $\eta_2 = 0.72$ (c) $\eta_2 = 1.60$ corresponds to the Hertz prediction with the force created by the magnet of B_r (1.37 T) remanent magnetization, (d) $\eta_2 = 4.56$ (e) $\eta_2 = 2.86$. Values of other parameters are $\eta_1 = 1.21$, $\eta_3 = 1.89$, $\eta_4 = 8.18 \cdot 10^{-5}$ and $\eta_5 = 2.14 \cdot 10^{-4}$. $\Omega = \omega/\omega_0$ is the reduced frequency with $\omega_0 = \sqrt{K_S/m}$.

In Fig. 2.7(a.1-2) we consider the case where the granular chain is coupled to a substrate only through the $\tilde{K}_N$ and $\tilde{K}_T$, namely $\tilde{K}_S = 0$. For the sagittal plane motion, the longitudinal branch $L(u_x)$, with displacement only along the x-axis, is uncoupled to two other transversal-rotational branches denoted by $TR_{1,2}(u_y, \phi_z)$, with displacement along y-axis and rotation around the z-axis. Similarly, a pure rotation branch $R(\phi_x)$ is uncoupled to two $TR_{3,4}(u_z, \phi_y)$. We have to notice that the $TR_{1,2}$ and $TR_{3,4}$ are not identical between the sagittal (x,y) and horizontal (x,z) plane.

When the shear coupling between the chain and the rigid substrate is activated, each branch in the dispersion diagram contains all components of the relevant mode family. In Fig. 2.7(b.1-2) we consider the case of $\eta_2 = 0.72$. According to analytical expressions for frequencies of the modes at $k = \pi/a$ in the sagittal plane, this corresponds to the case where two branches degenerate at the edge of the Brillouin zone.

For this case, we also observe that the first two branches in the sagittal plane show an anti-crossing effect which leads to the existence of a zero group velocity (ZGV) mode at a finite wavelength, $k \approx \pi/(2a)$. In particular, increasing the parameter η_2 from zero to a finite value, we observe that the dominant component of the first branch, at the crossing point with the second branch, is not the longitudinal u_x any more but the transversal u_y. This explains the avoided crossing of these two branches and the existence of a ZGV mode. One can also observe the existence of a band gap from zero up to the value Ω_1 (expressed later in Eq. (2.30)). Since this value depends on the free parameter η_2, it can be tuned by the shear coupling between the granular chain and the substrate. In Fig. 2.7(c.1-2), we present the case using values of stiffnesses given by the Hertz prediction and considering force created by the magnet $B_2 = 1.37$ T, thus $\eta_2 = 1.60$. Three branches in each plane are smooth and they do not exhibit ZGV. In Fig. 2.7(d) and Fig. 2.7(e), we consider cases for $\eta_2 = 4.56$ (sagittal plane) and $\eta_2 = 2.86$ (horizontal plane) respectively. Accidental degeneracies at $k = 0$ are present in both cases as well as a ZGV mode at $k \approx 0.26\pi/a$ (Fig. 2.7(d)).

Analytical values of cutoff frequencies of modes at $k = 0$ and $k = \pi/a$ are explicitly given for modes polarized in the sagittal plane (u_x, u_y, ϕ_z) as follows for $k = 0$,

$$\Omega_2^{\mathbf{s2}} = \eta_3, \tag{2.29}$$

$$\Omega_{1,3}^{\mathbf{s2}} = \frac{1}{2}\left[4\eta_1 + \eta_2(1+p) \pm \sqrt{(4\eta_1 + \eta_2(1+p))^2 - 16\eta_1\eta_2 p}\right], \tag{2.30}$$

while for $k = \pi/a$

$$\Omega_1^{\mathbf{s'2}} = 4 + \eta_3, \tag{2.31}$$

$$\Omega_{2,3}^{\mathbf{s'2}} = \frac{1}{2}\left[4\eta_1 + \eta_2(1+p) \pm \sqrt{(4\eta_1 + \eta_2(1+p))^2 - 16\eta_1\eta_2 p}\right]. \tag{2.32}$$

For modes polarized in the horizontal plane (u_z, ϕ_x, ϕ_y), one has for $k = 0$,

$$\Omega_1^{\mathbf{H2}} = 0, \tag{2.33}$$

$$\Omega_2^{\mathbf{H2}} = \eta_2(1+p), \tag{2.34}$$

$$\Omega_3^{\mathbf{H2}} = p\Big(4 + \eta_5\Big), \tag{2.35}$$

while for $k = \pi/a$,

$$\Omega_1^{\mathbf{H'2}} = \eta_5 p, \tag{2.36}$$

$$\Omega_{2,3}^{\mathbf{H'2}} = \frac{1}{2}\Big(4\eta_4 p + \eta_2(1+p) + 4 \pm \Big[(4\eta_4 p + \eta_2(1+p) + 4)^2 - 16p(4\eta_4 + \eta_2 + \eta_2\eta_4)\Big]^{1/2}\Big). \tag{2.37}$$

To conclude this section, we emphasize that the granular chain coupled to a rigid substrate results in rich dispersion behavior including ZGV modes at finite wavelength and accidental degeneracy.

2.2.5 Summary

In considering all degrees of freedom in transversal and rotational motions, the full set of dispersion relations has been derived for the case of free-standing granular chain and of a chain interacting with a substrate. The dispersion curves are presented in two decoupled planes, called sagittal (u_x, u_y, ϕ_z) and horizontal (u_z, ϕ_x, ϕ_y).

When the chain is not coupled to a substrate, the dispersion curves show two pure branches. One corresponding to longitudinal motion $L(u_x)$ and one to pure rotational motion $R(\phi_x)$. For each considered plane, two other coupled transverse-rotational TR branches are also present whose one is at zero frequency.

Considering a coupling of the beads with a substrate, there is no more pure branches and the modes are containing all components of the relevant plane. By modifying only the shear rigidity between bead and substrate, theoretical dispersion curves have shown that our system supports transversal/rotational propagation modes, zero group velocity (ZGV) modes and accidental degeneracies. Dispersion engineering by tuning some of contact stiffnesses can thus lead to interesting wave phenomena. In order to improve the modeling, the bending rigidity could be added to the study as in [62, 71, 99].

2.3 Linear spectra : experimental results and discussion

The objective of this section is to demonstrate the validity of the model via two different experimental setups using external magnetic field to induce forces in a granular chain. The first one is a free-standing chain where couplings between a substrate and beads can be neglected. The second setup corresponds to the case where the chain is coupled to a substrate.

In both cases, experimental setups are composed of a chain of stainless steel beads of 15.875 mm diameter, above permanent NdFeB magnets in a linear array configuration. The two setups differ by the presence or not of a soft substrate between beads and magnets.

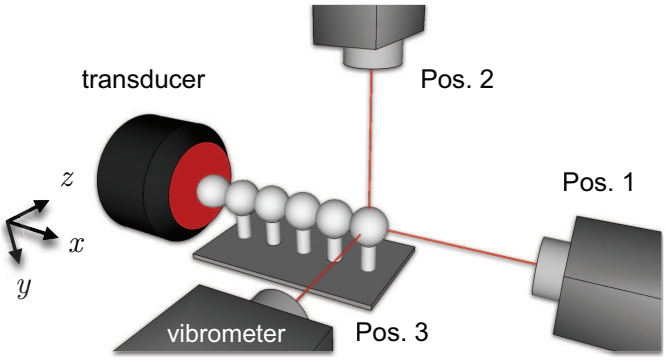

Figure 2.8: Schematics of the experimental setup. The configuration allows us to drive the chain along x, y or z directions. We place the vibrometer in 3 different positions, Pos. 1, 2 and 3 to detect displacement along the x, y and z axis, respectively.

The material characteristics of steel 440C beads are the following: density 7650 kg/m^3, Young's modulus $E_1 = 200$ GPa and Poisson ratio $\nu_1 = 0.3$. The magnets have a density of 7600 kg/m^3, a Young's modulus $E_2 = 160$ GPa, a Poisson ratio $\nu_2 = 0.24$ and a remanent magnetization $B_1 = 1.32$ T or $B_2 = 1.37$ T. The chain is driven at one extremity in three independent directions (x,y,z) by using two kinds of transducers (a longitudinal *Panametrics* V3052 and a shear *Panametrics* V1548). The schematics of the setup describing the complete measurement chain is presented in Fig. 2.9. A bead is glued to the exciting transducer to ensure the same contact between the driver (the glued bead) and the chain. The excitation signal is a sweep sine of 65 s duration with a span from 100 Hz to 15 kHz. The measurement of the particle velocity is made by a laser vibrometer *Polytec* OFV-503 with a sensitivity of 5 mm/s/V and an averaging is performed during the acquisition. We place the laser vibrometer in three different positions to be able to detect all directions of displacement of the bead. Experimental setup configurations are presented in Fig. 2.8.

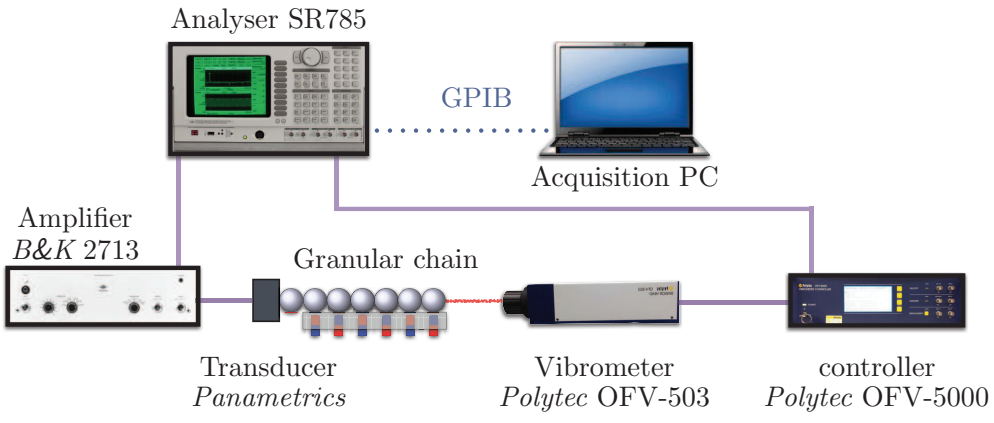

Figure 2.9: Diagram of the instrumentation.

A first measurement on the particle glued to the transducer is performed to ensure that the amplitude of excitation is in the linear regime. Thus calculating the ratio between the driven displacement and the theoretical static overlap leads to $\delta/\delta_0 \leqslant 0.019$ for all configurations present in this chapter. The most unfavorable case, when this ratio is equal to 0.019, can still be consider as linear regime and as a results we are sure to excite the chains in a linear regime. Before each set of measurement, beads are cleaned with acetone and placed carefully without touching directly the material with the skin finger.

2.3.1 "Free" linear granular chain

This section describes the experimental observations in a magneto-granular chain. Soft rubber has been chosen as a substrate in order to ensure high impedance contrast between the granular chain and the substrate. As such their mechanical coupling is weak while the remaining energy leakage from the beads to the substrate is highly attenuated due to the high viscoelasticity of rubber. In other words, the effective stiffness originating from contact deformation between spheres and the substrate is more than four order of magnitude smaller relative to the contact stiffnesses between spheres. It can thus be assumed that the granular chain is free, coupling with the substrate can be ignored. Permanent magnets are NdFeB cylinders of remanent magnetization $B_2 = 1.37\ T$, located 10 mm from the center of the spheres. For this case, as mentioned above, the measured static normal force is $F_0 = 1\ \pm\ 0.15$ N. Eqs. (1.4)-(1.9) therefore yield $K_N = 6.60{\cdot}10^6$ N/m, $K_S = 5.44{\cdot}10^6$ N/m, $K_T = 1.12{\cdot}10^{-2}$ m·N and $K_S R^2 = 3.42{\cdot}10^2$ m·N $\approx 3{\times}10^4\ K_T$. A schematic diagram of the chain on top of permanent magnets within a rubber substrate is presented on Fig. 2.10.

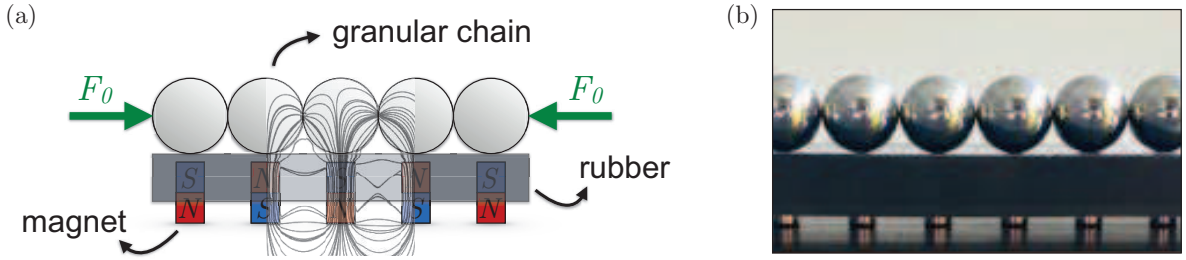

Figure 2.10: (a) Schematic diagram of the granular chain on top of permanent magnets within a rubber. Forces and magnetic flux lines induced by the magnetic field have been superimposed. (b) Photography of the experimental setup for the "free" chain configuration.

In Fig. 2.10, magnetic flux lines have been superimposed on the schematic diagram of the setup. These lines have been calculated using FEM simulations, a large concentration of lines is visible at the contacts, which indicates the attractive normal force between adjacent spheres and between spheres and substrate. Using Eqs. (2.18-2.19) theoretical dispersion curves are obtained for each plane (sagittal and horizontal) and are displayed on Fig. 2.11 along with the experimentally derived linear spectra. Measurements are performed on the last bead of the chain in the same direction as the excitation polarization. Pos. 1 for measurement along the x-axis, Pos. 2 along the y-axis, and Pos. 3 along the z-axis. The granular chain is composed of 5 (center panel) or 15 particles (right panel).

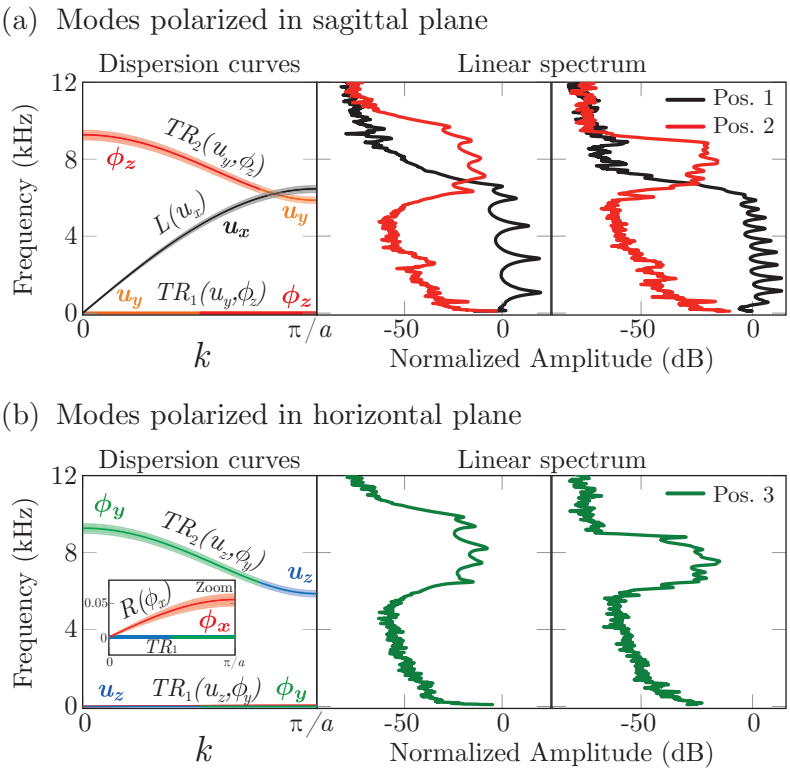

Figure 2.11: Dispersion curves (left) for the infinite free granular chain when considering the experimentally measured $F_0 = 1$ N (solid line) with an error of ± 0.15 N (shadow zone). The linear spectrum of the signal (velocity amplitude) detected by the laser vibrometer for a chain composed of 5 beads (center) and 15 beads (right) (a) in the sagittal plane (x,y), and (b) in the horizontal plane (x,z). For both chains, permanent magnets of $B_2 = 1.37$ T remanent magnetization have been used.

From a direct comparison, a very good agreement can be observed between theoretical and experimental findings on the allowed and forbidden band of propagation. In addition, the appearance of upper branches in experiments provides evidence of the existence of coupled transverse/rotational branches. The pure torsional branch $R(\phi_x)$ cannot be detected by the laser vibrometer. Indeed the laser vibrometer, being sensitive to changes in the optical path length, it permits to detect motion of the reflecting surface only along the optical beam direction. The zero frequency branches TR_1 presents theoretically in both planes are not excited in this experimental configuration and as results they cannot be measured. In the case of a 5-bead chain (central panels of Fig. 2.11), the 5 resonances in each branch are clearly visible. In the case of a 15-bead chain and under longitudinal excitation (right panels of Fig. 2.11 - Pos.1), only the first 10 resonances can be distinguished. This result offers evidence that increasing the system length strengthens the dissipation effect, especially around the edges of propagating bands. Furthermore, at high frequencies under both longitudinal and shear excitation, the corresponding propagating wavelengths are on the order of the lattice constant. Hence, a small amount of disorder induced by bead misalignments could lead to a stronger smearing of the relevant resonances.

With the validity of the theoretical model now verified, let's continue with a demonstration of the tunability of the "free" linear granular chain by external magnetic field.

2.3.2 Tunable "Free" linear granular chain by external magnetic fields

Analytical expressions of the contact stiffnesses have been presented in section 1.4 where we notice a nonlinear relation of the static force F_0 between particles and the stiffnesses. It has been also presented in the previous chapter, the dependence of the static force between spheres with the strength of the magnetic field. Finally, by changing F_0, which in our case is equivalent to change the strength of the magnetic field induced by the permanent magnets, we can tune the dispersion relation of our "free" granular chain. Plotting the analytical cutoff frequencies of the L and TR branches as a function of the static force F_0 permits to show the allowed and forbidden bands of propagation. Explicit expressions of cutoff frequencies are given for the L and TR branches in Eq. (2.25) and Eqs. (2.24, 2.27), respectively. Fig. 2.12 depicts the expected theoretical cutoff frequencies using two permanent magnets of B_1 and B_2, which correspond to $F_0 = 0.3$ N and $F_0 = 1$ N experimentally estimated, respectively.

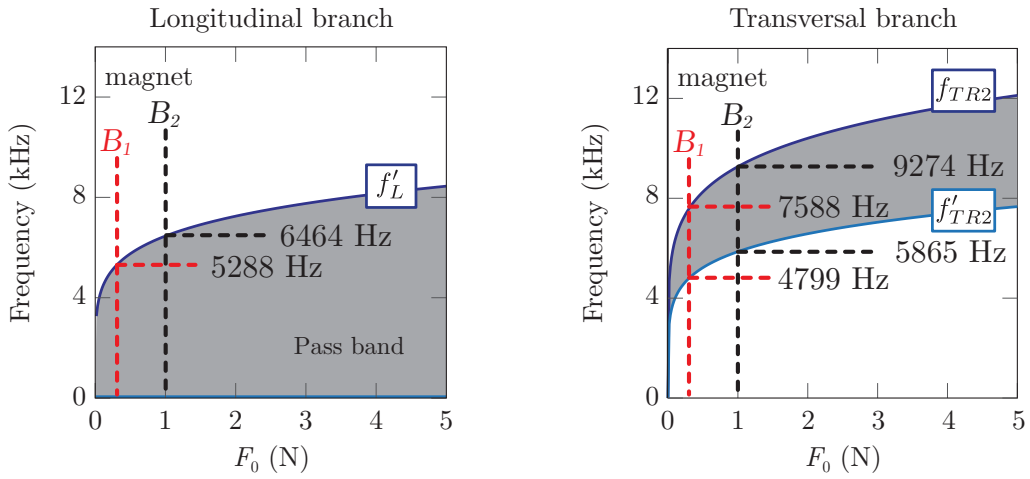

Figure 2.12: Cutoff frequencies for the L (left) and TR (right) branches as function of the normal force F_0. Experimentally estimated forces are $F_0 = 0.3$ N (dashed red) and $F_0 = 1$ N (dashed black) for permanent magnets of B_1 and B_2 remanent magnetization, respectively, both placed a distance 10 mm from the center of the beads. Grey zones correspond to pass bands. The torsional cutoff frequency is not shown.

In Fig. 2.12, dashed lines denote the experimentally measured force of each magnet B_1 and B_2 with their predicted theoretical values of cutoff frequencies. Band structure tunability is observed by changing the remanent magnetization. More specifically, using the B_1 permanent magnets instead of the B_2 magnets reveals a downshift of band edges of roughly 18%.

Fig. 2.13 shows on the same plot the experimental linear spectra of a chain composed of 15 beads, placed 10 mm above the linear array of permanent NdFeB magnets of B_1 (red line) and B_2 (black line), respectively. In the former case, introducing the experimentally measured $F_0 = 0.3$ N into Eqs. (1.4)-(1.9) yields to $K_N = 4.42 \cdot 10^6$ N/m, $K_S = 3.64 \cdot 10^6$ N/m, $K_T = 3.34 \cdot 10^{-3}$ m·N and $K_S R^2 = 2.29 \cdot 10^2$ m·N $\approx 10^5\ K_T$. Dashed lines denote predicted theoretical values of cutoff frequencies.

For the longitudinal branch $L(u_x)$, very good agreement is found for the cutoff frequencies depending on the force created by the magnetic field. Both TR branches detected when there are B_2 magnets (black line) give also a good agreement. For TR branches into magnetic field created by B_1 magnets, the high

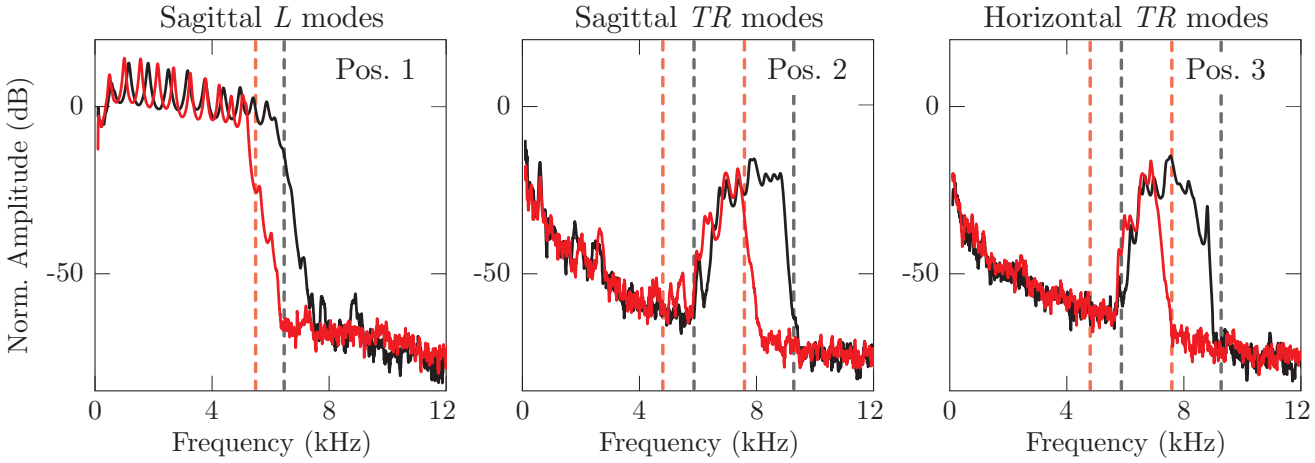

Figure 2.13: Linear spectrum of the velocity signal received for a chain of 15 beads under B_1 (red) and B_2 (black) permanent magnets at a distance of 10 mm from the center of the spheres. In the left panel, the dashed lines correspond to analytical cutoff frequencies of the longitudinal branch Eq. (2.25) along with the experimentally estimated forces. The dashed line in both the center and right panels shows the expected analytical transverse cutoff frequencies from Eqs. (2.24) and (2.27).

cutoff frequency is well predicted but it seems that the low cutoff is underestimated. For these low cutoff frequencies, the corresponding propagating wavelengths are on the order of the lattice period. Thus, small disorder in bead alignment could lead to smearing of the modes. This disagreement will be more discussed in the section 2.4.4 where the experimental dispersion curves are estimated.

The theoretical model is validated for the case of linear granular chain submitted to a magnetic field induced by permanent magnets. The assumption which consists of neglecting interactions between beads and rubber substrate is confirmed by the experimental results. Tunability by an external magnetic field is also demonstrated in such configuration. We can now turn to the case of a linear chain coupled with a substrate.

2.3.3 Linear granular chain coupled with a rigid substrate

This section describes experimental observations of the dispersive modes in a magneto-granular chain influenced by the coupling with a substrate. To ensure strong coupling of the chain with a substrate, beads are placed directly in contact with permanent neodymium NdFeB magnets. Magnets are glued on the bottom to a rigid metallic support. A schematic diagram of the chain in direct contact with the top of permanent magnets is presented in Fig. 2.14. Magnets with $B_2 = 1.37$ T remanent magnetization are used in this section. Precompressional forces F are created between beads and the magnets and have been estimated by finite element simulation to be $F = 10$ N. The interaction force between beads is experimentally measured 20 times to average the results using a dynamometer. We find an interparticle force between 2 N $< F_0 <$ 4.5 N with a mean value at 2.9 N. Between each measurement, beads are removed from the substrate and cleaned. The different values found for the force come from the slight variations of the bead positions relative to the center of the magnets making the magnetization of beads

slightly different. The roughness of the magnets could also influence this result (more details on the roughness can be found at the end of this section).

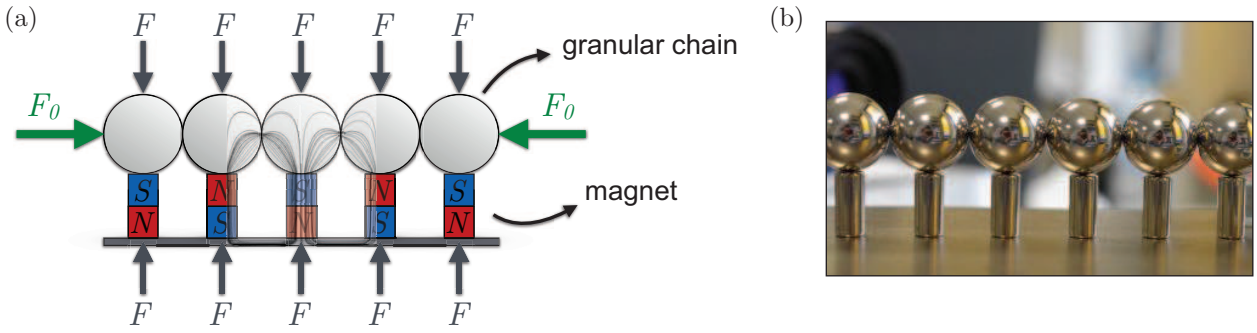

Figure 2.14: (a) Schematic diagram of the granular chain put directly on top of permanent magnets. Forces and magnetic flux lines induced by the magnetic field have been superimposed. (b) Photography of the experimental setup for the granular chain coupled to a substrate.

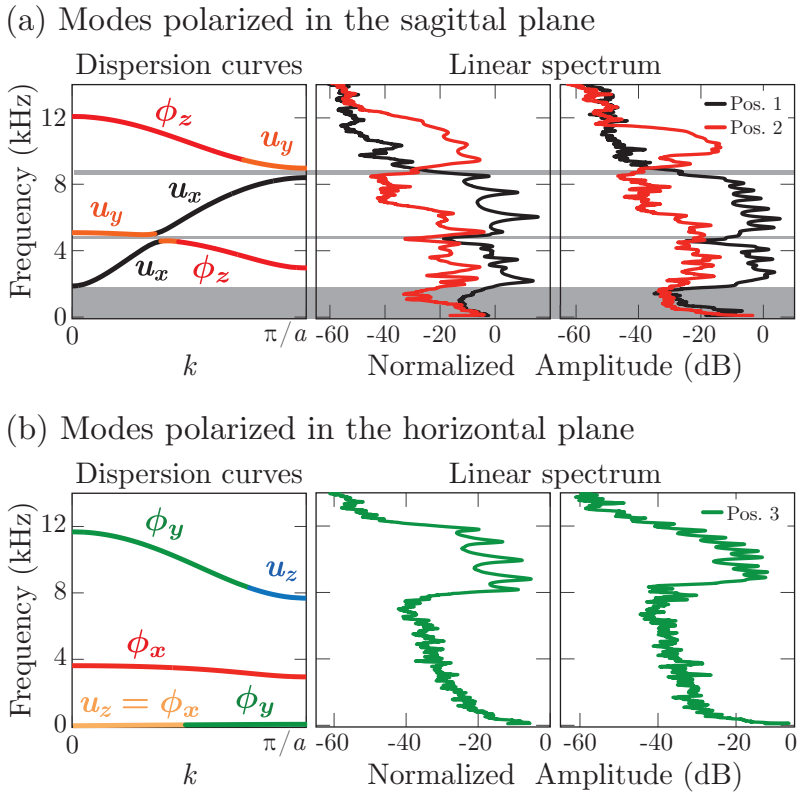

Figure 2.15: Dispersion curves (left) for the infinite granular chain considering the experimentally measured and estimated forces $F_0 = 4$ N (K_N, K_S, K_T), $F = 10$ N ($\tilde{K}_N$, $\tilde{K}_T$) and experimentally fitted $\tilde{K}_S$. Linear spectrum of the signal (velocity amplitude) detected by the laser vibrometer for a chain composed of 5 beads (center) and 15 beads (right) (a) in the sagittal plane (x,y) and (b) in the horizontal plane (x,z). The measurement is made on the last bead of the chain. We measure in the same direction than the polarization of the excitation. Pos. 1 (black line) measurement along x-axis, Pos. 2 (red line) along y-axis, and Pos. 3 (green line) along z-axis. The grey zones correspond to the theoretical forbidden propagation band-gaps.

Panels in the center and right of Fig. 2.15 present experimental results of a chain with 5 and 15 beads respectively, on top of cylindrical permanent magnets. From the dispersion curve presented in

Fig. 2.7(c.1-2) which considers the predicted stiffnesses by Hertz theory, we expect a large forbidden band of propagation from 0 up to 3880 Hz for the longitudinal motion (u_x). The width of this forbidden gap is governed mostly by the shear rigidity between each bead and the substrate, see Eq. (2.30). The Hertzian prediction of the shear rigidity considering a normal load of $F = 10$ N gives $\tilde{K}_S = 1.38 \cdot 10^7$ N/m. As we can see on the middle panel of Fig. 2.15(a), (linear spectrum measured in the Pos. 1 which is sensitive to u_x motion) the experimentally measured band gap is up to 1870 Hz. Considering the shear stiffness between the granular chain and the substrate as a free parameter, this band gap is produced by using $\tilde{K}_S = 2.36 \cdot 10^6$ N/m, namely an order of magnitude smaller. A similar discrepancy of the shear stiffness (Hertzian expected and experimentally measured) has been also observed in [120], for the case of micro-sized silica particles. Using this fitted parameter for $\tilde{K}_S$, a very good agreement between experimental results and the predicted allowed and forbidden bands of propagation is achieved. In particular, three band gaps (denoted by the grey area in Fig. 2.15(a)) have been observed. At $f = 4570$ Hz, a dip in the linear spectrum is noticed (a narrow band gap) to be in agreement with the frequency gap around the theoretical ZGV mode for $k \approx 0.38\pi/a$. This is an experimental evidence of the existence of ZGV mode. For modes polarized in the horizontal plane, the lowest branch can not be excited by our transducer so we can not measure it. The middle branch of the dispersion relation curve has a very strong predominance of rotation (ϕ_x) and only a small translation component, in this case less than 15%. Thus, it can not be detected by the laser vibrometer which permits to detect motion of the reflecting surface along the optical beam direction.

The difference between the Hertzian predicted shear stiffness, which is obtained considering smooth surfaces in contact, and the experimentally calculated one could be explained by the rough surface of permanent magnets. Measurement with an Atomic Force Microscopy (AFM) helps in characterizing the surface roughness. The AFM consists of a cantilever with a tip serving as a probe to scan a sample surface. A schematics of the AFM principle is presented in Fig 2.16(a). Experimentally, we scan the top of several magnets to find roughness properties. This technique can give the height of the asperities which is around 0.2-0.3 μm in our case, see Fig. 2.16(b-c). We also measured an averaged distance between asperities of around 2-3 μm. In comparison, the static overlap between spheres and magnets predicted by the Hertzian theory from Eq. (1.2) using the experimentally evaluated value of the static load $F = 10$ N is $\delta_0 = 0.9$ μm and the contact radius from Eq. (1.1) is $r_c = 85$ μm. Thus, the contact between spheres and magnets can be considered as a multicontact interface. In this case, as it has been shown in [121, 122], the shear stiffness varies proportionally to the normal load F,

$$\tilde{K}_S = \frac{F}{\lambda}, \tag{2.38}$$

where λ is an elastic length that lies in the micrometer range, and which is the relevant scale for the roughness of the surfaces. In our case, considering $\lambda = 3$ μm (the average distance between asperities) and $F = 10$ N, we obtain $\tilde{K}_S = 3.3 \cdot 10^6$ N/m, very close to the experimentally obtained value. On the other hand, considering now the interaction between spheres with a static load $F_0 = 4$ N, we obtain a static

overlap equal to 0.55 μm and a contact radius equal to 47 μm. The roughness of the steel 440C beads is provided to be 0.025 μm, much smaller than the static overlap predicted by the Hertzian theory using the experimentally evaluated values of the static loads F and F_0. Thus, as a first approximation the contact between the beads can be considered as a single contact.

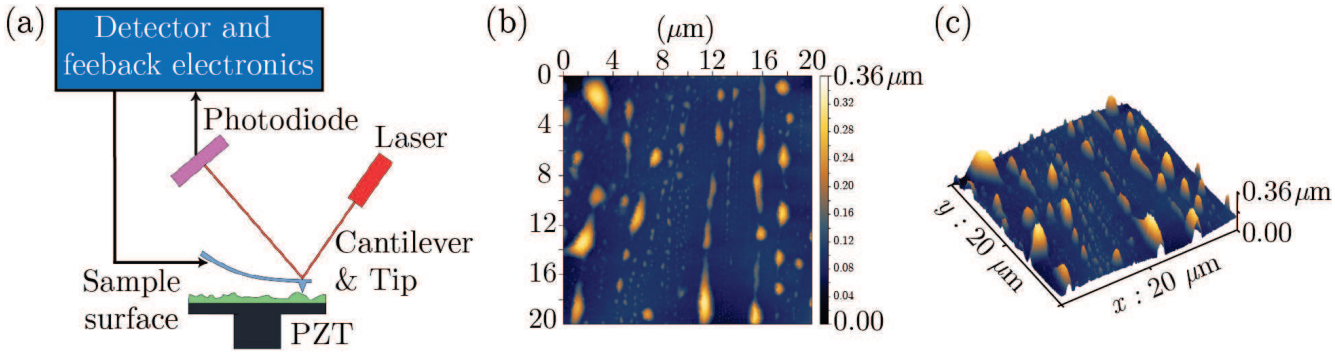

Figure 2.16: (a) Principle of Atomic Force Microscopy. Topography of the magnet surface measured by Atomic Force Microscopy (b) in 2D and (c) 3D representation.

Another point that should be commented is the fact that the magnets are fixed to one extremity (glued to the substrate) and free to move at the other extremity where the beads are located. Magnets can partially follow the bead motion, and as a consequence, the shear rigidity between bead and magnet is not completely activated. By FEM simulations we found that the first flexural mode of the cylindrical magnet is around 3.4 kHz clearly different from 4.4 kHz which is one of the gaps around the ZGV in Fig. 2.15(a). Thus the gap cannot be caused by the hybridization of the chain modes with the vibrations of the magnets. To further test this assumption, we performed experiments using shorter cylindrical magnets of 4 mm height and the same magnetization. FEM simulations predict the first flexural mode to be at 22.7 kHz, but once again the $\tilde{K}_S$ is weaker than the Hertzian predicted value. Thus, we believe that this disagreement in the $\tilde{K}_S$ is connected with the multicontact interface between the surface of the magnet and the sphere. This actually reveals another important feature in the proposed configuration: the tunability of the shear stiffness and thus of the dispersion relation by properly designed surface topographies. The latter can be produced either through a slow etching process using H_2 plasma [120] or by controlled abrasive powder coating [122].

2.3.4 Summary

This section has presented the development and dynamics of a magneto-granular phononic crystal, composed of spherical ferromagnetic spheres in contact, in the presence of a properly designed magnetic field. We developed two experimental setups with very different interaction properties between beads and a substrate.

The first experimental setup is composed of permanent magnets arranged in a row inside a soft rubber holder at a given distance from the granular chain. The effective stiffness originating from contact

deformation between spheres and soft rubber substrate is very small relative to the contact stiffnesses between spheres. In a first approximation, the coupling between the chain and the rubber substrate can be neglected, and the system considered as a free granular chain, as confirmed by the experimental results. They also reveal clearly the existence of TR modes and tunability of the dispersion relation upon external magnetic fields.

The second experimental setup taking into account the interaction with a substrate is composed of spherical ferromagnetic spheres in direct contact with permanent magnets. By fitting only one parameter, the shear stiffness between the spheres and the magnets, we obtained a very good agreement between experimental results and the predicted allowed and forbidden bands of propagation. We were also able to experimentally observe a ZGV point at finite wavelength. Disagreement between the shear stiffness predicted by the Hertzian theory for a single contact and the experimentally obtained one is attributed to the rough surface of the magnet, which was characterized using AFM techniques. The use of properly designed magnetic fields and particular surface topographies can lead to a programmable control of the stiffnesses between the elements of the setup and thus to an engineered dispersion relation. In addition, one can also modify the contact stiffnesses by placing dielectric spaces between the magnets and the spheres. This will increase the distance between the magnets and the spheres, resulting in weaker contact forces between the spheres and the dielectric spacer.

2.4 Experimental and numerical dispersion curves

The objective of this section is to present the method to derive the numerical and experimental dispersion curves of a free standing granular chain. The previous analytical results describe the derivation of dispersion curves for the case of infinite granular chain. The difference here stems from the addition of boundary conditions taking into account the finite size of the system. In order to obtain dispersion curves, displacements of each particle of the chain have to be estimated during a pulse propagation. Thus, a new experimental configuration is built and numerical simulation are performed involving, linear on-site dissipation, the driver excitation characteristic and boundary conditions. Numerical results will be compared to experimental one leading to the estimation of the precompressional force F_0 between particles together with the dissipative term. Simulations are achieved using a fourth order *Runge Kutta* numerical scheme.

Before running simulations for the entire chain, the experimental driver has to be characterized. The experimental driver is composed of a piezo-electric transducer with a bead glued on it to ensure the contact between the driver and the chain is the same than inside the chain. The next section is devoted to the characterization of this bead/transducer contact.

2.4.1 Characterization of the experimental driver

The driving bead and the transducer are glued together in order to ensure a high coupling. As a first approach for longitudinal motion, this system can be model as a linear mass-spring system (with dissipation) presented in Fig. 2.17. In order to estimate the stiffness K_g and the dissipative coefficient τ_g of this

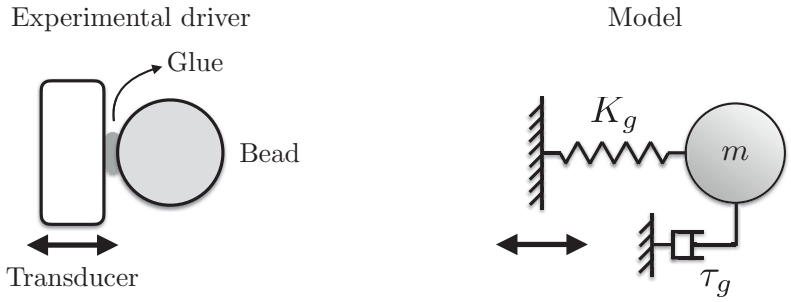

Figure 2.17: Schematics of the experimental driver (left) and mass-spring modelization of the driver (right) for longitudinal motion.

setup, we measure by laser vibrometer the response on the bead and on the transducer when a single pulse is sent, see Fig. 2.18(a). We will use the signal measured on the transducer as an initial condition for the driven wall in numerical simulation. Numerically, adjusting the stiffness and the dissipative parameters, the signal measured experimentally on the bead should correspond to the numerical results . The equation of motion solved numerically is:

$$m\ddot{u_1} = K_g\left(u_{act} - u_1\right) - m\dot{u}_1/\tau_g, \tag{2.39}$$

where u_{act} corresponds to displacement of the actuator and u_1 is the displacement of the particle. Numerically, u_{act} is imposed and takes values of the experimental signal measured on the transducer (blue line in Fig. 2.18(a)). The experimental and numerical results using $K_g = 1.49 \cdot 10^8$ N/m, $\tau_g = 0.17$ ms are presented in the Fig. 2.18(b).

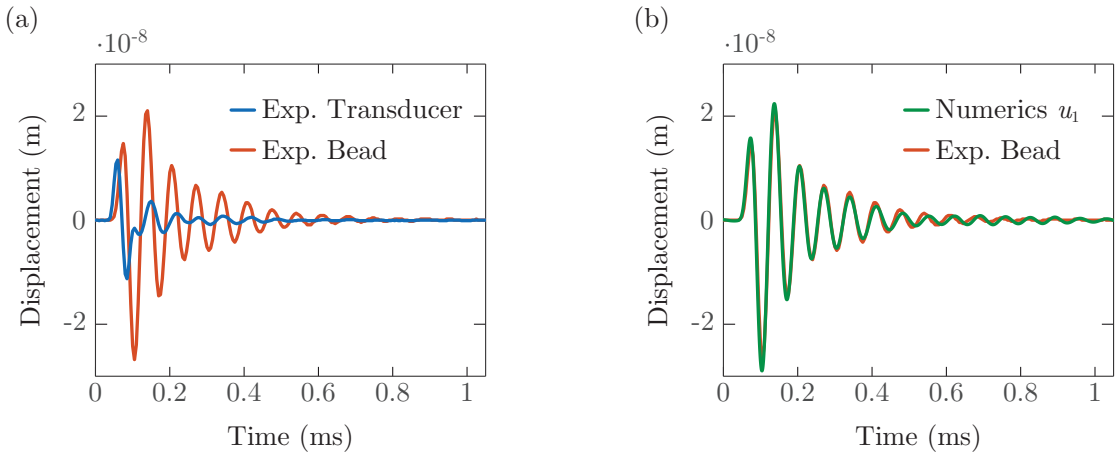

Figure 2.18: (a) Experimental signal measured on the transducer (blue) and on the bead (red) for a pulse excitation. (b) Numerical displacement (green) solving Eq.(2.39) with $K_g = 1.49 \cdot 10^8$ N/m, $\tau_g = 0.17$ ms and experimental signal measured on the bead (red).

From Fig. 2.18(b), we observe a very good agreement, after adjusting the stiffness and the dissipation term, between numerics and experiments. The simple model considering a driven wall and a mass linked by a linear stiffness is found appropriate. Exactly the same method is applied to characterized the shear contact between the transducer and the glued bead. The difference now is that the experimental shear transducer has in plane displacement (and also a small component of longitudinal motion). The laser vibrometer used for measurement is sensitive to out-of-plane motion only along the optical beam. Measuring with two opposite angles θ and applying simple trigonometric relations we can write the relation between the longitudinal (v_x) and the transverse (v_y) components of the velocity as follow:

$$v(\theta) = v_x \cos(\theta) + v_y \sin(\theta), \tag{2.40a}$$

$$v(-\theta) = v_x \cos(\theta) - v_y \sin(\theta). \tag{2.40b}$$

Fig. 2.19 depicts the setup measurement. Then, adding (or substituting) Eq. 2.40 permits to obtain the longitudinal and transverse components of the velocity as

$$v_x = \frac{v(\theta) + v(-\theta)}{2\cos(\theta)}, \tag{2.41a}$$

$$v_y = \frac{v(\theta) - v(-\theta)}{2\sin(\theta)}. \tag{2.41b}$$

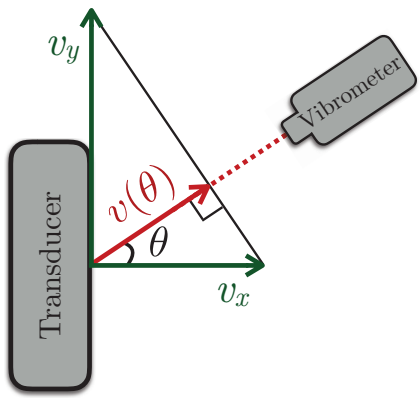

Figure 2.19: Schematics of the setup for the longitudinal and transverse components of the velocity.

Finally, the contact of the bead with the transducer for our configuration is well fitted in shear motion for $K_g' = 1.75 \cdot 10^8$ N/m and for the dissipative term $\tau_g' = 0.1$ ms. It is worth mentioning that when boundary conditions are taken into account for transversal-rotational modes, with shear rigidity between particles K_S, there is existence of a localized mode. It has been analytically demonstrated in Ref. [62] that the modification of the boundary condition will influence the position of this localized mode either in the gap between the two propagating branches (when $K_g' = K_S$) or above the higher propagative branch (when $K_g' > K_S$). In our case the shear rigidity estimated for the glue K_g' is two order of magnitude higher than the shear rigidity K_S inside the chain, hence a localized mode is present at very high frequency (far from the studied frequency). Consequently, in the present study, we will not focus on this localized mode. For the next simulations, we will include this first interaction between the transducer and the glued bead in order to fully describe the experimental setup. Let us turn now on the modeling of the linear granular chain with specific boundary conditions.

2.4.2 Modeling of the finite linear granular chain

The experimental setup has a finite size, thus boundary conditions have to be included in the numerical analysis. The attenuation of the wave during the propagation has to be considered, therefore a linear viscous on-site dissipation is added to the modeling considering a time of decay τ for the wave. This kind of dissipation is chosen because it is easy to implement it. Equations of motion for the modes sagittally polarized (u_x, u_y, ϕ_z) are explicitly given, for the first "1" and last particle "N" of the chain including boundary conditions and for all the particle "i" in between, as follow for the pure longitudinal branch $L(u_x)$:

$$\begin{aligned} m\ddot{u}_{1,x} &= -{K_N}^1 u_{1,x} - {K_N}^2(u_{1,x} - u_{2,x}) - \frac{m}{\tau_1}\dot{u}_1, \\ m\ddot{u}_{i,x} &= {K_N}^i(u_{i-1,x} - u_{i,x}) - {K_N}^{i+1}(u_{i,x} - u_{i+1,x}) - \frac{m}{\tau_i}\dot{u}_i, \\ m\ddot{u}_{N,x} &= {K_N}^N(u_{N-1,x} - u_{N,x}) - \frac{m}{\tau_N}\dot{u}_N, \end{aligned} \tag{2.42}$$

and for the coupled transverse-rotational branches $TR(u_y, \phi_z)$,

$$\begin{aligned} m\ddot{u}_{1,y} &= -{K_S}^1 u_{1,y} - {K_S}^2(u_{1,y} - u_{2,y}) + {K_S}^1 R\phi_{1,z} - {K_S}^2 R(\phi_{2,z} + \phi_{1,z}) - \frac{m}{\tau_1'}\dot{u}_1, \\ I\ddot{\phi}_{1,z} &= {K_S}^1 R u_{1,y} + {K_S}^2 R(u_{2,y} - u_{1,y}) - {K_S}^1 R(R\phi_{1,z}) - {K_S}^2 R(R\phi_{1,z} + R\phi_{2,z}), \\ m\ddot{u}_{i,y} &= {K_S}^i(u_{i-1,y} - u_{i,y}) - {K_S}^{i+1}(u_{i,y} - u_{i+1,y}) + {K_S}^i R(\phi_{i,z} + \phi_{i-1,z}) \\ &\quad -{K_S}^{i+1} R(\phi_{i+1,z} + \phi_{i,z}) - \frac{m}{\tau_i'}\dot{u}_i, \\ I\ddot{\phi}_{i,z} &= {K_S}^i R(u_{i,y} - u_{i-1,y}) + {K_S}^{i+1} R(u_{i+1,y} - u_{i,y}) - {K_S}^i R(R\phi_{i,z} + R\phi_{i-1,z}) \\ &\quad -{K_S}^{i+1} R(R\phi_{i,z} + R\phi_{i+1,z}), \\ m\ddot{u}_{N,y} &= {K_S}^N(u_{N-1,y} - u_{N,y}) + {K_S}^N R(\phi_{N,z} + \phi_{N-1,z}) - \frac{m}{\tau_N'}\dot{u}_N, \\ I\ddot{\phi}_{N,z} &= {K_S}^N R(u_{N,y} - u_{N-1,y}) - {K_S}^N R(R\phi_{N,z} + R\phi_{N-1,z}). \end{aligned} \tag{2.43}$$

Boundary conditions are "rigid" for one extremity leading to $u_{0,x} = u_{0,y} = \phi_{0,z} = 0$ and free for the other: $u_{N+1,x} = u_{N,x}$, $u_{N+1,y} = u_{N,y}$, $\phi_{N+1,z} = -\phi_{N,z}$. ${K_N}^i$ and ${K_S}^i$ are the normal and shear rigidities between particle i-1 and i, respectively. These rigidities depend on the material characteristics and the precompression force F_0 applied to the chain. This formulation allows to introduce different contact rigidities between all particles. Finally, for the longitudinal branch, ${K_N}^1$ corresponds to the first contact between the transducer and the glue bead defined in the previous section, thus ${K_N}^1 = K_g = 1.49{\cdot}10^8$ N/m and $\tau_1 = \tau_g = 0.17$ ms. Similarly in the transverse-rotational branches, ${K_S}^1 = K'_g = 1.75 \cdot 10^8$ N/m and $\tau_1 = \tau'_g = 0.1$ ms. The particle "1" will be considered as the driver for the chain. It should be noticed that for simplicity we consider losses only to the transverse part and not directly into the rotational one.

Fixing the material of the particle (here stainless steel beads : $R = 7.94$ mm, $E = 200$ GPa, $\nu = 0.3$), the only two parameters which have to be defined are the precompression force F_0 and the dissipation coefficient τ. The precompression force can be experimentally estimated by measuring the pulling force required to separate two adjacent particles when using a dynamometer, but the dissipation coefficient has to be fitted comparing experiment and numerical simulation. In order to access to these parameters, a pulse signal (short excitation in time) is employed. Indeed the finite length of the signal is useful because we can clearly observe the time of flight of the pulse from the driver to the other extremity of the chain and the reflections from the boundaries of the chain. In linear regime, the time of flight of the pulse propagation is governed by the precompressional force F_0. An increase of F_0 will reduce the time of flight of the wave. Thus looking for the amplitude of the pulse along the chain we can observe the attenuation of the wave. As we will see later, this attenuation term can be different between the longitudinal and the transverse branch. Numerically, the fourth order *Runge Kutta* method is implemented to solve Eqs. (2.42 - 2.43).

2.4.3 Experimental dispersion curve method and setup configuration

In order to derive the experimental dispersion curve of a free standing granular chain, i.e. without interaction with a substrate, the experimental setup is identical to the one in section 2.3.1. The stainless steel beads of 15.875 mm diameter are placed onto a rubber substrate, see Fig. 2.20. Permanent magnets are inside the rubber substrate, thus the magnetic field created by the magnets induces forces between particles. The use of soft rubber substrate allows neglecting the interaction between beads and substrate. To obtain the dispersion curve, measurements on each particle of the chain has to be realized. For the pulse signal which excites the chain, a compromise between the frequency bandwidth and the repartition of energy has to be taken into account to excite all modes of the chain. Finally the chosen signal is a "haversine" which is analytically described as one period of $\sin^2(\theta/2)$ and can be produced with a function generator. This experimental signal is a single sine wave with an offset voltage to obtain a zero amplitude at the starting and ending point as presented in the Fig. 2.21(a) in the temporal domain. From previous results, propagative bands

Figure 2.20: Photography of the 38 beads chain on top of the rubber substrate, with permanent magnets inside it.

are present up to 12 kHz so the excitation signal has to be sufficiently broadband to cover a frequency range up to this cutoff frequency. Thus the frequency of the "haversine" cycle is chosen at 20 kHz and we can see on Fig. 2.21(b) that a sufficient frequency bandwidth is reached which will permit to excite all modes of the chain by this signal.

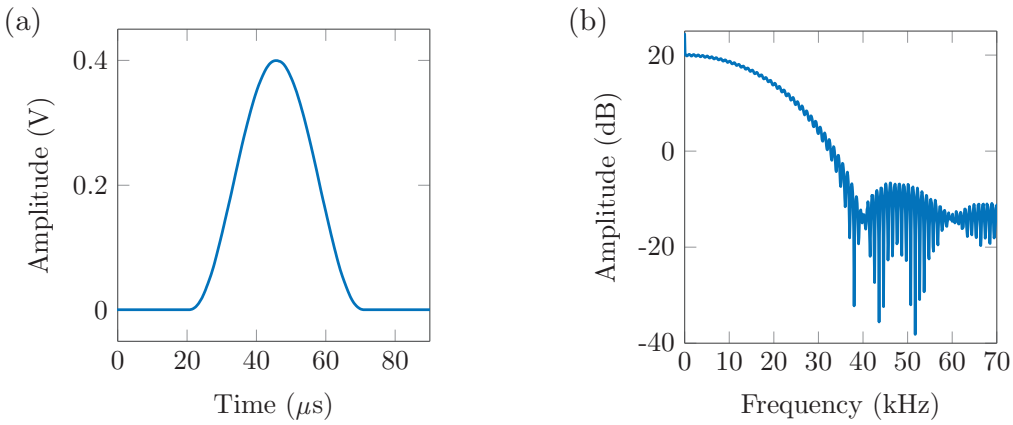

Figure 2.21: One period of the "haversine" electric signal excitation used to derive experimentally the dispersion curves, (a) temporal and (b) frequency domains.

Experimentally, the signal is repeated each second and 100 averages are performed on each particle in order to get rid of the noise and perturbations during measurements. Then the same experimental configurations than in the section 2.3.1 are explored, i.e. exciting the chain in 3 independent directions (x, y, z) and measuring in the same direction than the excitation, see Fig. 2.8. The difference is that now we scan every particles of the chain. With the aim of scanning each particle, the laser vibrometer is deported on the side of the chain with a given angle φ and we project the velocity obtained along the x-axis by the basic trigonometric formula $v_x = v(\varphi)/\cos(\varphi)$. The laser vibrometer is attached to a programable displacement stage *Newport*. The schematics of the experimental measurement is shown on Fig. 2.22.

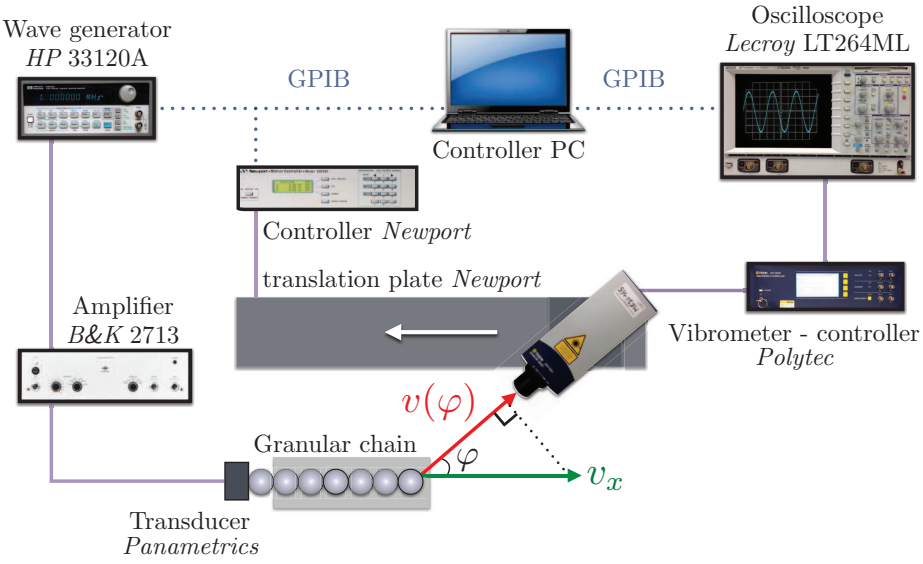

Figure 2.22: Diagram of the instrumentation used for the experimental dispersion curve measurement.

The displacement of each particle is recorded as a function of time. The post-processing is done by applying a two dimensional (space-time) Fourier transformation (FT) which leads directly to the experimental dispersion curves. The two dimensional FT permits to pass from temporal domain to wave number domain, thus we can rebuild the wave number axis to display the experimental dispersion curve. The resolution of this type of representation is limited by the number of measured points. Increasing the number of particles and thus the number of measurement points leads to a better resolution. The number of particles in the chain is extended to 38 beads. Because of practical issues, a new rubber substrate is constructed responsible of a small difference on the distance between bead and magnet compared to the previous setup (around 1.5 mm in this case). As a results the attractive force between particles is affected and experimentally estimated by dynamometer to be $F_0 = 1.5 \pm 0.15$ N.

2.4.4 Results and discussion

This section is devoted to the comparison between experimental and numerical dispersion curves for a "free" granular chain. The numerical simulation allows to better estimate the precompressional force F_0 and to estimate the attenuation term τ. Analytically the complete dispersion curves have been already presented in section 2.2.3 and are introduced in Fig. 2.23 as a reminder. In the sagittal plane, a purely longitudinal branch $L(u_x)$ and two transverse-rotational branches $TR_{1,2}(u_y, \phi_z)$ are present. For modes polarized in the horizontal plane, a pure rotational branch $R(\phi_x)$ and two transverse-rotational branches $TR_{1,2}(u_z, \phi_y)$ are present. The TR branches are identical between both planes because of the symmetry of the model. Numerically, we solve the Eqs.(2.42) for the pure longitudinal branch and Eqs.(2.43) for the transverse-rotational branch by a Runge Kutta method including the driver presented in previous section 2.4.1 and considering a free boundary for the other extremity. The experimental signal recorded on the glued bead is used as a driver in order to compare exactly the same setup between experiments and numerical simulations. The precompressional force and the dissipative term are fitted based on the time of flight and the amplitude of the experimental pulse propagation, respectively.

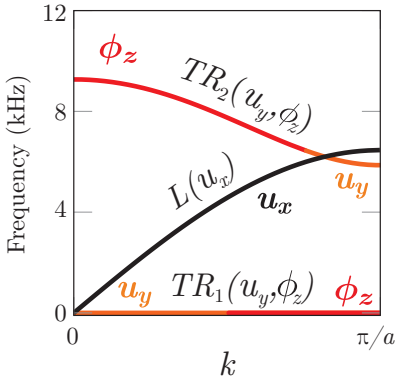

Figure 2.23: Dispersion curves for the infinite free granular chain for modes polarized in the sagittal plane considering a precompressional force $F_0 = 1$ N.

Fig. 2.24 presents experimental and numerical results for the longitudinal wave propagation and dispersion curves $L(u_x)$. The numerical simulations are performed using $F_0 = 1.8$ N and $\tau = 2.4$ ms. It should be noticed that in Fig. 2.24, the displacement of the glued bead is not represented.

From the temporal results presented in Fig. 2.24(a-b), we can observe a good agreement between both experimental and numerical results. The fitted parameter for the precompressional force F_0 is on the same order than the one experimentally estimated by the dynamometer ($F_0 = 1.5 \pm 0.15$ N). The value obtained for the dissipative term is on the same order than in [22] using the same bead material. However, from the experimental results we can see on the main pulse propagation a small feature of the displacement signal

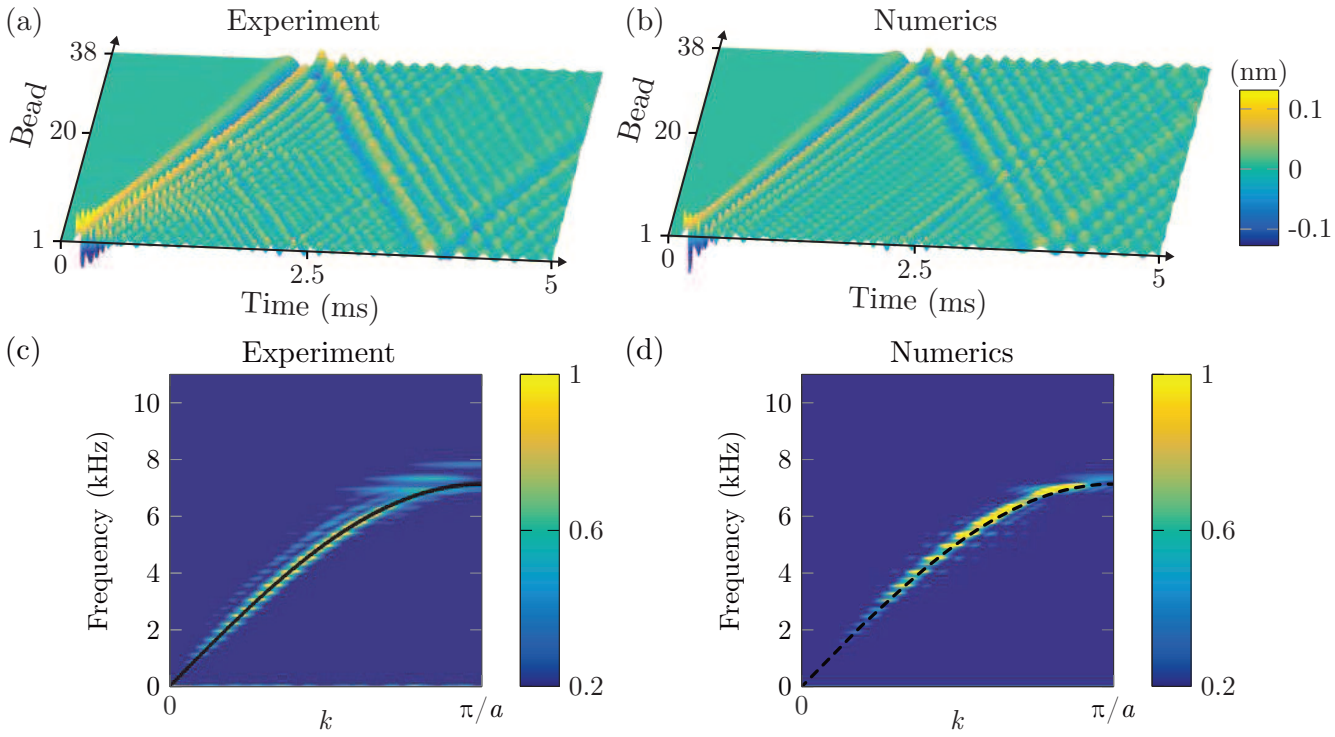

Figure 2.24: (a) Experimental and (b) numerical (from Eq. (2.42)) results for the longitudinal wave propagation as function of time for a chain of 38 beads. (c) Experimental and (d) numerical dispersion curves with $F_0 = 1.8$ N and $\tau = 2.4$ ms. Analytical dispersion curves are superimposed.

at the particle 20 which is not present by the numerical results. A scattered wave is also present from this site. This perturbation is probably due to the presence of a defect in the chain due to a modification of precompression force and/or misalignment of the particle 20. Numerical simulations adding defects in the precompression at the contacts are presented later on Fig. 2.28. On panel Fig. 2.24(c-d), the experimental and numerical dispersion curves are presented. Theoretical dispersion curves for an infinite chain are also superimposed adjusting the precompression force to $F_0 = 1.8$ N. Theoretical curves depict the existence of translational motion for u_x component in a color scale (as in the Fig. 2.5). On the panel Fig. 2.24(c), a grey scale from white (absence) to black (pure existence) of u_x component is represented. As predicted in the previous section, this branch is purely longitudinal $L(u_x)$, so the curve is totally black. We fully measure the predicted pure longitudinal branch. It should be noted that at very low frequency, the displacement amplitude decreases experimentally and numerically. This comes from the experimental transducer which is not efficient at theses low frequencies.

Let us now examine the propagation of coupled transverse/rotational wave, by driving vertically along the y-axis and measuring in the same direction. Numerically, we solve the set of Eqs. (2.43), only the transverse part is represented. The results are shown in the Fig. 2.25. In order to fit the experimental results in TR propagation, the precompression in now $F_0 = 1.23$ N, which is significantly different than in the L propagation where $F_0 = 1.8$ N. It should be noticed that the experiments for the TR wave propagation have been done a different day than the L propagation. After each series of experiment, beads are take off from the setup, therefore when replacing beads for a new series of measurement there

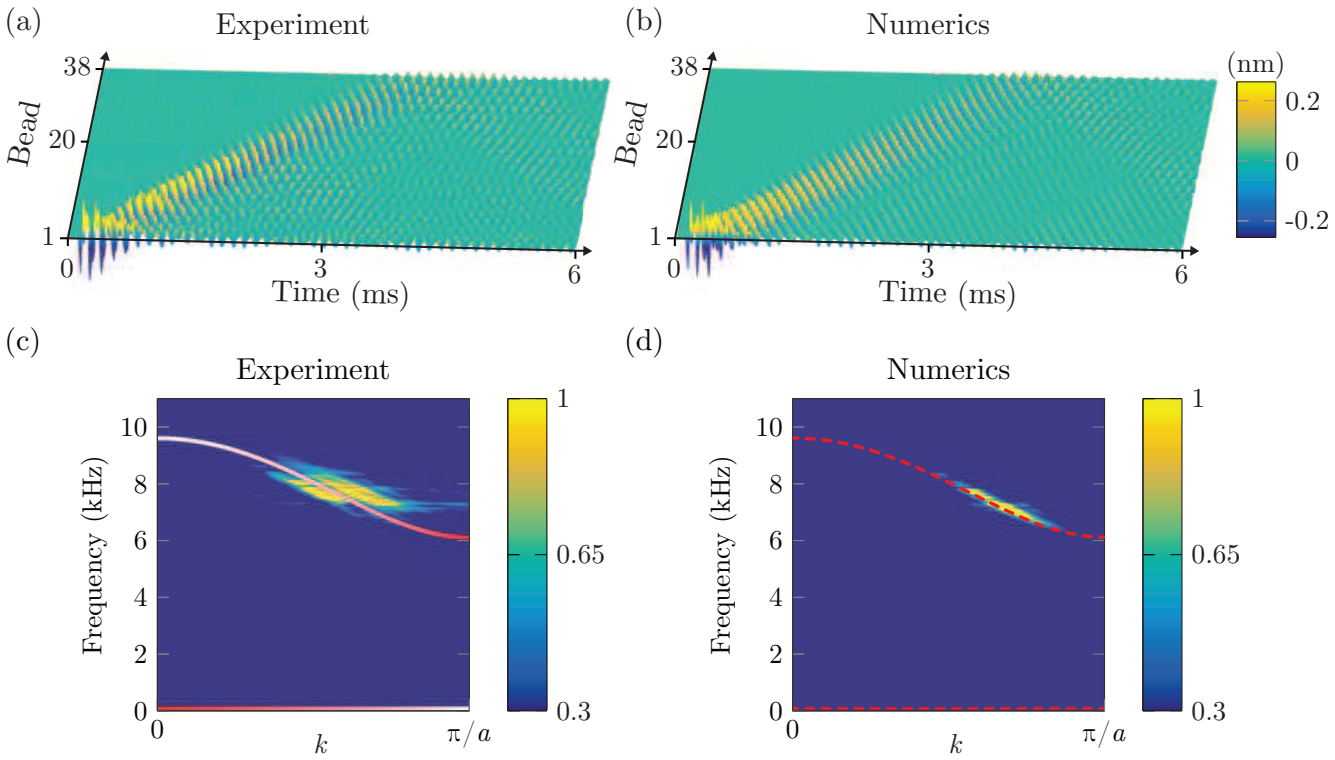

Figure 2.25: (a) Experimental and (b) numerical (from Eq. (2.43)) results for the transverse wave propagation as function of time for a chain of 38 beads. (c) Experimental and (d) numerical dispersion curves with $F_0 = 1.23$ N and $\tau' = 0.8$ ms. Analytical dispersion curves are superimposed.

are not exactly at the same positions, same alignment which could lead to difference in precompression. This first result shows that our setup is sensitive to the arrangement of the particles.

Looking to the temporal traces of the TR pulse propagation, Fig. 2.25(a-b) we observe a large difference on the propagation in comparison with the L branch. First, the time of flight is larger in TR meaning that the wave velocity is smaller. Second, in order to fit the experimental results, the dissipation has to be also larger in the TR propagation. This increase of losses can be expected because the loss mechanism is different, e.g. friction between particles. The vertical direction of excitation (u_y) leads also possibly to more interaction between beads and the soft rubber substrate which could explain the larger lossy term. From temporal signal point of view, we also observe some oscillations in the signal after the main pulse which indicates small reflections in the signal along the chain. Finally, the spacio-temporal pattern of the wave propagation in TR branch is different due to opposite sign between the group and phase velocity.

Regarding the experimental dispersion curve, Fig. 2.25(c), the theoretical existence of u_y component is superimposed in color scale from white (absence) to red (pure existence). Two coupled transverse/rotational $TR(u_y, \phi_z)$ branches are expected from theory. The TR branch at zero frequency is not measured for both experimental and numerical methods because the experimental transducer can not transmit enough energy at this frequency. Looking to the higher TR branch, the upper part becomes more and more dominated by rotational motion. Indeed, experimentally and numerically the upper part of

the branch has a very weak amplitude in contrast with the lower part. The numerical component of the rotational part is shown on the Fig. 2.26 and we can clearly observe the upper part of the TR branch. It should be noted that close to $k = \pi/a$ experimental and numerical results fail to describe the theoretical branch.

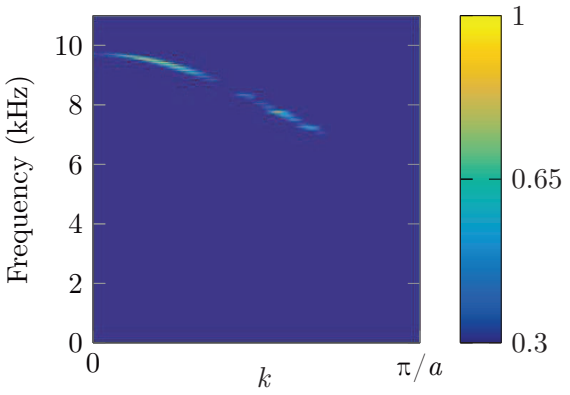

Figure 2.26: Numerical dispersion curve of the rotational component with $F_0 = 1.23$ N and $\tau' = 0.8$ ms.

The first hypothesis to explain this disagreement is that at high frequency the corresponding propagating wavelengths are on the order of the lattice period. Hence, experimentally a small amount of disorder induced by bead misalignments could lead to the loss of the relevant modes. However, the numerical simulation which does not take into account misalignment fails also close to $k = \pi/a$. The second explanation to the missing part of the dispersion curve may arise from the very small values of the group velocity close to $k = \pi/a$. It has been demonstrated in [123, 124] that for small group velocity an enhanced damping appears from the interplay of losses and slow sound propagation. Looking to the rotational component, Fig. 2.26, the group velocity is also small close to $k = 0$ however the branch is better described. This stems from the simulation which does not consider direct dissipation for the rotational component.

Let us look again on the experimental TR dispersion curve, Fig. 2.25(c), the measured path is thicker than the numerical results. Experimentally 100 averages are performed on each particle. For each measurement, a rearrangement of the particles could exist leading to a modification of the effective precompression into the chain. In order to verified this assumption, numerical simulations are computed 100 times considering a constant precompression F_0 along the chain but varying this force at each simulation. Finally, 100 simulations are performed using 100 random values of F_0 into the interval of $F_0 \pm 0.3$ N. After simulations, the mean value the precompression is equal to F_0 and the numerical results of the dispersion curve for the longitudinal and transversal-rotational branches are presented in the Fig. 2.27.

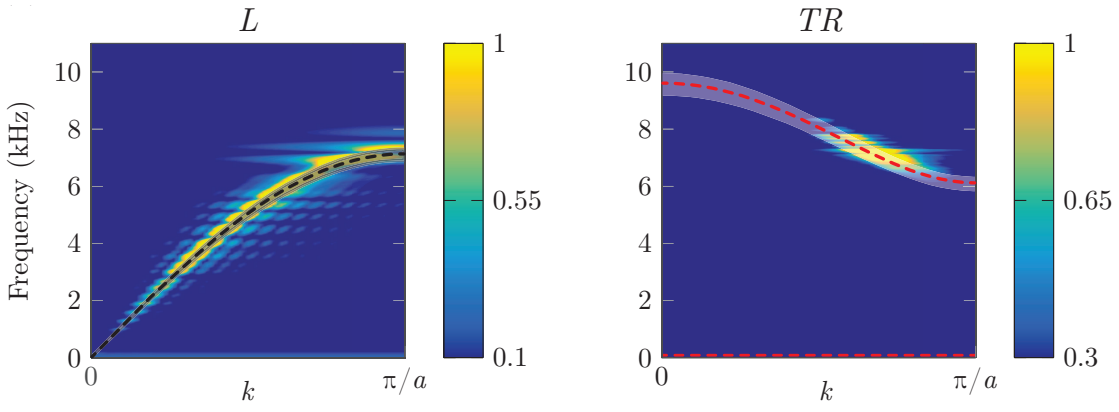

Figure 2.27: Numerical dispersion curves for the longitudinal branch (left) and (right) for the transverse-rotational branches after 100 simulations varying the precompressional force $F_0 \pm 0.3$ N. The analytical dispersion curves are superimposed considering F_0 (dashed lines) $\pm$ 0.3 N (shadow zones).

From Fig. 2.27, we can observe that the TR dispersion curve are thicker than before which is in accordance with experimental and analytical results. For the L dispersion curve, it appears some broad lines at high frequency which are also present in the experimental results.

We can now examine the effect due to disorder in the precompressional force. Indeed, experimentally on temporal domain we have observed some reflected and scattered waves during the propagation. For the longitudinal propagation, a feature on the displacement at the particle 20 is clearly present with scattered waves. We can numerically mimic this effect by decreasing the precompression force at the contact between the particle 19 and 20. The numerical result is presented in Fig. 2.28(a). Physically, the decrease of the attractive force could be due to a modification of the magnetic field and/or misalignment. To go further, simulations with disorder in precompression at each contact are shown on Fig. 2.28(b-c) for the L and TR propagation. The forces are created by random values into a certain interval around F_0. The mean value of the precompressional forces are very close to F_0. For the L simulation the precompression are $F = F_0 \pm 0.9$ N with $F_0 = 1.8$ N, and for the TR one $F = F_0 \pm 0.5$ N with $F_0 = 1.23$ N. Dissipative terms τ are the same than the previous fitted parameters for each branch.

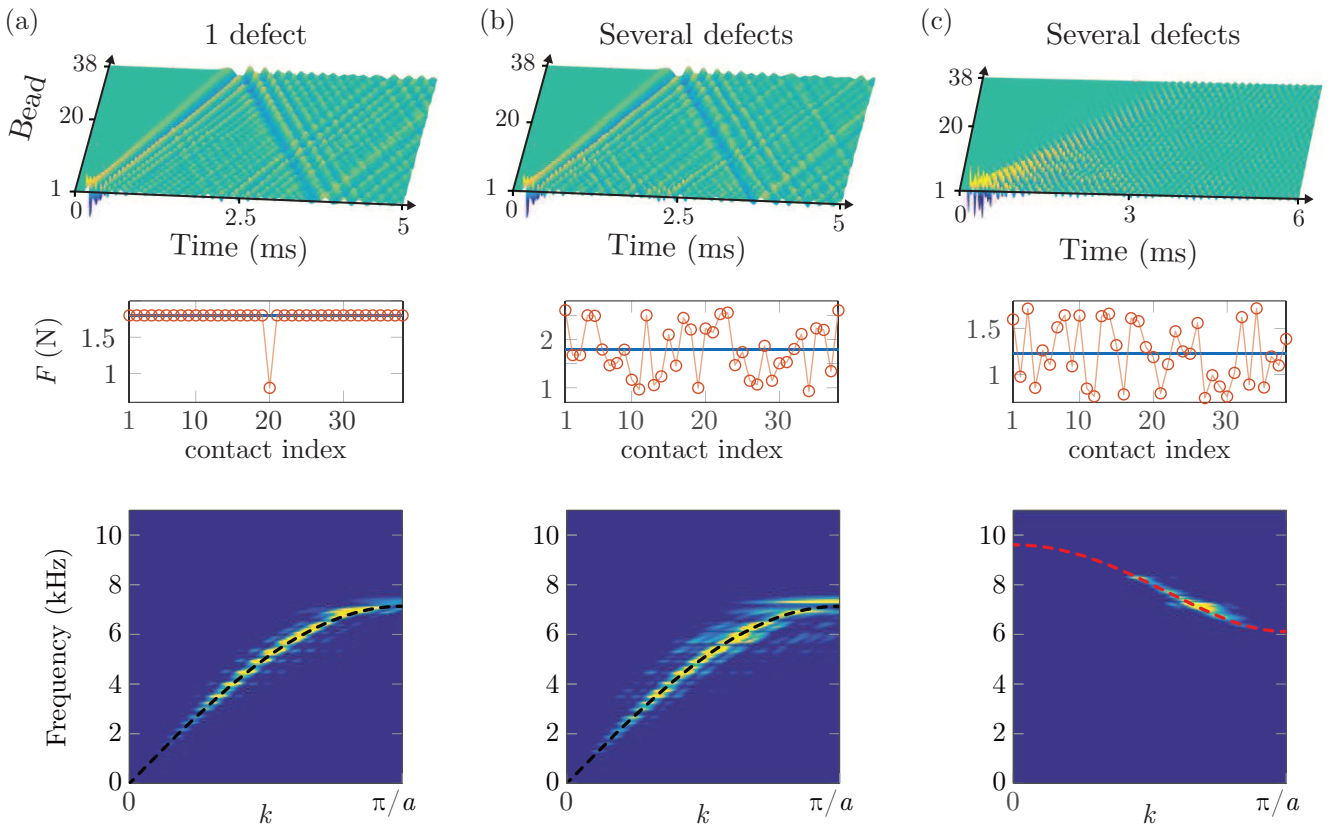

Figure 2.28: Numerical results for (a) the L branch with $F_0 = 1.8$ N and $\tau = 2.4$ ms, defect at bead 20 with $F_0 = 0.8$ N (b) with several defects $F = 1.8 \pm 0.9$ N and $\tau = 2.4$ ms (c) TR branch with $F = 1.23 \pm 0.5$ N and $\tau' = 0.8$ ms. The blue line corresponds to the mean value of F_0. The dashed lines correspond to the analytical dispersion curve using a constant F_0.

From the result with only one defect, Fig. 2.28(a), on the spacio-temporal plot a reflected wave is present starting from the defect site. A straight line appears along the time around the defect particle

site, meaning that some waves are localized. This pattern is closer to experimental results. The dispersion curve is not affected by this single defect. When the precompression is randomly created at each contact, panel (b), we observe several reflected waves forming from sites with a large difference in precompression. Furthermore, the dispersion curve seems to be more spread than before. For the case of several defect in the TR branch, panel (c), reflected waves are also present but due to the pattern of the wave propagation it is difficult to determine at which site the wave is reflected. The dispersion curve is basically the same as before but with smaller amplitude. The decrease in amplitude could be expected because a part of the wave is reflected at several sites and finally there is less energy reaching the end of the chain. Finally, this numerical study shows the robustness of the dispersion curve visualization when large defect in precompression are taken into account.

To complete the set of experimental results, the full dispersion curve can be presented for the modes polarized in sagittal and horizontal planes, in Fig. 2.29. The sagittal plane is composed of displacements along x and y-axes and a rotation around z-axis, which corresponds to the former results presented in Figs. 2.24(c) and 2.25(c). Thus, the two results are represented on the same panel (a) of Fig. 2.29. The horizontal plane is composed of a displacement along z-axis and two rotations around x and y-axes. Exciting and measuring along the z-axis allows to describe the upper TR branch. The measurement has been made the same day than for the longitudinal branch, thus fitting the precompression with the time of flight, we obtain the same value of $F_0 = 1.8$ N. The result is shown in Fig. 2.29(b) where the theoretical existence of the translational motion u_z is labeled by magenta color. Between both planes, the higher TR branches have the same behavior: the upper part of these branches are not measured (mostly rotational motion) as well as when $k = \pi/a$ is approached. The pure rotational branch $R(\phi_x)$, existing at very low frequency in the horizontal plane, is not excited and also cannot be detected by the laser vibrometer so we do not expect to measure it, as well as the zero frequency branch.

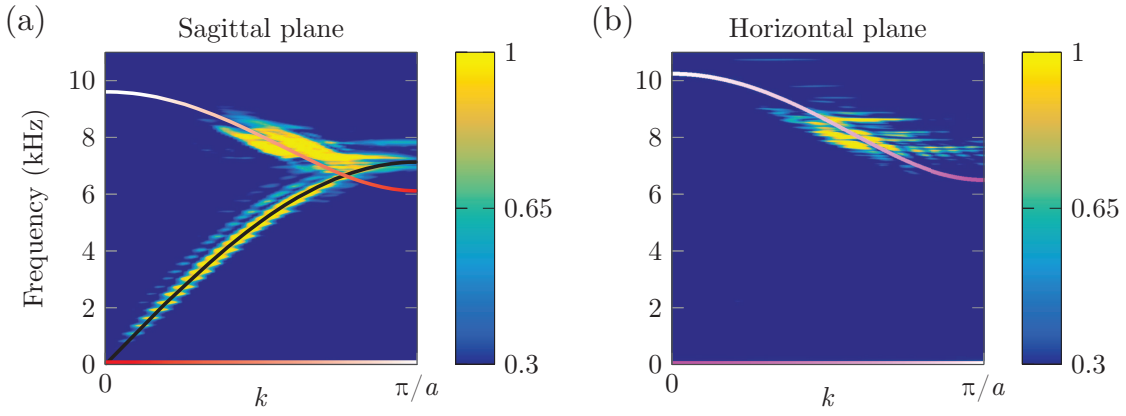

Figure 2.29: Experimental dispersion curves for a chain of 38 beads for modes polarized in (a) sagittal plane and (b) horizontal plane. The theoretical existence of translational motion is superimposed on each panel in color scale (black, red and magenta for u_x, u_y, u_z components, respectively). Theoretical dispersion curves are plotted with $F_0 = 1.8$ N for $L(u_x)$ and $TR(u_z, \phi_y)$ (same day of experiments) and $F_0 = 1.23$ N for $TR(u_y, \phi_z)$.

A method presented in Ref. [125] provides the recovery of complex wavenumber information from spacio-temporal experimental measurement. The method, called SLaTCoW for Spatial LAplace Transform for COmplex Wavenumber recovery, is based so on spacial Laplace transform instead of the usual spacial Fourier transform. The Laplace transform provides information on both real and imaginary parts of the poles by minimizing a correctly chosen cost function. It enables the reconstruction of complex wavenumber (k_r, k_i), as well as the complex amplitudes, of the modes. We applied the SLaTCoW method to our experimental measurement for longitudinal wave propagation, the results are presented in Fig. 2.30.

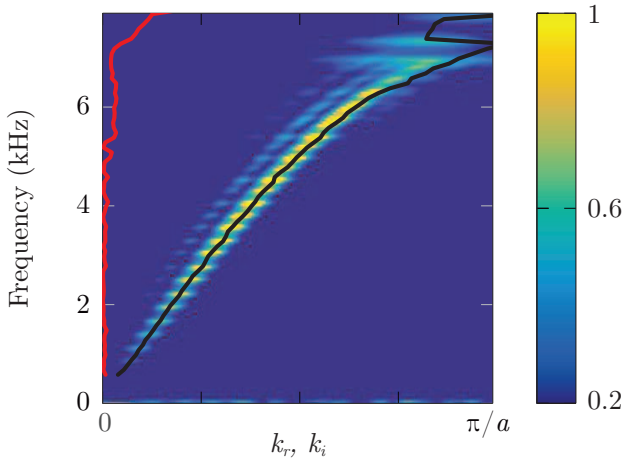

Figure 2.30: Experimental dispersion curve for longitudinal excitation in a chain of 38 beads. The colormap corresponds to the experimental dispersion curve from the two dimensional Fourier transform (already presented in Fig. 2.24(c)). Real (black) and imaginary (red) parts of the wavenumber, estimated by SLaTCoW method [125], are superimposed.

From the Fig. 2.30, we can observe that the real part of the wavenumber is in very good agreement with the results from the spacial FT. The imaginary part of the wave number is small and constant up to 5.5 kHz and then is three times larger up to the cutoff frequency of the chain. In the gap, we see a clear increase of the imaginary part. Finally, this method could be used as an indicator of the loss present in experimental system.

The preliminary experimental results for the dispersion curves of a linear granular chain coupled with a subraste are presented in appendix B.

2.4.5 Summary

The experimental dispersion curves are successfully measured for the case of a linear granular chain without interaction with a substrate. Numerical results including boundary conditions and driver characteristics are in very good agreement for each branch. Via the study of the spacio-temporal wave propagation, numerical results allow to better estimate the precompressional force and the attenuation of the wave along propagation. We observe different values for the linear dissipation between L and TR propagation. The dissipation is higher for the TR modes which is expected because the beads are interacting more

with the soft rubber substrate, with shear excitation, than for L mode one. These numerical simulations also explain why experimentally we are not able to detect the part close to $k = \pi/a$ for the TR branches which is due to enhanced damping from the interplay of losses and slow sound propagation (group velocity takes very small values). This study points out that the precompression in the experimental setup is also very sensitive to the initial position and alignment of the beads. In order to improved the comparison between experiment and numerical simulation, a model taking into account the bead misalignment could be developped.

2.5 Conclusion

This chapter has described the propagation of elastic waves in a magneto-granular phononic crystal consisting of a granular chain in direct contact or not with an array of fixed permanent magnets. Taking into account all degrees of freedom in translational and rotational motions, the full dispersion relation has been derived. Theoretical study have shown that our system supports transversal-rotational propagation modes, zero group velocity (ZGV) modes and accidental degeneracies in the dispersion curves.

Furthermore, experiments have clearly revealed the existence of coupled transversal-rotational branches in a granular chain that moreover can be tuned by the external magnetic field. In the configuration where the beads are in direct contact with the magnets, good agreement is found between experimental results and the predicted allowed and forbidden bands of propagation by fitting only one parameter: the shear stiffness between the spheres and the magnets. Experimental evidence of a ZGV point at finite wavelength has been shown. Disagreement between the shear stiffness predicted by the Hertzian theory of single contact and the experimentally obtained one is attributed to the rough surface of the magnet, which was characterized using AFM techniques. The use of properly designed magnetic fields and particular surface topographies can lead to a programmable control of the stiffnesses between the elements of the setup and thus to an engineered dispersion relation. In addition, one can also modify the contact stiffnesses by placing a dielectric spacer between the magnets and the spheres. This will increase the distance between the magnets and the spheres, resulting to weaker contact forces between the spheres and the dielectric spacer.

Finally, experimental dispersion curves have been obtained by measuring the velocity each particle of the chain and are successfully compared to numerical simulations including boundary conditions and the experimental driver characteristics. The numerical simulations have provided a better estimate the precompression force and the attenuation of the wave along the propagation. This study has pointed out that the precompression in the experimental setup is sensitive to the initial position and alignment of the beads. Numerical simulations taking into account bead misalignment could finally improve the comparison with experimental results.

The low static load F_0 values endows the system with a strong nonlinear response. The next chapter will first focus on the complete understanding of wave packet and continuous signal propagation in magneto-granular structures via the study of the linear dynamical response followed by the study of the nonlinear case.

Chapter 3

Linear and nonlinear wave propagation

Contents

3.1 Introduction 68
3.2 Linear propagation of packets and continuous harmonic waves 69
3.2.1 Longitudinal wave propagation: experiments vs numerics 69
3.2.2 Transverse-Rotational wave propagation: experiments vs numerics 73
3.2.3 Summary 79
3.3 Second harmonic generation in a finite granular chain 81
3.3.1 Numerical analysis 81
3.3.2 Experimental observation of the second harmonic generation 84
3.3.3 Frequency analysis in different dynamical regimes 87
3.3.4 Summary 89
3.4 Γ-shaped granular chain: mode conversion and harmonic filtering 91
3.4.1 Principle of conversion from longitudinal to coupled transverse-rotational modes . 92
3.4.2 Experimental Γ-shaped chain 93
3.4.3 Summary 98
3.5 Conclusion 99

3.1 Introduction

This chapter is focused on the complete description of the linear and nonlinear wave propagation through one-dimensional and Γ-shaped granular structures. In the first part, the granular chain is excited by wave packets and continuous harmonic waves in their linear dynamical regime. By direct comparison of spatio-temporal measurements and numerical simulations, we estimate the precompression force and the losses for different propagating wave polarization (i.e. longitudinal or transversal/rotational wave propagation). The latter are approximated as viscous on-site damping in the numerical simulations. The group velocity is also experimentally estimated as a function of the driven frequency for longitudinal and coupled transversal/rotational waves.

In the second part, the nonlinearities originating from the contact between particles are taken into account. In particular, we focus on the experimental excitation of harmonics and the observation of the spatial beating in amplitude of the second harmonic. Finally, the nonlinear propagation in a Γ-shaped granular structure is studied. Advanced wave control can be obtained by combining nonlinear effects and geometrically induced conversion from longitudinal to coupled transversal/rotational modes.

3.2 Linear propagation of packets and continuous harmonic waves

This section is devoted to the study of the linear propagation of wave packets (sinus modulated by a Gaussian function) and continuous harmonic waves in a free standing granular chain considering both longitudinal and transverse polarizations. The objective is to obtain from experiments a better understanding of the wave propagation in such a system. Experimentally, the setup configuration is identical to the one presented in section 2.3.1. Only the wave generator is replaced by a *Tektronix* AFG3022B. The stainless steel beads of 15.875 mm diameter are placed on a rubber substrate with permanent magnets inside it. Using a laser vibrometer, we measure the velocity of each particle during the wave propagation. Experimental results are compared with numerical simulations in order to estimate experimental values for the dissipation and the precompression force.

3.2.1 Longitudinal wave propagation: experiments vs numerics

First, we study the propagation of wave packets (sinus modulated by a Gaussian function) in the granular chain.

We choose a short duration signal (few periods of sinus) in order to clearly separate forward and backward waves during the propagation. The central frequency of the wave packets is modified from 1 kHz to 10 kHz and the measurement is averaged 30 times by particle. Fig. 3.1 represents an example of the velocity signal recorded on the transducer.

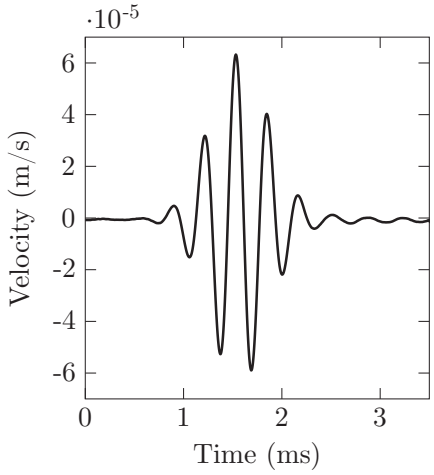

Figure 3.1: Velocity measured on the transducer for a sinus at 3kHz modulated by a Gaussian function (corresponding to a maximum of displacement 3.46 nm).

Numerically, we solve the Eq. (2.42) using the fourth order Runge Kutta method. One boundary is considered free while the other driven using the exact experimental signal as recorded by the laser vibrometer. An example of the numerical and experimental particle velocities as a function of the time is presented in Fig. 3.2 for a chain of 38 beads, using a wave packet with central frequency at 3 kHz, see Fig. 3.1. Wave propagation can be considered as near-linear when the amplitude of the driver excitation is very small in comparison with the static overlap, here $\delta/\delta_0 = 0.003$.

By fitting the precompression force to $F_0 = 2.25$ N and the dissipative term to $\tau = 1.9$ ms a good agreement is found between experiments, Fig. 3.2(a), and simulations, Fig. 3.2(b). We can clearly see the multiple reflections of the wave packet from the boundaries and the decrease of the wavepacket amplitude during the propagation caused by dispersion and dissipation. Wave packets can be isolated and numbered as presented in Fig. 3.2(a)(c). The wave packet ① corresponds to the initial wave packet while ③ and ⑤ correspond to reflected waves from the boundaries. In Fig. 3.2(c)(d), we also show the velocity of the first and the last particle of the chain as a function of time. Looking in more details at the experimental velocity signal of the first particle, one can observe some oscillations between 2.5 ms

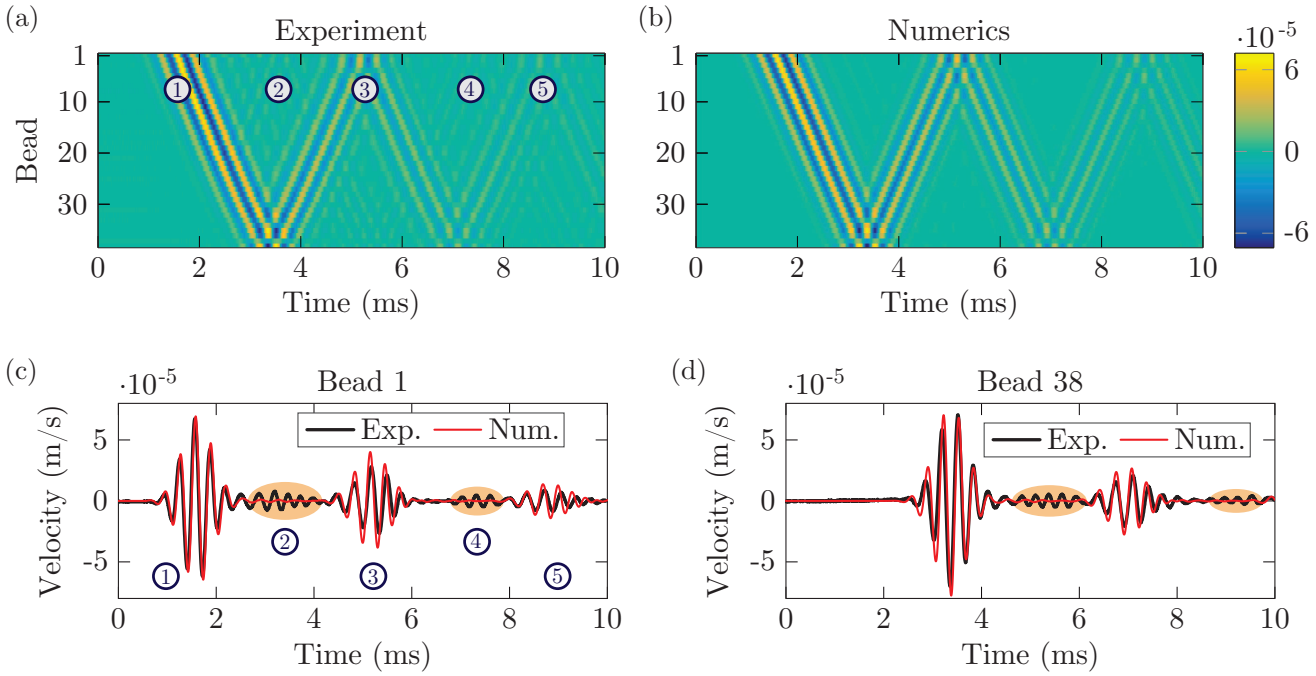

Figure 3.2: (a) Experimental spacio-temporal diagram of the velocity of the particles during the propagation of a wave packet with a central frequency of 3 kHz. (b) Numerical spacio-temporal diagram with $F_0 = 2.25$ N and $\tau = 1.9$ ms. Velocity as a function of time for (c) the first bead and (d) the last bead of the chain.

and 4 ms (wave packet ②), as well as between 7 ms and 8 ms (wave packet ④). The same kind of small oscillations are also presented in the experimental velocity signal of the last particle. These oscillations do not appear in the numerics in which a perfectly aligned chain has been considered. Thus, we believe that these oscillations represent reflected waves which come from misalignment of the central particles, see more details below.

Using the spatio-temporal experimental measurements, we can also obtain the dispersion relation. To do so, we apply the two-dimensional FFT for each wave packet propagation (central frequency from 1 to 7 kHz). We record the maxima (pairs of frequency-k) and we plot these in Fig. 3.3(a). Different colors correspond to initial wave packets with different central frequency. The analytical solution from Eq. (1.22) and a third order polynomial fit, given by the following expression

$$\omega(k) \quad = \quad -0.0059725 * k^3 + 0.79966 * k^2 + 304.24 * k + 1734.03, \tag{3.1}$$

are also superimposed. Experimentally, the dispersion curve is not totally reconstructed at the very low and high frequency ranges. For the low frequency range the reason is that the transducer that has been used is not powerful at this frequency range and thus the chain is weakly excited at these frequencies. For the high frequency range, close to the cutoff frequency, the obtained dispersion curve is not well reconstructed since there are no clear maxima in the two-dimensional FFT post processing analysis (similar results have been presented in Chapter 2). Furthermore, we observe that the fitted dispersion relation has a slight deviation from the analytical dispersion as k goes to zero. In particular, it seems that in experiments, a

small band gap exists up to $f \approx 275$ Hz. This deviation leads to strong different group velocity at low frequency. This small gap can be explained by considering a weak mechanical coupling, mostly governed by shear coupling, between the granular chain and the rubber substrate. By estimating the shear rigidity that causes this gap we find a rigidity three orders of magnitude smaller than the rigidity between particles. This observation confirm the fact that the coupling between the chain and rubber can be safely neglected for most of the frequency band.

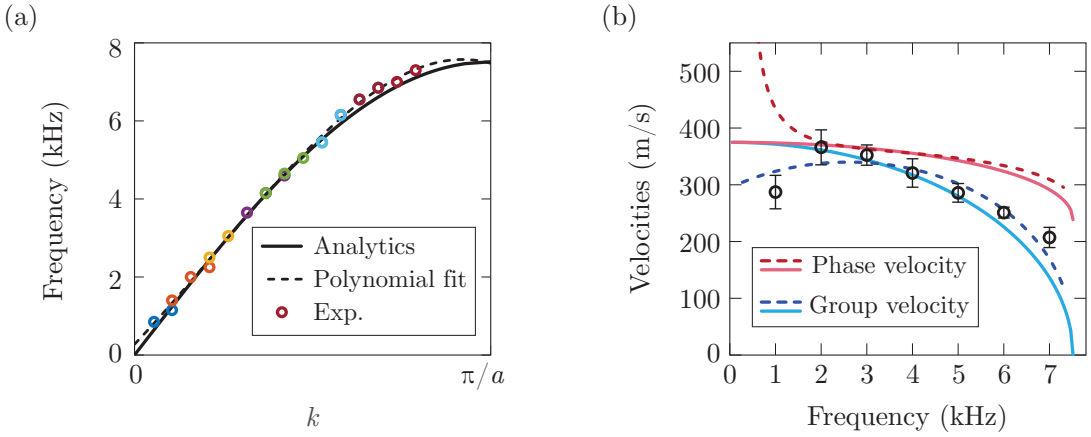

Figure 3.3: (a) Dispersion curve from experimental data (marker), analytics (solid line) and polynomial fit (dashed line). (b) Phase and group velocity calculated by Eq. (1.26-1.27) (solid lines), by polynomial fit, Eq. (3.1) (dashed line), and experimental group velocity calculated by Hilbert transform (markers).

In Fig. 3.3(b), we present the analytic and experimental phase and group velocity as a function of the carrier frequency of the driver. By definition, for a lossless medium the velocity of the envelope of a wave packet is equal to the group velocity $\partial\omega/\partial k$. In presence of dissipation, the group velocity is not well defined [109], however this definition remains a good approximation taking only the real part of the wave number. The polynomial fit, Eq. (3.1) gives an analytical expression $\omega(k)$ derived from experimental data. Using this fitting expression, we can obtain the phase velocity considering ω/k and the group velocity assuming $\partial\omega/\partial k$. These fitted velocities are denoted with dashed lines. Analytic phase and group velocity from Eq. (1.26-1.27) for a lossless mediium are also shown with solid lines. In addition, we obtained experimentally the group velocity, extracting the envelope of the wave packet using the Hilbert transformation, and calculating its velocity from the spatio-temporal measurements. A good agreement is found between this method and the group velocity curve calculated by the fitting function.

Regarding the dissipative term used in numerical simulation, we consider this to be constant and equal to $\tau = 1.9$ ms, regardless of the driven frequency. Fig. 3.4 shows the maximum of the wave packet velocity along the propagation into the chain for different exciting frequencies. A reasonably good agreement between experiments and numerics is observed. Some differences can be noticed as for example oscillations of the experimental curves between particles 17 to 23 (orange zone), specially for the frequencies 4 and 5kHz. These oscillations, as we mentioned above, could be induced by misalignment of the central particles in the chain leading to reflected waves. Similar kind of oscillations can be observed both in numerics and experiments into the grey zone when reflections appear. When the driven carrier frequency is inside the

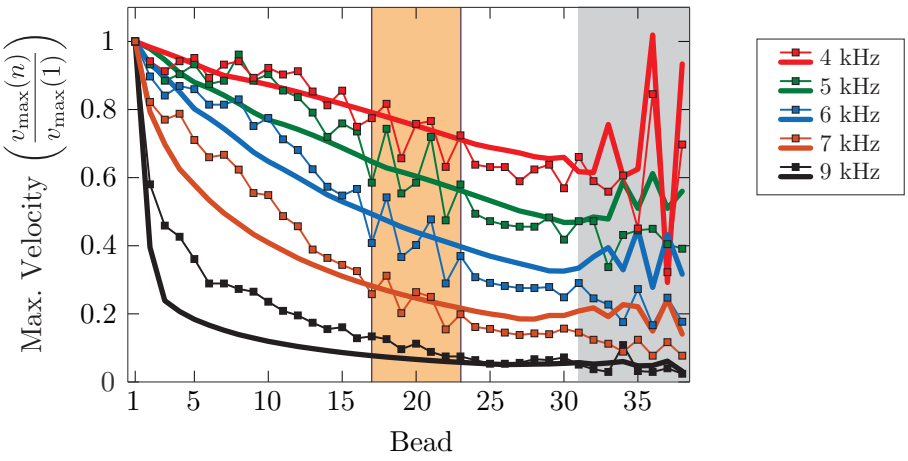

Figure 3.4: Maximum of the wave packet velocity as a function of beads for different carrier frequencies. Thick lines correspond to numerical results with $\tau = 1.9$ ms and $F_0 = 2.25$ N, and thin lines with markers are experimental results. The grey/orange zones correspond to the presence of reflected wave.

forbidden band of propagation (9 kHz), the experimental results are still in good agreement with numerics using the same damping term. Results from frequencies between 1 and 3 kHz are not presented here to relieve the number of curves presented but they are similar to the one at 4 kHz. As a conclusion, the assumption of a on-site, dissipative term which is independent of the driven frequency approximate fairly good the dissipation of the experimental system. Additional numerical simulations have been performed using a damping term between the contact of the particle and similar results have been achieved.

We end this section, by presenting the case at which the granular chain is driven by a continuous harmonic wave (single frequency sinus wave). The driver amplitude is modulated by a linear ramp during the first 4 ms up to a constant value. Fig. 3.5 presents the results for harmonic wave driver inside and outside the propagating band. When the driver frequency is inside the propagating band we can see an increase of the amplitude due to the linear ramp. Lattice waves are generated and they propagate with phase velocity till the end of the chain, where they are reflected. After a certain time the steady state can be obtained. The phase velocity is estimated to 348 m/s which is in accordance with analytical prediction. When the driver frequency is in the band gap, as expected there is no propagation, waves are completely damped after few particles (evanescent regime).

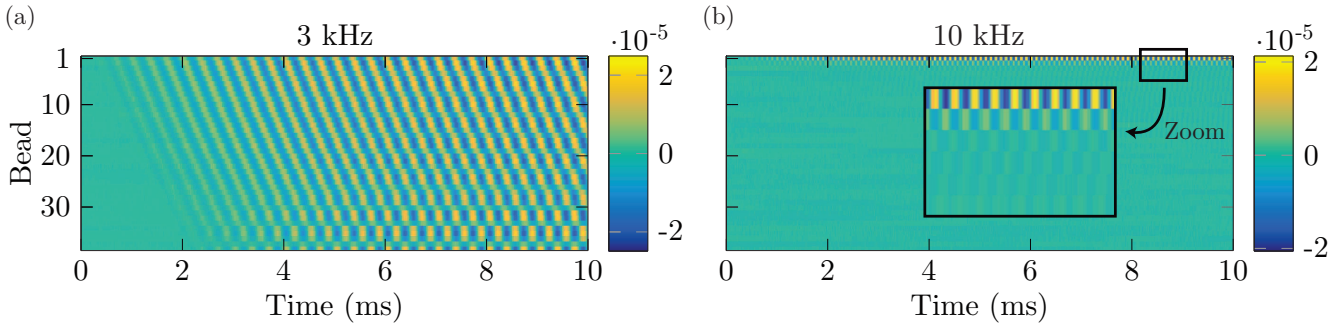

Figure 3.5: Experimental velocity of each particle as function of time for harmonic wave frequency (a) inside and (b) outside the propagating band.

3.2.2 Transverse-Rotational wave propagation: experiments vs numerics

Now, we turn our attention to the propagation of transverse-rotational wave packets. We consider a transverse direction of excitation in relation to the axis of chain. First numerical simulations are presented by using again a 4-th order Runge Kutta method to solve Eq. (2.43) considering a purely transversal driving. Fig. 3.6 presents the numerical results for the transverse and rotational parts along with dispersion curves from the transverse component for two different widths of wave packet with a carrier frequency of 7 kHz.

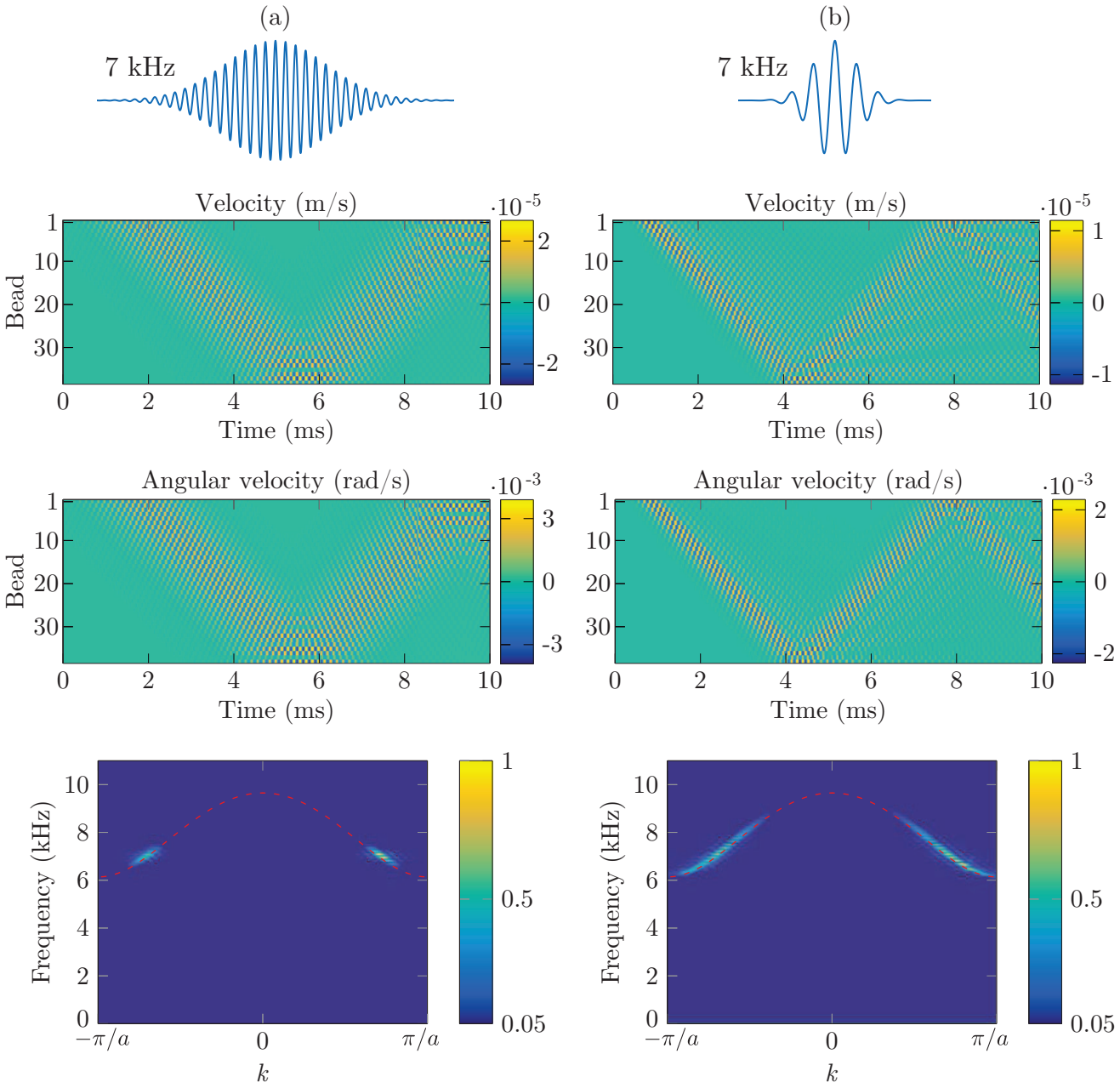

Figure 3.6: Numerical spacio-temporal diagrams of the transverse velocity, angular velocity and dispersion curve for (a) large and (b) short wave packet excitation with a central frequency of 7 kHz, considering $F_0 = 1.2$ N and a lossless configuration. Analytical prediction are superimposed on the dispersion curves (dashed red).

Results are presented by column for a wide, i.e. many periods of the carrier signal, and a short (i.e. few periods) wave packets excitation. Looking to the case with a wide wave packet excitation, panel (a), we can observe that the wave packet is propagating without significant modification of the shape meaning that the dispersion is very weak. The amplitude is remaining constant during the propagation because the medium is considered lossless. The driver is composed only of a transverse component (u_y) and it should be noticed that this component takes part into both transversal and rotational equations of motion in Eq. (2.43). As a result, we can see that transversal and rotational component are excited from the beginning. The dispersion curve related to these results clearly shows that the excited frequency range is small around 7 kHz which is expected due to the large number of periods in the carrier wave packet. The dispersion curve is computed with a signal containing forward and backward waves thus the two directions of propagation are represented in the positive and negative values of the wave number k. Regarding now the case where the driven wave packet is short, i.e. with few periods of signal, presented in panel (b), we observe in the temporal domain a spreading of the wave packet during the propagation. This observation is confirmed by the dispersion curve representation where the excited frequency range is large (in comparison with the panel (a)) and thus the dispersion is stronger.

The wave packet velocity can be determined, as for the longitudinal wave propagation, by following the maximum of the absolute value of the Hilbert transform for the carrier frequency. Let's describe first the analytical phase and group velocities in the transverse-rotational branch $TR(u_z, \phi_y)$. From the previous chapter, the dispersion relation is defined as:

$$\omega = \omega_0 \sqrt{p \cos^2(kR) + \sin^2(kR)}, \tag{3.2}$$

with $\omega_0 = 2\sqrt{K_S/m}$ and $p = \dfrac{mR^2}{I}$. The wave number into the propagating band can be explicitly expressed as:

$$k = \frac{1}{R} \arccos\left(\frac{\sqrt{\omega^2 - 4\omega_0^2}}{2\omega_0\sqrt{p-1}}\right). \tag{3.3}$$

It comes that the phase velocity c_{T_ϕ} in the TR branch is,

$$c_{T_\phi} = \frac{\omega}{k} = \frac{R\omega}{\arccos\left(\frac{\sqrt{\omega^2-4\omega_0^2}}{2\omega_0\sqrt{p-1}}\right)}, \tag{3.4}$$

and the group velocity $c_{T_{gr}}$ is,

$$c_{T_{gr}} = \frac{\partial\omega}{\partial k} = \frac{\omega_0 R(1-p)\sin(2kR)}{\sqrt{(p\cos^2(kR) + \sin^2(kR))}}. \tag{3.5}$$

Fig. 3.7 depicts the analytical phase and group velocities for longitudinal and transverse-rotational branches normalized by the maximum of the longitudinal phase velocity $c_{L_{\phi c}} = 2R\pi f'_L$ where f'_L correspond to

the longitudinal cutoff frequency defined in Eq. (2.25).

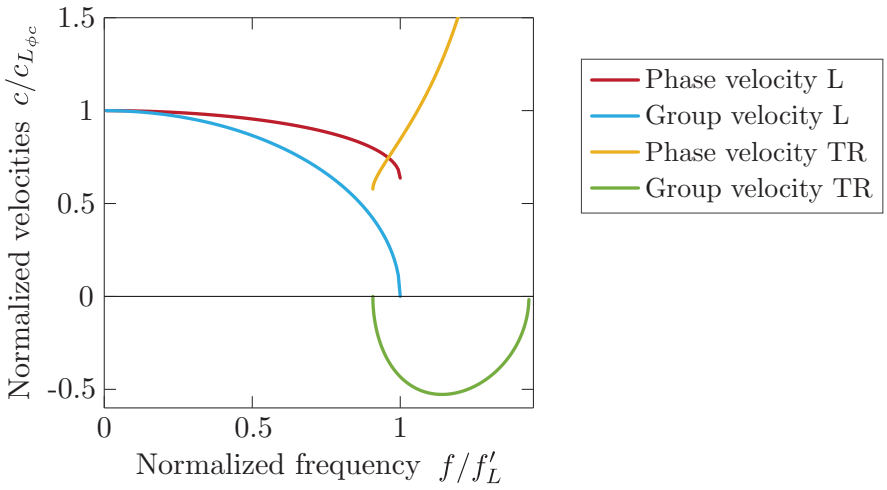

Figure 3.7: Analytical phase and group velocities for the L and TR branches normalized by the maximum of the longitudinal phase velocity $c_{L_{\phi c}}$. The frequency is normalized by the longitudinal cutoff frequency f'_L.

In the TR branch, phase and group velocities have similar shape with the one of the optical branch in a diatomic granular chain. Phase and group velocities have an opposite sign. Experimentally and numerically, we measure a positive group velocity and a negative phase velocity. We can thus compare the estimated value with the absolute value of the analytical predictions. For the case of Fig. 3.6(a) with a central frequency at 7 kHz, the analytical group velocity (Eq. (3.5)) is $c_{T_{gr}} = 163$ m/s which is also found by following the maximum of the wave packet envelope.

Now, we focus on the experimental study of transverse-rotational wave propagation. The transverse transducer (*Panametrics* V1548) is placed to drive horizontally the first bead of chain. The carrier frequency takes values from 4 to 13 kHz considering a short wave packet. The real experimental signal, as presented in Fig. 3.8, measured on the transducer by laser vibrometer (purely transverse signal) is considered as the numerical boundary driver. It is worth mentioning that Eq. (2.43) presents the motion for coupled vertical transverse-rotational motion $TR(u_y, \phi_z)$ but due to the symmetry of the system equations are identical to solve the horizontal problem: $TR(u_z, \phi_y)$. Zero frequency modes are predicted from the theory. In practice, due to the presence of very weak torsional and bending rigidity, instead of zero frequency modes one expects propagating modes at very small frequencies, up to 100 Hz. These are experimentally difficult to be excited (and observed) and thus we will not consider them in our study.

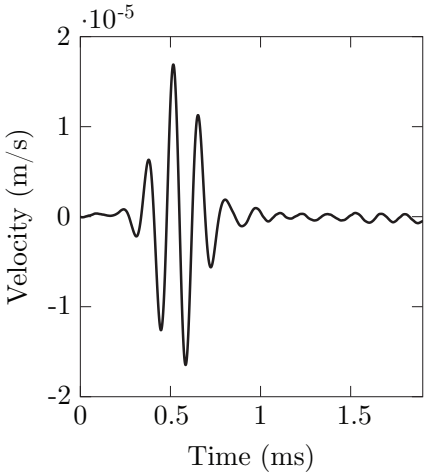

Figure 3.8: Velocity measured on the transducer for a sinus of 7 kHz modulated by a Gaussian function.

In Fig. 3.9, we present the experimental (a) and numerical (b) results for a transverse-rotational

propagation of a wave packet with a central frequency at 7 kHz. A qualitatively good agreement is found between experiments and numerics.

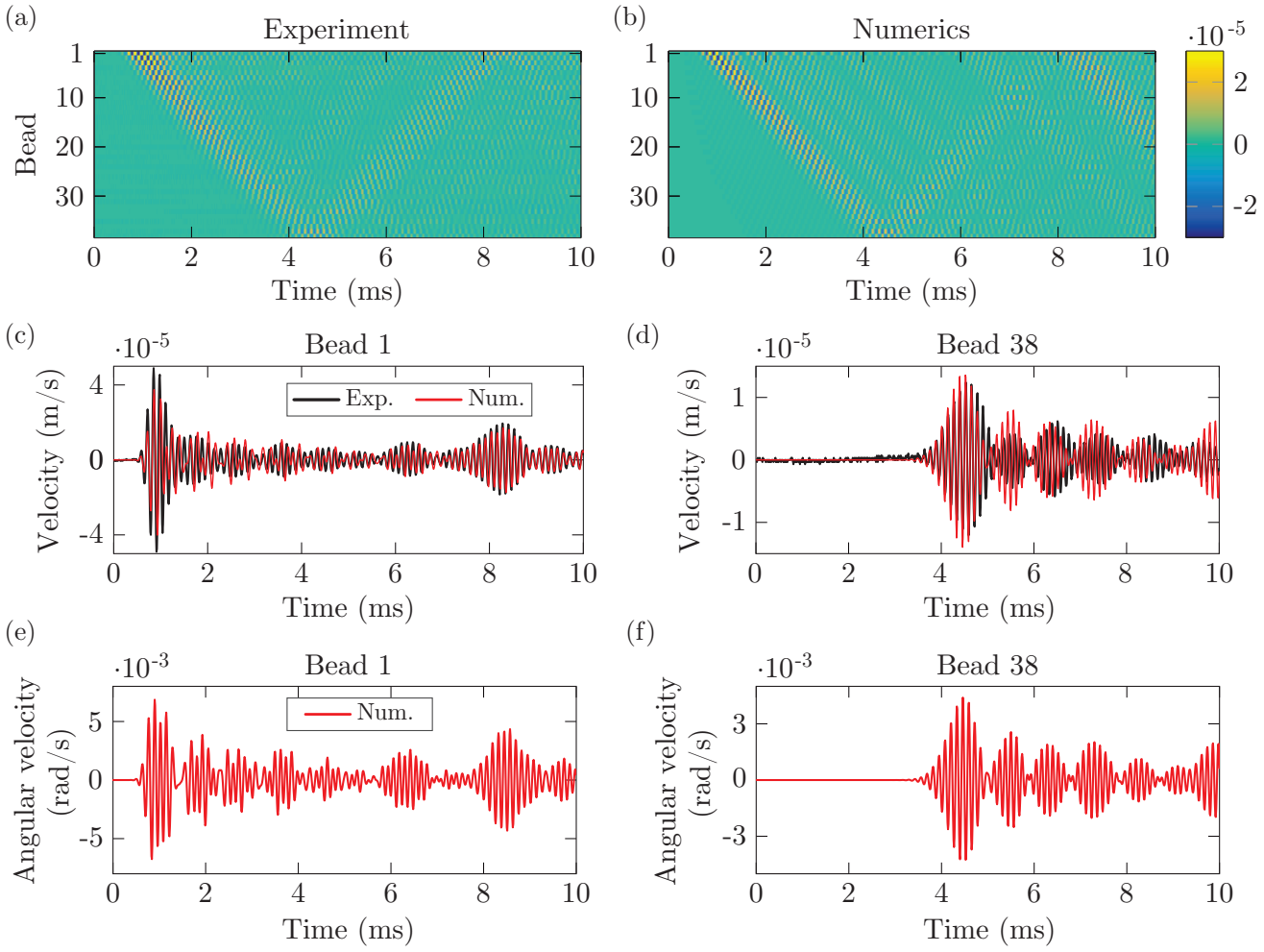

Figure 3.9: (a) Experimental velocity measured for each particle driving with a wave packet with a central frequency of 7 kHz, (b) transverse part from numerics with $F_0 = 1.2$ N and $\tau = 1$ ms. Transverse velocity as a function of time for (c) the first bead and (d) the last bead of the chain. Angular velocity from numerical simulation for (e) the first and (f) the last bead of the chain.

From panels (a),(b), we can observe a different pattern of propagation compared to the longitudinal case. As we will comment below, this is connected with the negative product of group and phase velocity for this propagating band. Regarding the temporal signal measured on the first particle, panel (c), we found a good agreement with numerics. For the last particle of the chain, panel (d), the agreement is less good. To complete the description of the transverse-rotational wave propagation, the rotational part obtained from numerics is shown on panel (e-f). It should be noticed again that the laser vibrometer is not sensitive to rotation, thus experimentally, only transverse displacements are recorded. As we can see, although the chain is excited by a purely transverse wave packet, rotational motion is also excited. As we mentioned in the previous chapter, the system supports coupled transverse-rotational waves. The percentage of rotational motion in the coupled TR propagating wave depends on the frequency. For

example, for the case of 7 kHz studied here, the theory predicts 55 % of rotation which is confirmed by the simulations.

The wave packet velocity is determined by following the maximum of the envelope for the carrier frequency. Fig. 3.10 depicts the analytical phase and group velocities for longitudinal and transverse-rotational branches with the experimental results. As commented above, phase and group velocities have an opposite sign. Experimentally, we can measured only positive group velocity and a negative phase velocity. Due to that we present the absolute value of the group velocity in dashed line in order to compare with the experimental results.

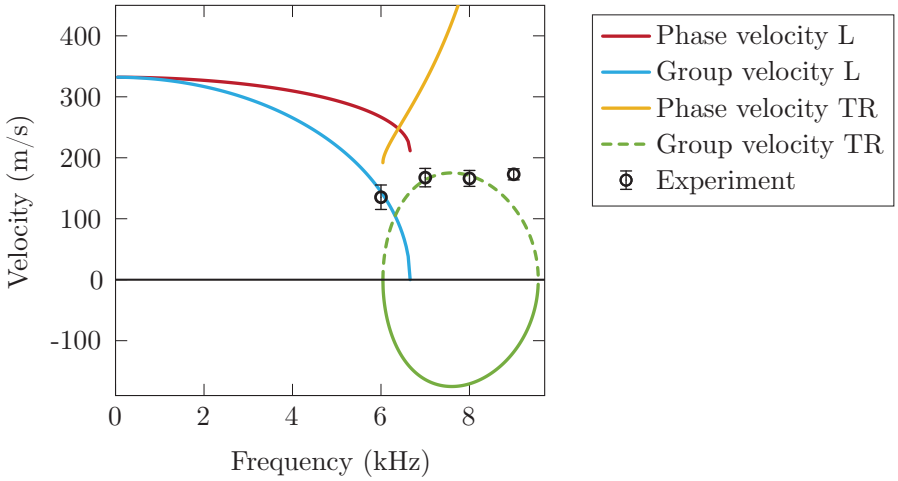

Figure 3.10: Analytical phase and group velocities for the L and TR branches. The dashed line correspond to the absolute value of the analytical group velocity in TR branch, markers correspond to the experimental results.

We can observe a good agreement for the experimental velocity with the analytical prediction for frequencies 7 and 8 kHz. Close to the cutoff frequencies (6 and 9kHz), the group velocity becomes very slow and the dispersion very strong. The wave packet is strongly spread out during the propagation leading to more inaccurate estimation of the velocity. Moreover for the higher frequency 9 kHz, we expect from theory more rotation than transverse motion. Thus the measured velocity of the transverse part could be over or underestimated.

Let's take a look to the maximum velocity (in the transverse direction) of the wave packet as this propagates along the chain. Fig. 3.11 displays the results for a frequency inside the propagating band and two frequencies outside (one in the lower gap and one in the higher gap). Numerical simulations are computed using the same damping term $\tau = 1$ ms regardless of the frequency of excitation. To be consistent with the experimental results, we calculate the maximum velocity of the transverse direction.

An acceptable agreement is found between experimental and numerical results. The wave packet velocity in the propagating band is less attenuated than in the band gap as it is expected. More attenuation is found when the driver is in the lower gap. In this case, it should be noticed that the driving frequency is into the gap for the TR branch but inside the propagative band of the L branch. Experimentally, we

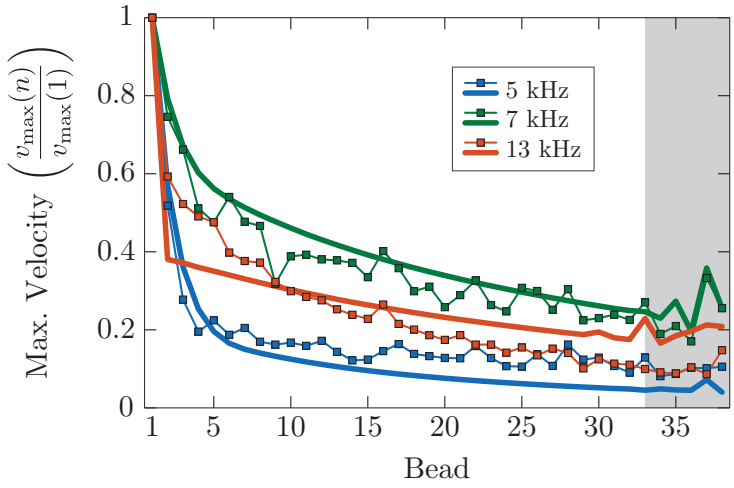

Figure 3.11: Maximum of the pulse for each particle considering one frequency in the propagative band (7 kHz) and two in the band gap (5 and 13 kHz). Thick lines correspond to numerical results with $\tau = 1$ ms and $F_0 = 1.2$ N, and thin lines are experimental results. The grey zone corresponds to the presence of reflected wave.

can expect that a misalignment of the driver and the chain, will cause a possible conversion of mode from transverse to longitudinal which could lead to lower energy transmitted in TR pulse. Numerically this mode conversion is not allowed thus we can exclude this assumption. Numerical simulations capture well the attenuation in the propagating band as well as in the forbidden bands keeping the same damping term.

Let us turn on the TR wave propagation by single harmonic frequency driver. The amplitude of the driver is still modulated by a linear ramp at the beginning. Fig. 3.12 shows the propagation of harmonic wave inside (8 kHz) and outside the propagation band in the lower band gap (4 kHz).

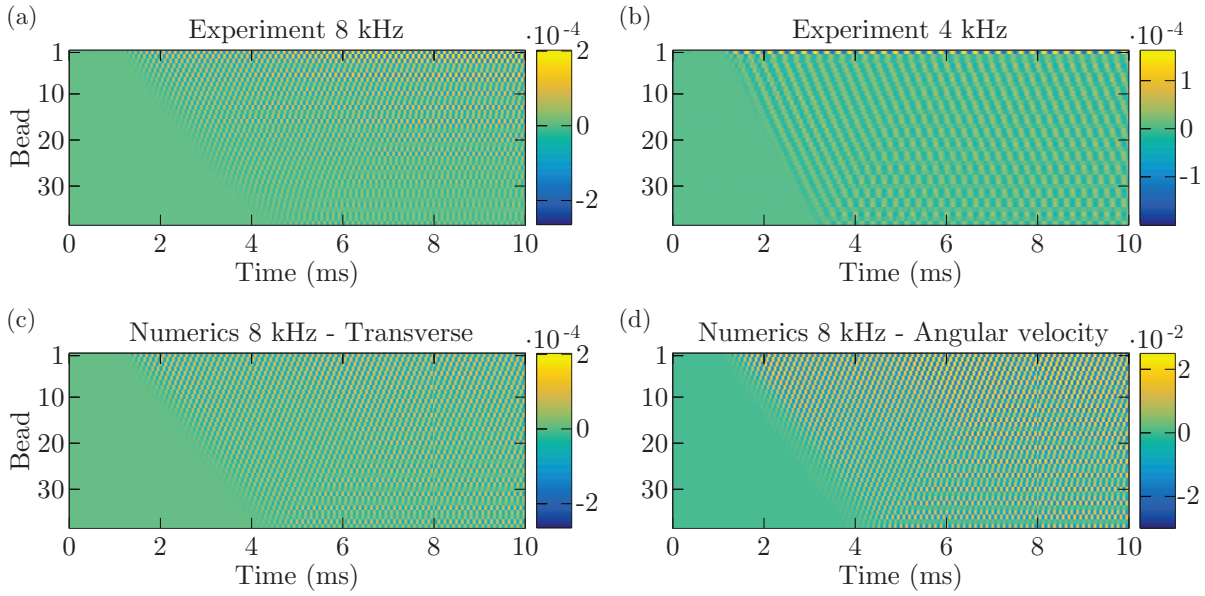

Figure 3.12: Experimental velocity of each particle for single harmonic wave driving frequency (a) inside and (b) outside of the propagative band (in the lower band gap). (c-d) Numerical results corresponding to the driving frequency inside the propagative band for (c) transverse velocity and (d) angular velocity components.

When the driver frequency is inside the propagating band, panel (a), we can observe a wave propagation regime and a stationary regime (steady state). The numerical results, panel (c), are in good agreement with experiments. It should be noticed that in the experimental results, there are in addition reflected waves which is an indicator of misalignment of particles. When the driver frequency is inside the lower band gap, panel (b), we can see a high amplitude of the velocity for the first particle followed by a quick decrease inside the chain (evanescent regime). Even if the amplitude is small in comparison with the first particle, a wave propagates all along the chain. This propagation is not predicted by our model. The most interesting is the pattern of the wave propagation into the chain which corresponds in fact to a longitudinal wave. The wave velocity is estimated at 324 m/s corresponding indeed to a longitudinal wave velocity. We have to notice, that we are able to measure this longitudinal component because the laser vibrometer is measuring with an angle from the axis formed by the center of the beads. Additional measurement with the vibrometer perpendicular to the chain has been realized and indeed only the evanescent transversal/rotational regime is observable. The first assumption to explain this longitudinal wave propagation could be the misalignment of the transverse driver and/or of the particles into the chain which could lead to mode conversion from TR to L. The second explanation is the driver itself. Indeed, the shear transducer is never sending pure transverse motion but transverse and small component of longitudinal motion. From the manufacturer's datasheet of the transducer, it exists a ratio between the longitudinal (u_x) and transverse (u_y) component defined as:

$$G_{L/T} = 20 \log_{10} \left(\frac{u_x}{u_y} \right) < -30 \text{ dB}. \tag{3.6}$$

We experimentally estimate this ratio by making the decomposition of the velocity presented in section 2.4.1 and we find $G_{L/T} = -39$ dB at 4 kHz. Thus, the shear transducer is obviously participating to excite longitudinal motion but the misalignment of the particles can also plays a role leading to stronger longitudinal wave propagation by mode conversion.

3.2.3 Summary

The complete linear wave propagation in L and TR branches is experimentally realized for wave packets and harmonic wave signals. Numerical simulations, using the experimental signal of the driver as a driving boundary, are used in order to estimate the precompression force and the attenuation in the chain. Viscous on-site damping are taken into account only for the displacement component (not directly to the rotational part in the TR branch). The damping term τ is fitted for one driven frequency for each polarization of excitation. As a first good approximation, these fitted values can be used for other driven frequencies to describe the wave attenuation during the propagation. It should be noticed that different attenuation values are found between L and TR modes. Experimental and numerical results are in good accordance for all results. In addition, unexpected reflected waves have been observed during the propagation of wave packets which are probably due to misalignment of particles.

Following the propagation of the envelope of the wave packet a good approximation of the group

velocity for both L and TR chains comparing with analytical predictions was found.

Finally, the longitudinal component of the shear transducer and its possible role on the experimental measured longitudinal waves after transverse excitation have been highlighted.

3.3 Second harmonic generation in a finite granular chain

This section is devoted to the study of the second harmonic generation in a finite granular chain. The chain is longitudinally driven at one extremity and both the effect of reflections, due to the finite size of the chain, and dissipation are studied.

When harmonics are generated in a dispersive medium the interaction between the fundamental frequency and the second harmonic is modified. Considering the basic dispersion curve of a 1D granular chain, Fig. 3.13, several zones in frequency can be determined leading to different phenomena during the harmonic generation. (i) At very low frequency range, the dispersion relation is quasi-linear for the fundamental but also for the higher harmonics thus the dispersion can be neglected. (ii) Increasing slightly the frequency, weak dispersion appears which could lead to different wave speeds of the different harmonics. In this regime there are different cases, for example one case is when the second harmonic could travel with almost the same velocity than the fundamental, meaning that the dispersion can still be neglected for this harmonic but higher harmonics are in the dispersive regime leading to different wave velocities. A more interesting case in this regime is when even the second harmonic is located in the dispersive regime, a case that leads to a spatial beating in amplitude depending on matching conditions [126]. (iii) Higher harmonics, for example the second or the third are in the band gap of the structure, and in this case the wave propagation for these harmonics is considered as evanescent.

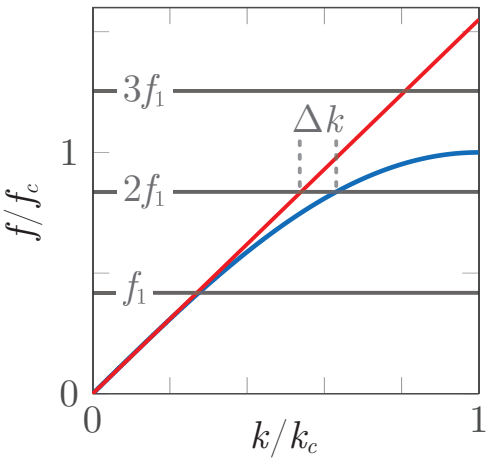

Figure 3.13: Representation of the dispersion curve of a monoatomic granular chain, linear relation and representation of the wave number mismatch Δk.

For this section, we will focused in the regime where the fundamental f_1 and the second harmonic are located in the propagating band while the third harmonic in the forbidden gap, i.e. $f_1/f_c < 0.5$ where f_c is the linear cutoff frequency of the system. The second harmonic is in the strong dispersive regime of the dispersion relation. First, we study the harmonic generation through numerical analysis and then we present the experimental results.

3.3.1 Numerical analysis

For the numerical analysis, we solve by fourth order Runge Kutta method the following equations of motion considering the Hertzian contact law:

$$m\ddot{u}_n = A\left[\delta_0 + u_{n-1} - u_n\right]_+^{3/2} - A\left[\delta_0 + u_n - u_{n+1}\right]_+^{3/2} - \frac{m}{\tau}\dot{u}_n. \tag{3.7}$$

The difference with Eq. (1.16) presented in the first chapter, is the presence of a dissipative term τ corresponding to a phenomenological viscous on-site dissipation. In Ref. [127], analytical predictions for

the generation of the second harmonic in the presence or not of the dispersion have been presented by expanding Eq. (3.7) in series (quadratic approximation) and using successive approximation approach. In the dispersive case, this study shows the presence of the well-known effect of beating for the second harmonic considering a semi-infinite granular chain (no reflected wave) and without considering dissipation in the system.

3.3.1.1 Absence of reflection

We start our numerical analysis by neglecting the dissipative term τ. Fig. 3.14 presents the amplitudes of the fundamental, second and third harmonic for two different amplitudes of excitation. The amplitude is normalized by the maximum of the fundamental amplitude. The chain is composed of 520 particles which permits to obtain propagating waves containing only forward waves for the 100 first sites. The precompression between particles is adjusted to $F_0 = 1.7$ N leading to a linear cutoff frequency of the chain at $f_c = 7.17$ kHz. The driving frequency is at 3 kHz, $f_1/f_c = 0.42$ corresponding to a second harmonic at 6 kHz in the propagating band but the third harmonic at 9 kHz in the band gap. The first case, which is presented in Fig. 3.14(a) considers small amplitude of excitation with the maximum of displacement very small in comparison to the static overlap ($\delta/\delta_0 = 3{\cdot}10^{-4}$). In this case, the regime can be considered as near-linear and no strong harmonic generation is expected. Considering a larger amplitude

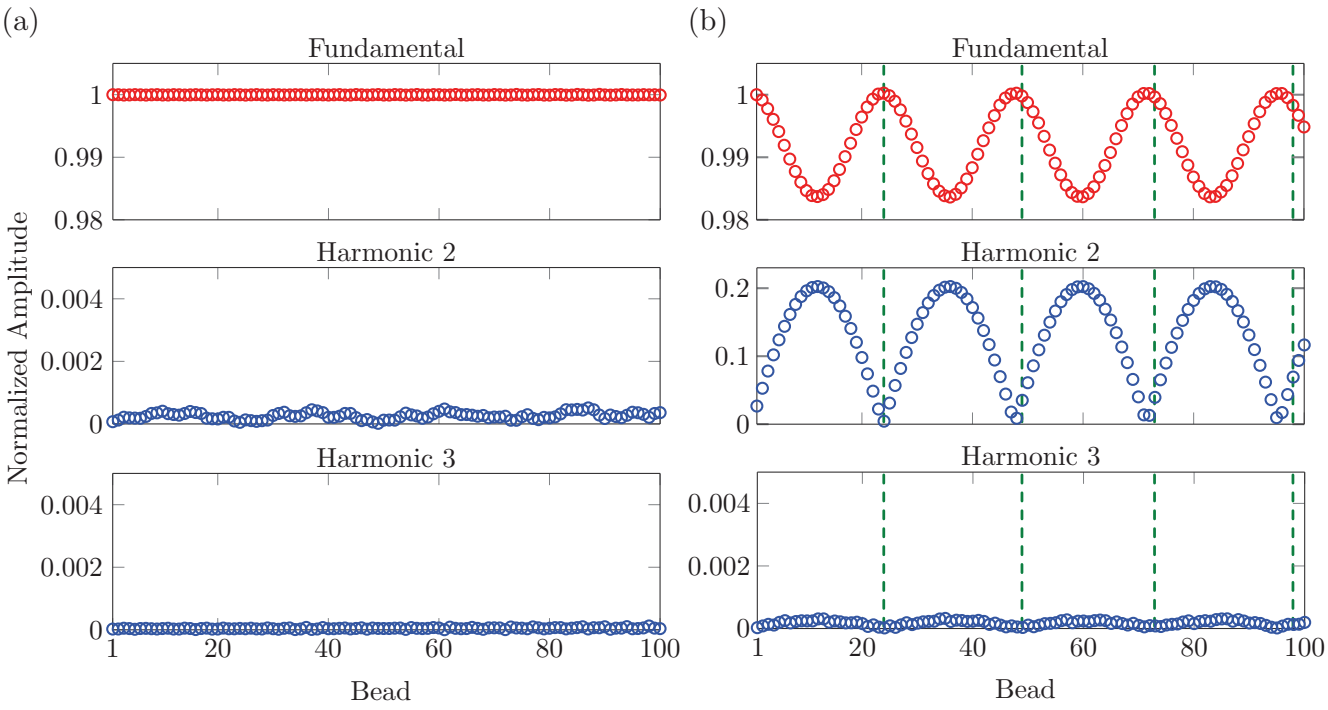

Figure 3.14: Normalized amplitude of the fundamental, second and third harmonics considering lossless propagation for displacement amplitudes (a) $\delta/\delta_0 = 3 \cdot 10^{-4}$ and (b) $\delta/\delta_0 = 0.19$, for both cases $f_1/f_c = 0.42$. Green dashed line are analytical predictions of the disappearance of the second harmonic contribution from Eq. (3.8).

of excitation, with $\delta/\delta_0 = 0.19$, Fig. 3.14(b), the second harmonic is strongly generated. We can observe a maximum of the fundamental amplitude when the second harmonic contribution is minimum. The site

n of this minimum can be predicted by

$$n = \frac{2l\pi}{\Delta k}, \tag{3.8}$$

where $l \in \mathbb{N}^+$ and the detuning parameter Δk that describes the asynchronous second harmonic generation is defined as

$$\Delta k = \left| 2k\left(\frac{\omega}{\omega_c}\right) - k\left(\frac{2\omega}{\omega_c}\right) \right|. \tag{3.9}$$

For this configuration $n \approx 24, 49, 73, 98$ which is in good agreement with the numerical results (green dashed lines). The third harmonic is in the forbidden band of propagation. In order to be closer to the realistic wave propagation in granular chains, we add the dissipative term τ to the numerical simulations as presented in Eq. (3.7). Fig. 3.15 presents the results of the harmonic generation without wave reflections for two different cases, a weakly lossy case with $\tau = 10$ ms (blue circles) and a strongly lossy case with $\tau = 1$ ms (black diamonds).

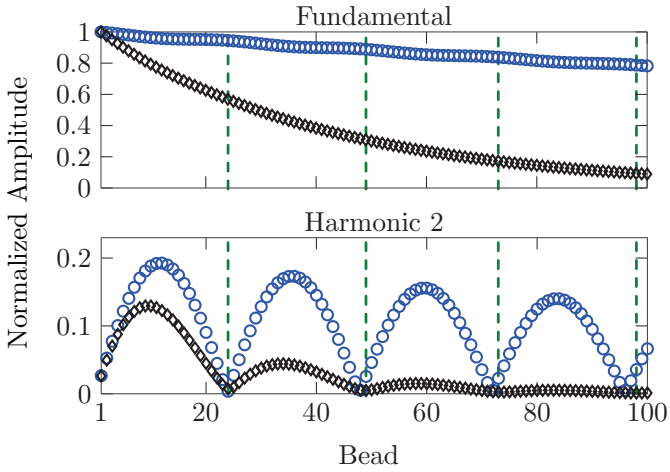

Figure 3.15: Normalized amplitude of the fundamental and second harmonic considering lossy propagation for displacement amplitudes $\delta/\delta_0 = 0.19$ and $f_1/f_c = 0.42$. Blue circles correspond to a dissipative term $\tau = 10$ ms and black diamonds to $\tau = 1$ ms. Green dashed line are analytical prediction of the disappearance of the second harmonic contribution from Eq. (3.8).

On Fig. 3.15, we can see that the amplitude of the fundamental and the maxima of the second harmonic are reduced as the wave propagates within the chain. We also note that despite the presence of dissipation, the second harmonic vanishes at the same particles than in the case without losses.

3.3.1.2 Presence of reflection

The theory of the beating of the second harmonic assumes the absence of reflected waves during the signal analysis. However, due to the finite size of the granular chain, it should be useful to study the effect of reflected waves on the beating of the second harmonic. Fig. 3.16 presents the amplitude of the fundamental and second harmonic for a chain composed of 150 particles considering driven-free boundary

conditions. As presented in panel (b), the wave is reflected at the end the chain leading to an increase of the presence of reflected components as the bead site is closer and closer to the free boundary. Grey

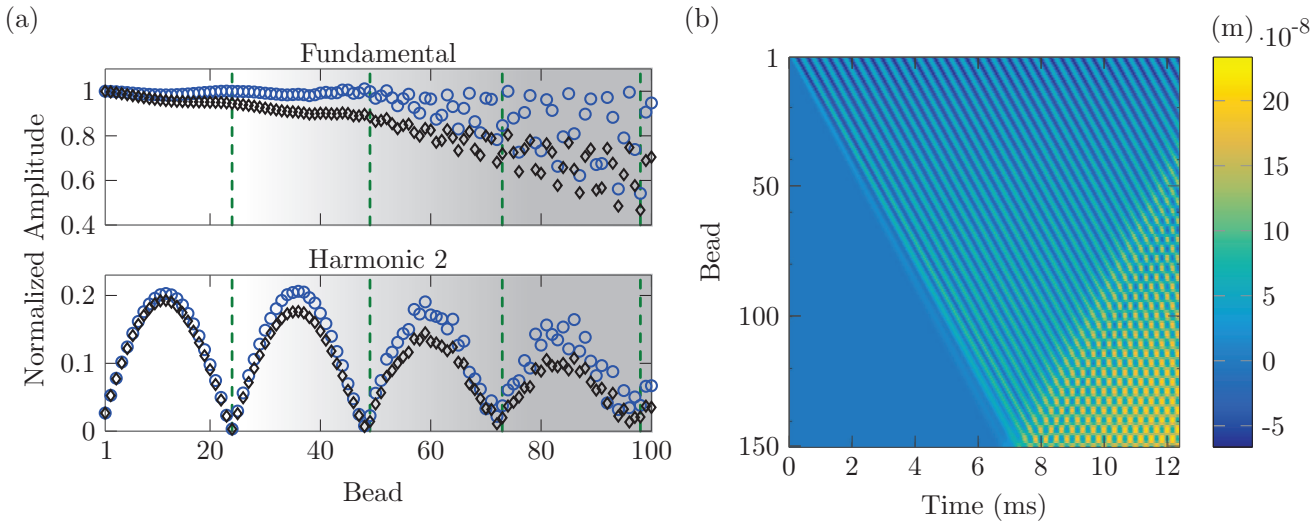

Figure 3.16: (a) Normalized amplitude of the fundamental and second harmonic for a displacement amplitude $\delta/\delta_0 = 0.19$ and $f_1/f_c = 0.41$ when reflected wave is present. Blue circles correspond to a lossless case and black diamonds to a dissipative case with $\tau = 10$ ms. Grey zones correspond to the presence of reflection during the analysis. Green dashed line are analytical predictions of the disappearance of the second harmonic contribution from Eq. (3.8). (b) Displacement of each particle of the chain as a function of time.

zones in Fig. 3.16(a), are added to represent the presence of reflected wave into the analysis. Before the presence of reflected wave, the results are the same than previously presented. The presence of reflected wave disrupts the beating phenomenon and finally when the reflected part is strong the beating disappears but the second harmonic is still present.

3.3.2 Experimental observation of the second harmonic generation

The objective of this section is to experimentally observe the second harmonic generation into the free suspended granular chain. The experimental setup is identical to the one of Fig. 2.22. The velocity of each particle of the 38-beads chain is measured by a laser vibrometer. The chain is driven by a piezo electric transducer at one extremity by harmonic waves created with a *Tektronix* signal generator. Such generator allows to create harmonic waves starting with a linear ramp in amplitude. As in numerical simulation, the use of a linear ramp enables to excite the chain smoothly in amplitude which ensure the good harmonic wave driving. Indeed without linear ramp, the transducer could "strike" the chain because of a strong amplitude of displacement leading to the excitation of a wide band of frequencies. The velocity recorded on the transducer is presented in Fig. 3.17(a) in the temporal domain where we can observe the linear ramp in amplitude at the beginning of the signal. The spectral component of the driver is shown in panel (b) for a driving frequency of 3 kHz. This frequency analysis of the transducer signal depicts very small contribution of second, third and fourth harmonics in comparison with the fundamental amplitude (more than 50 dB of difference). On panel (c), the velocity of each particle as a function of time is represented

for the signal onset (left) and after a certain time (right). Fig. 3.17(c) depicts different dynamical regimes

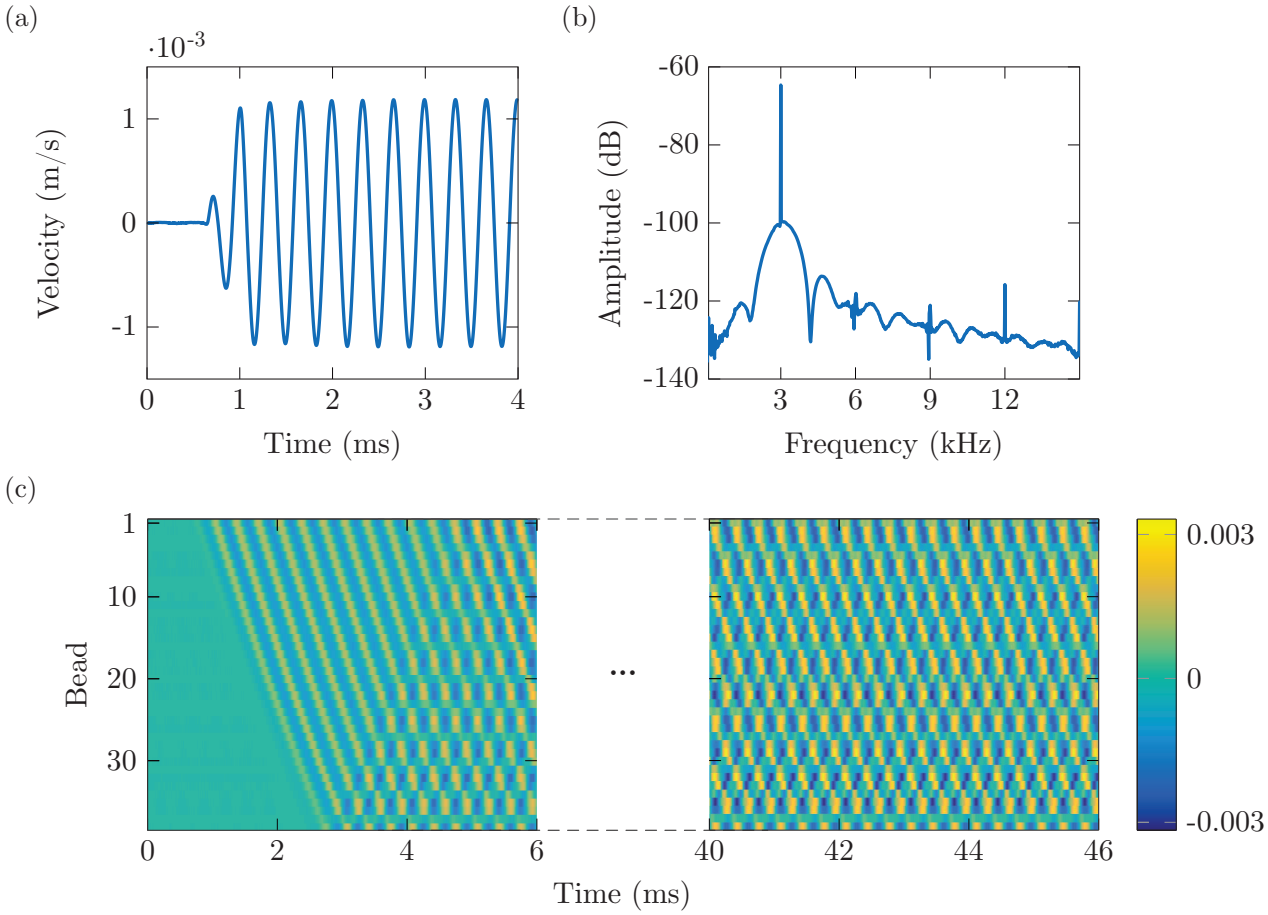

Figure 3.17: Experimental velocity of the transducer with a linear ramp in amplitude for a driving frequency of 3 kHz in (a) temporal and (b) frequency domains. (c) Velocity of each particle of the chain for the onset time (left) and after a certain time (steady state) (right).

of the wave propagation. The first one, between the time 0 to 3 ms, is the propagation without reflected wave followed by a transient dynamics where forward and backward waves are interacting, between the time 3 to 6 ms. After a certain time, from 40 to 46 ms for example, the forward and backward waves get mixed up reaching a stationary dynamic (steady state). The latter two regimes will be studied in more details in the section 3.3.3.

Let us focus on the first part of the signal where there is only a small part of reflected wave. As it has been shown in the previous section, the presence of reflected wave has to be minimized during the analysis in order to obtain the beating phenomenon of the second harmonic. To do so, we take only one period of the signal close to its beginning during the analysis. Starting the analysis on the first period just after the linear ramp and repeating this for the two following periods allows to get rid of the reflection up to the 27-th particle. Numerical simulations are used to fit the precompression and the damping term of the experimental results. The precompression is found to be $F_0 = 1.8$ N leading to a cutoff frequency at $f_c = 7.24$ kHz and the damping term is $\tau = 1.9$ ms. Fig. 3.18 presents the experimental and numerical results for a driving fundamental frequency at 3 kHz ($f_1/f_c = 0.41$) and 5 kHz ($f_1/f_c = 0.69$). The

experimental velocity signal recorded on the transducer is used as the driver for the numerical simulation. The maximum of displacement in comparison with the static overlap is $\delta/\delta_0 = 0.19$, ensuring that we are in the nonlinear regime.

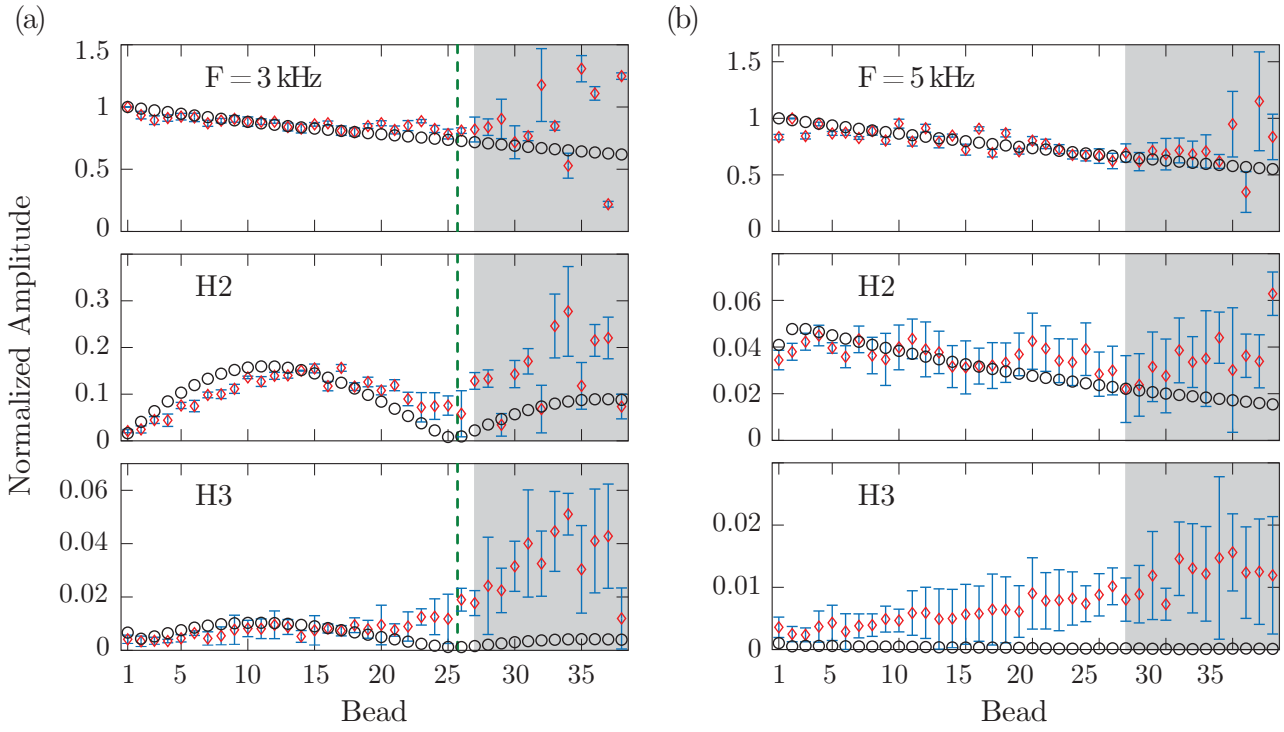

Figure 3.18: Experimental and numerical harmonic generation for a driving frequency at (a) 3 kHz: $f_1/f_c = 0.41$ and (b) 5 kHz: $f_1/f_c = 0.69$. Black circles correspond to numerics and red diamonds to experiment, respectively. Green dashed line is given from Eq. (3.8). Grey zones correspond to the experimental presence of reflection during the analysis.

The numerical results, presented in Fig. 3.18, are made for a large chain of 238 particles to avoid completely the reflected wave during the analysis. Panel (a) depicts the harmonic generation for a driving frequency at 3 kHz. In this case the second harmonic (H2) is inside the propagating band while the third harmonic (H3) in the gap. From Eq. (3.8) the vanishing of the second harmonic is predicted at the 26-th bead, shown by the green dashed line. Red diamonds represent the mean value of the frequency amplitude and the error-bars correspond to the standard deviation found from the 3 periods analysis. Looking at the experimental results, when there is no reflected wave (white zone) we find a very good agreement on the fundamental, second and third harmonics dynamics compared to numerics. We can observe that the third harmonic (inside the band gap) has a really small amplitude. Regarding the results with the presence of reflected waves (grey zone), as it is expected, the experimental results do not capture the beating phenomenon and moreover the standard deviation clearly increases into this regime. To confirm this result, we present on Fig. 3.19 the experimental and numerical temporal signal for different bead positions during the first beating phenomenon (from particle 1 to 26). We still observe a good agreement in this temporal representation. Fig. 3.18(b) presents the configuration where the driving frequency is 5 kHz, in this case the second and third harmonics are in the forbidden band of propagation. Once again,

the results are in very good agreement, the second and third harmonic get a very small amplitude. The experimental data for the second and third harmonic have a bigger standard deviation due to a small signal to noise ratio.

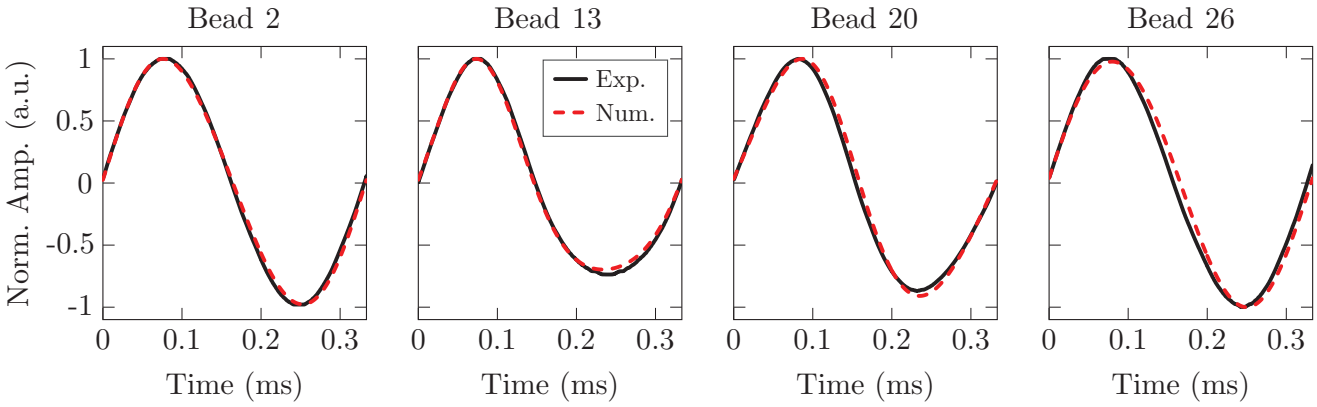

Figure 3.19: Temporal signal of bead 2, 13, 26, 20, for a driving frequency at 3 kHz, corresponding to the beginning of the chain, middle of the harmonic beating, at the end of the beating and in between, respectively. Solid black lines and dashed red lines correspond to experimental and numerical results, respectively.

Now, we modify the fundamental driving frequency keeping the second harmonic into the propagating band, in order to observe the change in bead position of the second harmonic vanishing. Fig. 3.20 shows results for fundamental frequency at $f_1 = 3.2$ kHz ($f_1/f_c = 0.44$) and $f_1 = 3.4$ kHz ($f_1/f_c = 0.47$). From Eq. (3.8), we expect disappearance of the second harmonic contribution at bead 19 and 37 for the fundamental 3.2 kHz and at bead 13 and 26 for the 3.4 kHz. The maximum of displacement in comparison with the static overlap is kept to $\delta/\delta_0 = 0.19$.

From Fig. 3.20, we conclude that the experimental results are in accordance with the numerical results. The beating of the second harmonic is well observed and corresponds to the analytical prediction for the position of disappearance of the second harmonic. It should be noticed that for all the numerical analysis, the value of the damping term is $\tau = 1.9$ ms. From the previous section, studying the linear wave propagation for several frequencies, it seems that this fitted value is a good approximation. We can expect that in reality the dissipation could change as we change the amplitude of the driver, thus a nonlinear model for the dissipation could be more appropriate, as the one developped in [128–130]. The aim here is to keep the simplest model capturing well the wave propagation which is the case for these results.

3.3.3 Frequency analysis in different dynamical regimes

This section describes in more details the different dynamical regimes of the granular chain and in particular the steady state regime.

Fig. 3.21 shows the experimental frequency components as a function of the time for different particles for a driving frequency at 3 kHz. Particles have been chosen to be at a maximum (bead 10) or minimum (bead 16) of displacement when the steady state is achieved. The bead 26 is chosen because it corresponds to the site where the contribution of the second harmonic disappears during the beating phenomena.

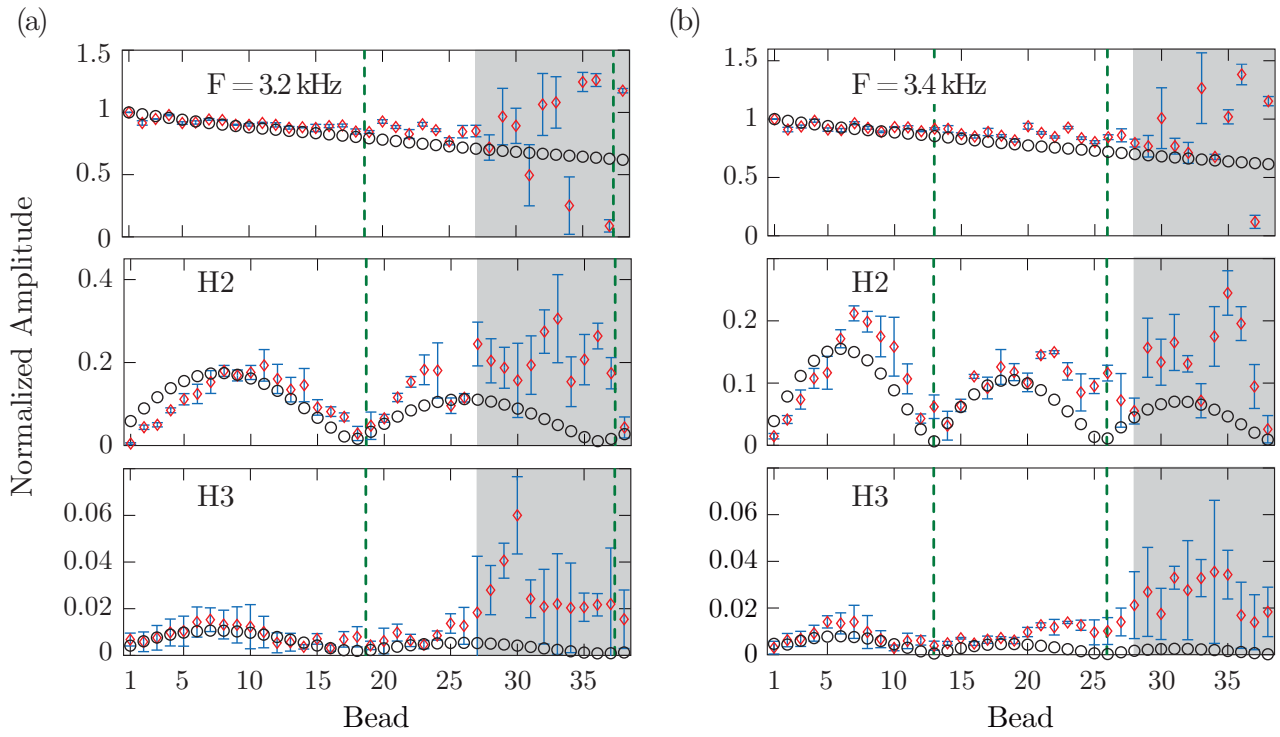

Figure 3.20: Experimental and numerical harmonic generation for a driving frequency of (a) 3.2 kHz: $f_1/f_c = 0.44$ and (b) 3.4 kHz: $f_1/f_c = 0.47$. Black circles correspond to numerics and red diamonds to experiment, respectively. Green dashed line from Eq. (3.8). Grey zones correspond to the experimental presence of reflection during the analysis.

From Fig. 3.21, three dynamical regimes can be determined. As presented before for the temporal domain

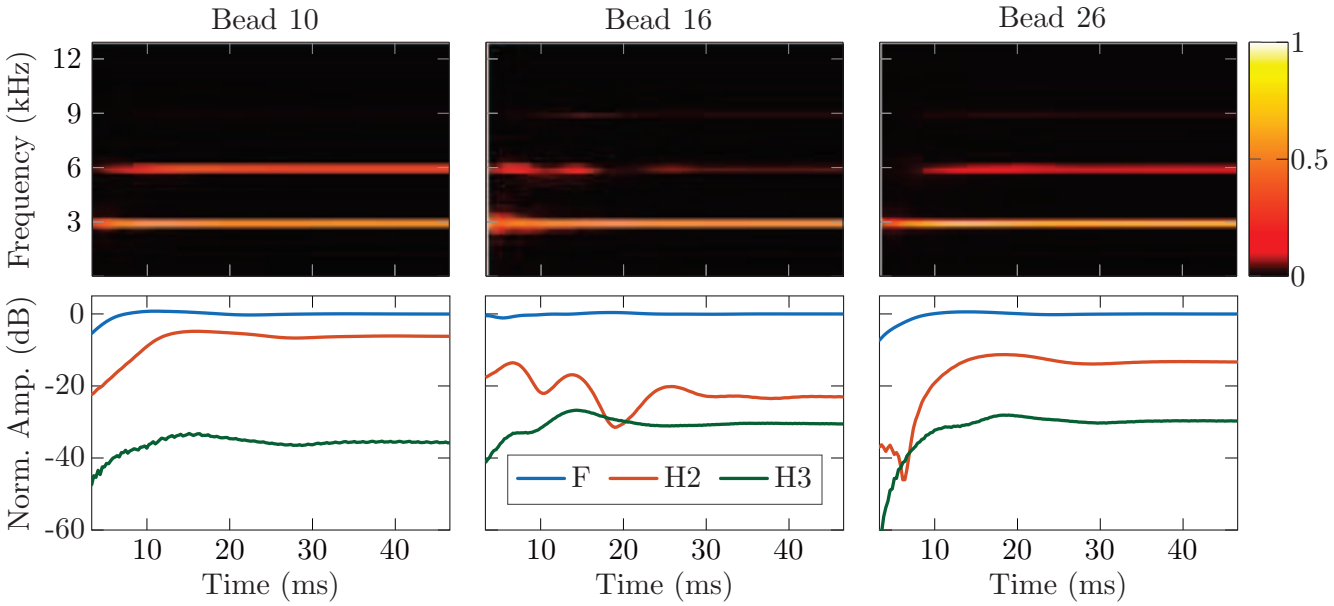

Figure 3.21: (Top) Experimental spectrogram for bead 10, 16, 26 and (bottom) amplitude of the fundamental (F - blue), second harmonic (H2 - red) and third harmonic (H3 - green) normalized by the maximum the fundamental when steady state is achieved for each bead from experimental results.

(Fig. 3.17(c)), the first regime, between 0 and 3 ms, is the propagation without reflected wave. The second one, from 3 to 30 ms, is a transient dynamics with both forward and backward waves. Finally the last one, from 30 to 50 ms, the forward and backward waves lead to a steady state. It should be noticed that in this case, the mode is nonlinear because it is composed of several frequencies.

Looking at the frequency components in the transient regime for particle 26, where the beating is at the minimum, we can see that the amplitude of the second harmonic is constant during few milliseconds before growing up to the stable regime. Looking at the frequency components in the steady state, particle 10, with a maximum of displacement, has a strong presence of the second harmonic (less than 10 dB between the fundamental and the second harmonic). For particle 16, corresponding to a minimum of displacement, the second harmonic is 20 dB smaller than the fundamental.

Fig. 3.22 presents the steady state of the experiments and numerics. We can see that the pattern of the

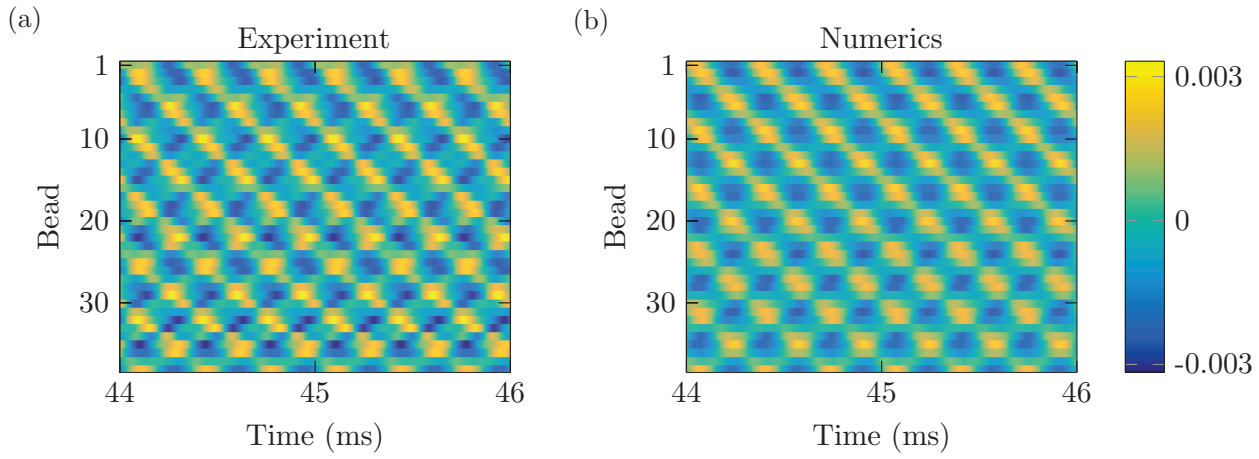

Figure 3.22: Velocity of each particle for a driven frequency at 3 kHz when the steady state is achieved for (a) experimental and (b) numerical results.

mode is different between experimental and numerical results. Numerically, the studied chain is perfectly aligned and the precompression is considered to be homogeneous all along the chain which is not the case in reality. Normalizing the amplitude of the second harmonic by the amplitude of the fundamental for each particle, we find that the mean amplitude of second harmonic in the experimental chain is 10 dB lower than the fundamental with a standard deviation equal to 8 dB. For the numerical results we find a mean value of the second harmonic 15 dB lower than the fundamental with a standard deviation equal to 6 dB. These results show that the second harmonic is strongly present in the steady state.

3.3.4 Summary

The second harmonic generation in a finite granular chain has been numerically described. When reflected waves and dissipation are neglected, the well-known beating in amplitude of the second harmonic have been shown. By adding attenuation in the propagation, the amplitude of the second harmonic is decreasing as a function of the depth into the chain but the sites where the second harmonic disappear are the same as in the lossless case. In the presence of reflected waves, we observe that the beating phenomenon is

not captured. Finally, experimental evidence of the beating phenomenon in a granular chain has been observed. Several driven frequencies have been tested and the harmonic generation is in good agreement with analytical and numerical predictions. The amplitude and the sites where the second harmonic is vanishing are well recovered. The presence of strong second harmonic in the stationary regime has been also shown.

Additional measurements have been realized for the harmonic generation in the TR branch. For the same electric voltage, it was not possible to achieve harmonic generation in this propagating branch. Thus, these preliminary experiments can support the linear modeling of TR propagation for the same range of amplitude excitations.

3.4 Γ-shaped granular chain: mode conversion and harmonic filtering

The propagation of elastic waves in a one-dimensional granular chain has been fully described in chapter 2 and in the beginning of chapter 3. In this section, we extend the study to the wave propagation through a granular setup deviating from a simple one-dimensional granular chain. Taking advantage of the external magnetic field to induce attractive forces between the particles, various shapes can be easily built, such as curved chain, zigzag chain, honeycomb, and hexagonal lattices. The new proposed granular structure that we will study in this section is composed of two simple granular chains linked perpendicularly at those extremities, forming a "Γ"-shaped chain, see Fig 3.24. From the previous results presented in chapter 2, we theoretically and experimentally observe that coupled transversal-rotational modes can be excited using a transverse driver. In the Γ-shaped configuration, if we drive longitudinally the first chain, the resulted longitudinal wave will propagate up to its end where the second chain is linked. Thus, the last bead of the first chain becomes a transverse driver for the second chain exciting transverse-rotational modes. Thus, a conversion from longitudinal to transverse-rotational modes due to geometry is achieved. The conversion from shear to longitudinal mode has been experimentally and theoretically shown in a three-dimensional granular packing of mm-size glass beads [131] via the second harmonic generation. In two dimensional granular structures, the conversion from shear to longitudinal mode has been theoretically and numerically investigated also via second second harmonic generation in an hexagonal structure composed of micro-spheres [132].

The propagation of elastic waves in granular structures composed of a main granular chain, side loaded by several beads or granular chains has been already investigated by several authors. For example, the transmission of an acoustic pulse through a one-dimensional granular chain composed of glued metal beads with grafted stub have been numerically and experimentally investigated in Ref. [64]. The stub is created by placing additional beads grafted on both sides of a bead at the middle of the chain. The authors of this work have studied the effect of different stubs, containing different number of beads and different sizes, on the spectral response of the chain. They have demonstrated the appearance of a dip in the frequency response of the chain due to the excitation of the stub mode. In addition, they have shown that the frequency of this dip can be adjusted by varying the stub mass. This work has been extended to the case of periodic stub grafted to the one-dimensional granular chain made of glued steel particles [65]. The band structure tunability of such system has been demonstrated by the modification of the bead materials (steel, brass, or glass) in the stubs. In addition to these works, the possibility of redirection of nonlinear wave via pulse splitting have been also investigated in other granular structures like curved or y-shaped granular networks [77–80].

In this thesis, we present the first experimental results of the ability to control the conversion from a longitudinal to a coupled transverse-rotational mode in a simple Γ-shaped granular structure. This structure can be the building block of more complex granular networks in which an advanced control of

elastic wave propagation will be achieved by tailoring the mode conversion and the nonlinear propagation.

3.4.1 Principle of conversion from longitudinal to coupled transverse-rotational modes

In a simple one-dimensional granular chain, the longitudinal normal modes are decoupled from the transversal-rotational ones, as presented in chapter 2. In the first chain, we consider only longitudinal interactions between particles while in the second chain only transverse-rotational interactions are taken into account. Thus, the first chain will be denoted as "L-chain", for Longitudinal-chain, which corresponds to the polarization of the wave motion propagating through it. The second chain will be called TR-chain, for coupled Transverse-Rotational modes. The mechanical representation of the structure as a mass-spring lattice is presented in Fig. 3.23(a).

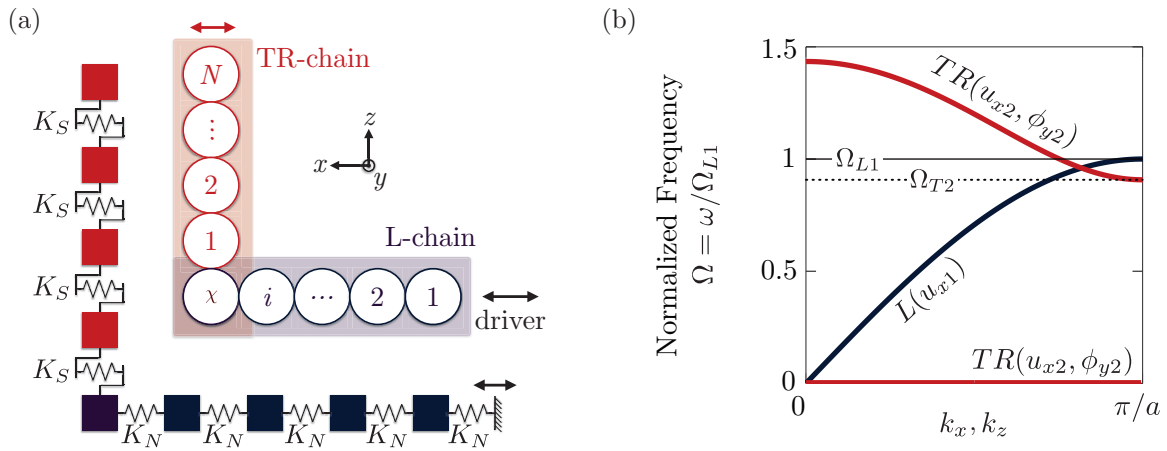

Figure 3.23: (a) Representation of the Γ-shaped granular chain and schematics of the linearized chain by mass-spring lattice. (b) Dispersion curves considering longitudinal motion for the first chain (dark blue) with propagation along the wavenumber k_x and for the second chain (red) considering transversal-rotational motion along the wavenumber k_z. The precompression force is identical in both chains. The frequency is normalized by the longitudinal linear cut-off frequency, Ω_{L1}, of the first chain.

In Fig. 3.23(b), the dispersion curves are presented considering the same precompression force in both chains. The frequency is normalized by the linear cut-off frequency of the longitudinal branch of the first chain, Ω_{L1} given by Eq. (2.25). The linear lower cut-off frequency of the TR branch is $\Omega_{T2} = \omega'_{TR2}/\Omega_{L1}$ where ω'_{TR2} is given in Eq. (2.27). The indices 1 and 2 are referred to the first and the second chain, respectively. It should be noticed that the zero frequency branch, existing in the TR-chain, is excluded from the study.

Considering that the first chain is excited longitudinally, we can expect three different regimes of propagation as a function of the driven frequency. (i) When the driven frequency is under the TR cut-off frequency, namely $\Omega < \Omega_{T2}$, a pure longitudinal wave propagates up to the particle χ. Since the particle χ is also part of the chain 2, a longitudinal motion of this particle for chain 1 corresponds to a transverse

motion for chain 2. However, in this case the mode in the TR-chain is evanescent and finally nothing is transmitted to the end of the second chain. (ii) When $\Omega_{T2} < \Omega < 1$, L and TR modes are supported by both chains (overlapping in frequency of theses branches) leading to the propagation through the entire structure. (iii) When $\Omega > 1$, longitudinal waves are considered as evanescent from the beginning thus there is no wave propagation along chain 1.

3.4.2 Experimental Γ-shaped chain

Let us turn to the realization and the presentation of some preliminary experiments in a Γ-shaped granular structure. The complete chain is composed of 9 stainless steel beads of 15.875 mm diameter, leading to 5 beads for each chain, above a Γ-shaped configuration of cylindrical permanent magnets which are located within a rubber substrate. As in the section 2.3.1, the coupling between the granular structure and the rubber substrate is very weak and in a good approximation is neglected. The external magnetic field is used to create attractive forces between particles of the chain. We assume that the forces into the chain are identical by using the same magnets under both chains. This force is experimentally estimated to be 1 N by using a dynamometer. The chain is driven longitudinally by a piezo-electric transducer *Panametrics* V3052 where a bead is glued on it to ensure that the contact between the driver and the chain is the same than inside the chain. The measurement of a particle velocity is made by a laser vibrometer *Polytec* OFV-503 with a sensitivity of 5 mm/s/V and an averaging is performed during the acquisition. We measure particle velocities at 3 different positions which are presented in Fig 3.24. The first position of measurement is at end of the L-chain, the second and third position are at the end of the TR-chain. The second position allows to measure translational motion of the TR-chain along x-axis while position 3 permits to measure longitudinal motion of the TR-chain in z-direction.

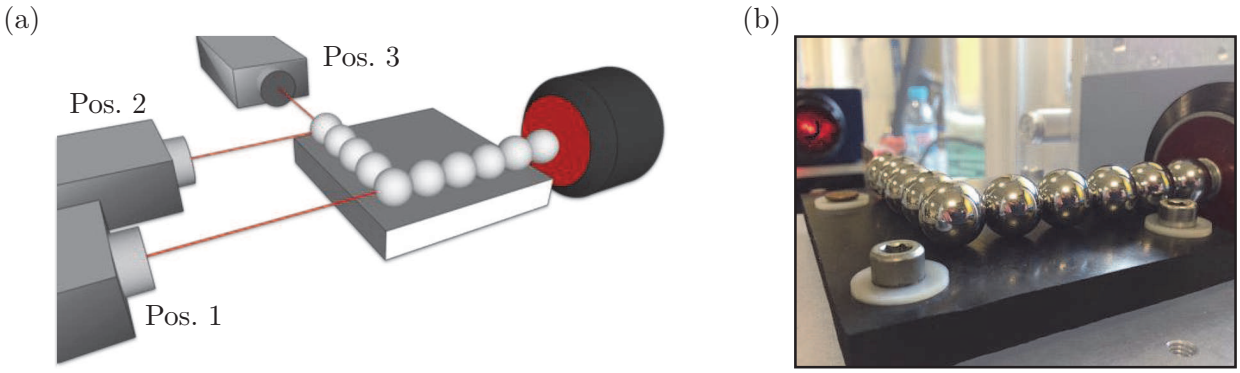

Figure 3.24: Schematics of the experimental Γ-shaped chain and representation of the measurement positions. (b) Photography of the experimental setup.

The excitation signal is a continuous sinus wave and we focus on the study of the steady state of the Γ-shaped granular structure. A linearization process of the entire chain of excitation (generator, amplifier, and transducer with glued bead) is implemented. This method, described in Ref. [133], allows to linearize the signal emitted by the transducer via an active loop which adds to the initial signal harmonic

components with different phases providing the cancelation of the undesired harmonics. Thus, this method ensure a direct control of the driver linearity. It is worth mentioning that our setup, even without this linearization process, is sufficiently linear when the input voltages are smaller than the admissible limit. However, close to this voltage limits harmonics can appear. In order to experimentally implement this linearization method, a second laser vibrometer is used to measure and control the frequency components of the glued bead to the transducer during each measurement. As a result, harmonics are 60 dB smaller than the fundamental frequency corresponding to a level very close to the experimental noise.

From Eqs. (2.25, 2.27), using a precompression force of 1 N, the cutoff frequency of the longitudinal branch is found at 6565 Hz (namely $\Omega_{L1} = 1$) and 5958 Hz for the lower TR branch (namely $\Omega_{T2} = 0.90$). First measurements are made using a sinus at 3 kHz which leads to $\Omega = 0.455 < \Omega_{T2}$. For this frequency, we expect that the longitudinal wave is propagating while the TR wave is evanescent. Fig. 3.25 presents the experimental temporal displacements and the related frequency analysis for each position of measurement described above. The ratio between the driver displacement δ and the static overlap δ_0 is estimated to be $\delta/\delta_0 = 0.009$ and thus we ensure a near-linear dynamical regime of the chain.

The first line in Fig. 3.25, presents the experimental signal of the driver (glued bead to the transducer) when the steady state is achieved. We observe a very clean harmonic signal with only a frequency component at the fundamental frequency. The amplitude of the frequency components is from now on normalized by the maximum of fundamental component of the driving bead. Looking to the measured signal in position 1, corresponding to the longitudinal components at the end of the first chain, we observe that the amplitude of the displacement of the last bead of the L-chain is to close the driver amplitude. We notice also the existence of the second and third harmonics with an amplitude 45 dB smaller than the fundamental. The presence of these harmonic components is associated to the nonlinearity of the system existing even at low amplitude of excitation (near-linear regime). Moreover, the third harmonic amplitude is slightly higher than the second harmonic amplitude which could come from the modal behavior of the chain at this driven frequency.

In the position 2, corresponding to the measurement of the transverse component at the end of the second chain, we see that the measured amplitude is much weaker compared to the other two positions. The experimental signal is noisy because we are close to the experimental noise. The driver frequency is in the lower band gap of the TR branch thus we expect that the TR wave which is excited by particle χ is evanescent. Due to the small length of the second chain (5 beads), the wave is not totally attenuated and this is why it is measured in position 2.

Regarding the longitudinal motion of the second chain, namely position 3 of measurements, we can observe that a wave is present in the longitudinal direction. This longitudinal modes was not expected from the simple first model including only transversal-rotational motion in the second chain but can be explained by a more complex modeling of the chain. A model considering three degrees of freedom (two displacements and one rotation) for each bead motion of the Γ-shaped chain enables to demonstrate that the rotational component is responsible to the couplings of all the motions at the particle χ. From preli-

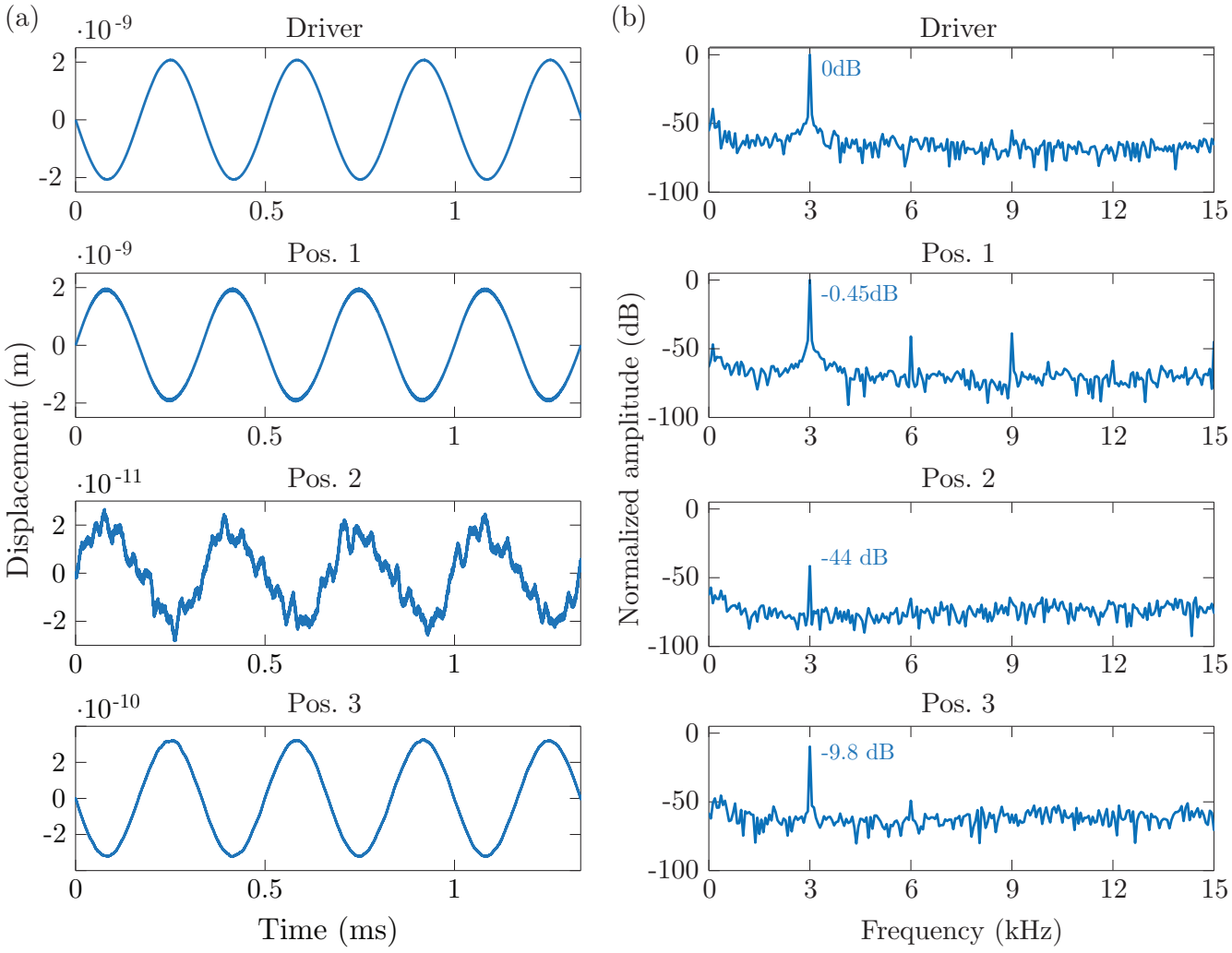

Figure 3.25: Experimental results for a driven frequency at $\Omega = 0.455 < \Omega_{T1}$ in linear regime in (a) temporal and (b) frequency domains.

minary numerical simulations, the presence of longitudinal motion is well capture by this model including 3 degrees of freedom. From this set of experimental results, we observe that L modes are excited in both chains while the TR modes are in the evanescent regime.

We consider now the case where the driving frequency is at 6 kHz, namely $\Omega_{T2} < \Omega = 0.91 < 1$. The experimental results are presented in Fig. 3.26 where the amplitude of excitation is again small and thus the dynamics can be considered near linear, $\delta/\delta_0 = 0.012$. For the signal measured on the driven bead and on position 1, we can observe that a harmonic longitudinal mode is well presented. We can notice the weak presence of the second harmonic in position 1 measurements, as in the previous case. Looking the position 2 measurements (transverse detection) we can notice that the amplitude of the displacement is clearly higher than in the previous case. These results show an evidence of the conversion of mode from longitudinal to transverse-rotational mode in a Γ-shaped chain. In addition the very weak amplitude measured in position 3 (longitudinal motion of the second chain) could highlight a good efficiency in the

mode conversion.

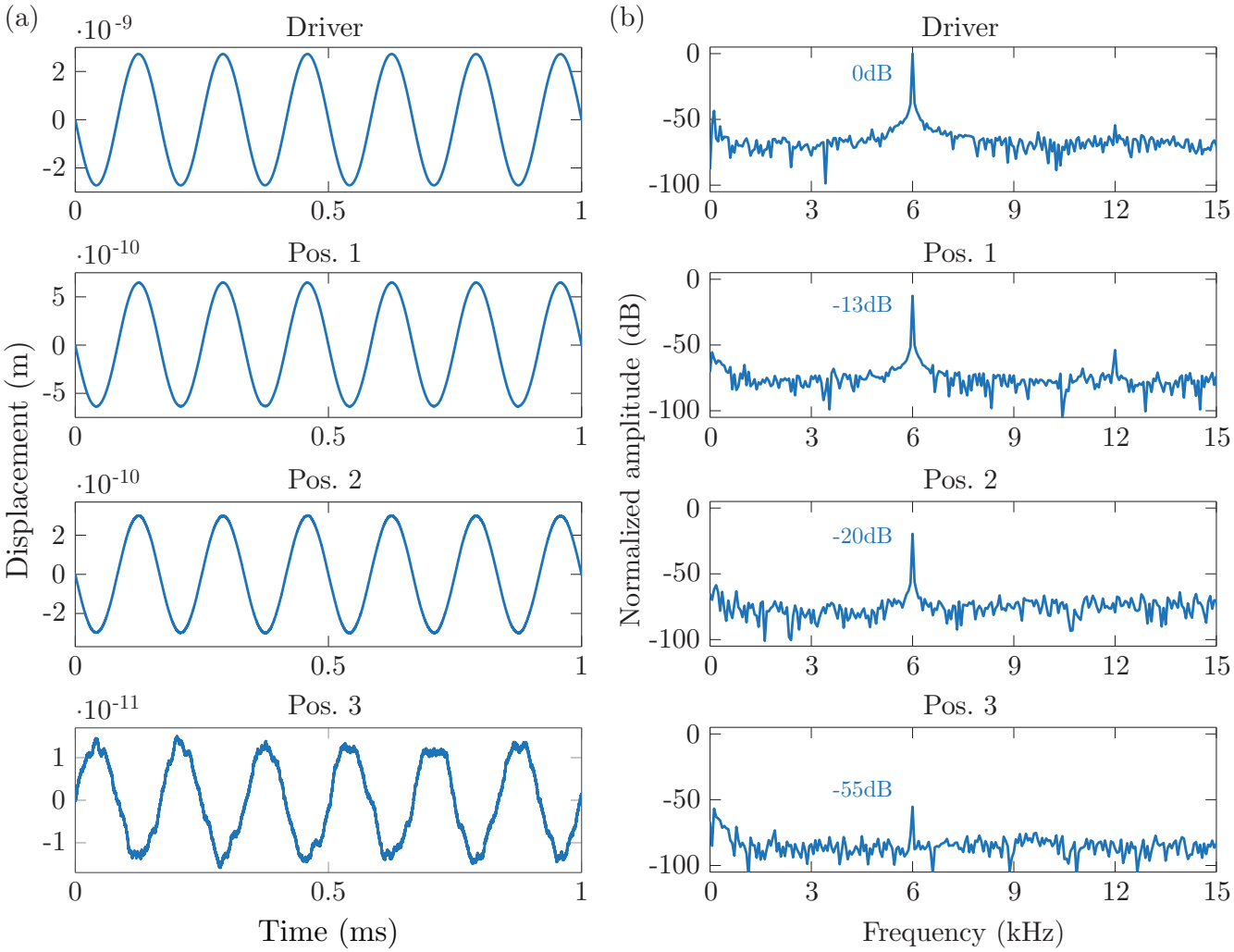

Figure 3.26: Experimental results for a driven frequency at $\Omega_{T2} < \Omega = 0.91 < 1$ and linear amplitude of excitation in (a) temporal and (b) frequency domains.

Let us now study the effect of nonlinear longitudinal wave propagation through the Γ-shaped granular structure. We have presented, in section 3.3, the possibility to generate higher harmonics in our one-dimensional granular chain. Taking advantage of this nonlinear phenomenon, we can tune the wave propagation as a function of the fundamental frequency in the Γ-shaped chain. We consider a driving frequency below the cut-off frequency of the TR-chain, $\Omega < \Omega_{T2}$, having its second harmonic in the frequency overlap of the L and the TR branches, $\Omega_{T2} < 2\Omega < 1$. In this configuration, harmonics are generated in the first chain but only the second harmonic is allowed to propagate through the second chain. This configuration provides a linear filtering of the fundamental wave. Considering the precompression force to be 1 N and the fundamental frequency at 3 kHz, we obtain $\Omega = 0.455 < \Omega_{T2} = 0.90$, which allows the second harmonic to be inside the frequency overlap of the L and TR branches: $\Omega_{T2} = 0.90 < 2\Omega = 0.91 < 1$. Fig. 3.27 depicts the experimental results for the wave propagation under longitudinal excitation with large amplitude $\delta/\delta_0 = 0.32$.

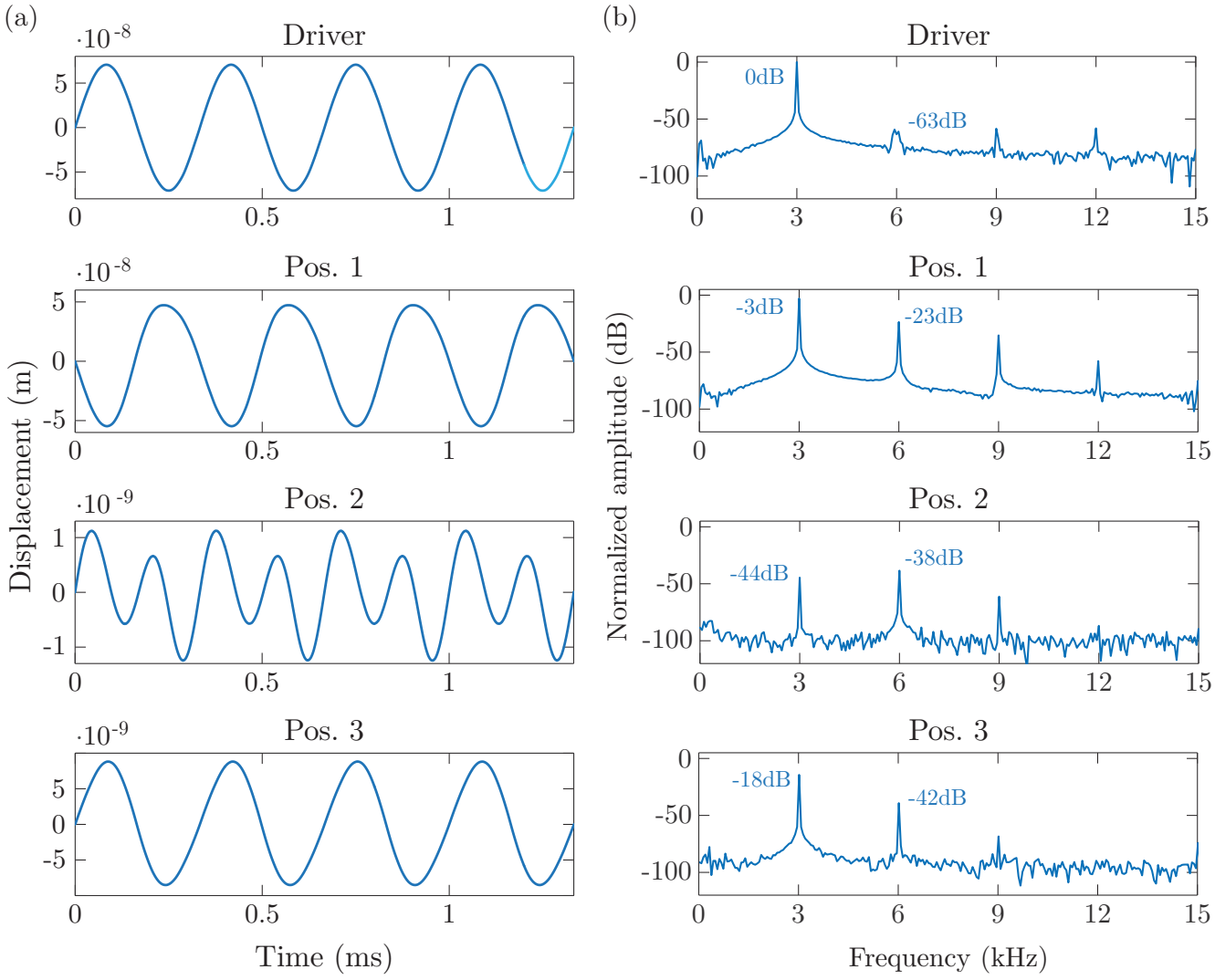

Figure 3.27: Experimental results for a driven frequency at $\Omega = 0.455 < \Omega_{T2}$ and nonlinear amplitude of excitation ($\delta/\delta_0 = 0.32$) in (a) temporal and (b) frequency domains.

Regarding the measured driver displacement in Fig. 3.27, we observe that the second harmonic generated by the driver is 60 dB smaller than the fundamental. Thus we can confirm that the driven bead provides only the fundamental frequency. At the position 1, corresponding to the end of the first chain, we can notice that the harmonics are strongly generated in the first chain. At the position 2, where we are sensitive to transverse displacements of the last particle of the second chain, we can observe that the period of the signal is doubled in comparison with the driver signal which indicates that the second harmonic components is large. Indeed looking to the spectrum, we see that the second harmonic is higher than the fundamental frequency which is expected because the fundamental frequency is not propagating in the TR branch. This ratio between the fundamental and the second harmonic shows the experimental evidence of the linear filtering effect of the fundamental and the mode conversion from longitudinal to coupled transversal/rotational.

In position 3, we are sensitive to longitudinal displacements of the last particle of the second chain. We

can observe that the dominant component is the fundamental and the ratio between the amplitude of the second harmonic and the fundamental is close to the one in position 1.

3.4.3 Summary

In this section, we have presented the experimental realization of a Γ-shaped granular structure by considering the use of external magnetic field induced by identical permanent magnets in a Γ-shape configuration. A toy model has been proposed to explain and understand the experimental results. The experimental results have shown clearly the evidence of mode conversion from longitudinal to coupled transverse-rotational modes along with a linear filtering of frequency due to the geometry of the structure. Experimental results have shown that the modeling of the Γ-shaped has to include the longitudinal motion in the second chain and the transversal-rotational motions in the first chain.

3.5 Conclusion

The complete linear wave propagation in L and TR branches has been experimentally realized for wave packets and harmonic wave signals in a freely standing granular chain. Numerical simulations, using the experimental signal of the driver as a driving boundary, are performed in order to estimate the precompression force and the attenuation in the chain. We found very good agreement between experimental and numerical results for all the frequency studied. Moreover, the numerical simulations involving viscous on-site damping describe correctly, as a first approximation, the attenuation of the waves as a function of the frequency. In addition, the spatio-temporal measurements have highlighted the presence of defects in the granular chain by the observation of unexpected reflected waves inside the chain. These defects are probably a misalignment of particles with the chain axis. The linear study has included the experimental estimation of the group velocity in L and TR branches by following the envelope of the wave packets propagation as a function of different carrier frequencies. Theoretical predictions are in good agreement with the experimental results.

The nonlinear dynamical behavior has been first numerically studied focusing on the second harmonic generation. The well-known spatial beating in amplitude of the second harmonic has been shown by neglecting reflected waves from the boundary and dissipation. Then, dissipation has been added to the numerical model and the effect of reflected waves has been analyzed. The presence of dissipation affects the amplitude of the harmonic but does not modify the spatial effect of the beating, while the presence of reflected waves destroyed totally the beating of the second harmonic. Finally, experimental evidence of the beating phenomenon in a granular chain has been realized by minimizing the presence of reflected waves in the signal analysis. Several driven frequencies have been tested and the harmonic generation has been found in good agreement with analytical and numerical predictions. The amplitude and the positions where the second harmonic is vanishing have been recovered. Regarding the dynamics in the transverse direction, all the performed experiments revealed a linear behavior. This is due to the small amplitude excitation of the used shear transducers. However the potential nonlinear response in the tangential direction could open the way for the observation of novel, nonlinear TR waves in mechanical structures.

Finally, in the last part, the experimental realization of Γ-shaped chain has been presented by taking advantage of properly designed external magnetic field to induce attractive forces between the particles. A first toy modeling of the chain, considering longitudinal motion in the first chain and transverse-rotational motion in the second chain, has been proposed in order to understand the experimental results. The experimental results have shown clearly the evidence of mode conversion from longitudinal to coupled transverse-rotational modes along with a linear filtering of frequency. This mode conversion is induced by the geometry of the structure. Experimental results have shown that the toy model is not sufficient to describe well the dynamics of the Γ-shaped chain. Indeed, the longitudinal motion has to be taken into account in the second chain as well which leads to the modeling of transverse-rotational motion also in the first chain. Preliminary numerical results considering three degrees of freedom (two displacements and one rotation) for each chain show a quantitatively good agreement for the estimation of the longitudinal motion

in the second chain and also show the possibility of mode conversion. The combination of the non-contact tunability of the interparticle forces and strong nonlinear behavior allows the design of two-dimensional metamaterials and networks for an advanced control elastic wave propagation.

General conclusion

In this thesis, we have reported on the design and study of elastic wave propagation in magneto-granular phononic structures. These are composed of linear chains of spherical steel beads inside a properly designed magnetic field induced by permanent magnets. The external magnetic field offers not only a great advantage of straightforward construction but also a non-contact tunability via its magnetic field strength. The importance of the rotational degrees of freedom in the dynamical description of the bead motion in granular structures has been discussed. Theoretical studies from several authors, have predicted the existence of coupled transversal-rotational modes granular media, but very few have experimentally confirmed their existence. This work has been devoted to the linear and nonlinear wave propagation through granular structures by analytical modeling, numerical simulations together with experimental measurements including the presence of rotation in bead motion.

After a reminder of useful notions for the acoustic wave propagation in granular media, the theoretical description of the three-dimensional dynamics of the granular chain has been proposed by considering a linear model. The contact interactions between adjacent particles are modeled by three springs (for the normal, shear, and torsional interactions) obeying the Hertz-Mindlin theory. The model is considering all the six degrees of freedom, i.e. three translations and three rotations of bead motions. By the application of different coupling parameters between beads and the substrate our system supports transversal/rotational propagation modes, zero group velocity (ZGV) modes and accidental degeneracies in the dispersion curves. Experiments have clearly revealed the existence of coupled transversal-rotational modes in a granular chain that moreover can be tuned by the external magnetic field. When the granular chain is mechanically coupled with the rigid substrate, experimental results are in good agreement with the predicted allowed and forbidden bands of propagation by fitting only one parameter, the shear stiffness between the spheres and the substrate. It has been shown that the disagreement between the shear stiffness predicted by the Hertz theory and the one experimentally estimated is originating from the rough surface of the substrate. Particular surface topographies can lead to a programmable control of the stiffnesses between the elements of the setup and thus to an engineered dispersion relation. In addition to the coupled transverse-rotational modes, an experimental evidence of a ZGV point at finite wavelength has been shown.

Then, spatio-temporal measurements have been performed by measuring the velocity each particle of the chain and have been successfully compared to numerical simulations. The numerical analysis has provided a better estimation of the precompression force and of the wave attenuation along the propagation.

The spatio-temporal measurements have also pointed out the presence of defects into the chain probably due to misalignment of particles and have highlighted that the precompression in the experimental setup is sensitive to the initial position and alignment of the beads.

The low value of the static load endows the system with a potential strong nonlinear response. Thus, nonlinear dynamical behavior has been studied. In particular, the second harmonic generation has been first numerically simulated in a chain without reflected waves and dissipation, and secondly in a more realistic case (considering both the finiteness of the structure and the losses) focusing on the spatial beating in the amplitude of the second harmonic. Finally, experimental results have revealed for the first time the existence of such beating phenomenon in a granular chain by minimizing the presence of reflected waves in the signal analysis. Several driven frequencies have been tested and the beating in amplitude of the harmonic generation has been found in good agreement with analytical and numerical predictions.

Finally, the wave propagation in a granular structure deviating from a simple one-dimensional granular chain has been studied. The proposed granular structure is composed of two simple granular chains forming a "Γ"-shaped chain. A simple model considering longitudinal motion in the first chain and transverse-rotational motions in the second has been proposed as a first approach to understand the experimental results. The experimental results have shown the evidence of mode conversion from longitudinal to coupled transverse-rotational modes along with a linear filtering of frequency. In a simple granular chain these modes are decoupled, however here the ability of mode conversion is induced by the geometry of the structure. The simple model fails to describe the entire chain dynamics. Thus, first numerical simulations have been tested considering three degrees of freedom (two displacements and one rotation) for each chain and a better agreement was found for the estimation of the final mode conversion as well as magnitude of the longitudinal motion in the second chain.

Different perspectives to this work could be considered. From the modeling point of view, it would be interesting to add a possible disorder in the alignment of the particles in order to analyze this effect on the elastic wave propagation. The addition of bending rigidity between the granular chain and the substrate could enable a better fitting of the experimental dispersion curve at low frequencies. Finally, the complete modeling of the nonlinear interactions for the transverse displacement could lead to novel nonlinear TR waves in mechanical structures. In addition, the modeling of dissipation is a key point in granular assemblies. In this work, the dissipation has been qualitatively modeled via a viscous on-site damping. The comparison between numerical simulations and experimental results has shown a good agreement for the attenuation along the wave propagation. However, the implementation of nonlinear viscoelastic model for the dissipation could provide better results, especially when considering the nonlinear regime of the wave propagation.

From the experimental point of view, it would be interesting to investigate in more details the presence of zero group velocity mode at the middle of the first Brillouin's zone for the case of a granular chain coupled with a rigid substrate. Moreover, the modification of the substrate roughness could lead to the

tunability of the dispersion curve and interesting phenomena could appears such as the predicted accidental degeneracies. In order to improve the detection of coupled transversal-rotational modes and the experimental dispersion curve, the measurement of the rotational component is needed. Thus, accelerometer or rotational laser vibrometer which are sensitive to angular displacement can be used to measure the rotational motion. The main advantage of the laser vibrometer is the contactless measurement.

Magneto-granular structures offer a perfect experimental testbed for the study of novel wave phenomena. Taking advantage of the external magnetic field to induce attractive forces between the particles, different one-dimensional and two-dimensional structures can be easily built such as curved chain, zigzag, armchair, or honeycomb structures. In addition, placing the permanent magnets on displacement stages one could control the distance between the granular structures and the magnets leading to modification of the force in the chain and thus adding tunability into the dynamical response of the granular structure. Finally, rotational motion induced by non-central forces and nonlinear contact laws between the beads enrich the dynamic response of these mechanical structures.

To conclude, all the above features of the magneto-granular structures, namely structural engineering of the dispersion relation, tunability by external magnetic fields and the inherent potential strong response open the way for novel wave phenomena and an advanced control of elastic wave propagation.

Appendix A

Additional experiment and simulations of magnetic field

This appendix presents more details and results on magnetic simulation in 2 and 3 dimensions, comparison between analytics and finite element methods.

One magnet - 2D model

The non-uniform magnetic field created by a permanent magnet has been analytically presented by Yonnet in Ref. [119] in two and three dimensions. In this section we consider the 2D configuration. The rectangular magnet has a height $2L_m = 10$ mm, width $2l_m = 4$ mm and an infinite dimension along z-axis. The analytical expressions of the magnetic field components in air $B_0(x, y)$ for such a magnet are:

$$B_{0x} = \frac{-\sigma^*}{4\pi\mu_0} \sum_{i=0,1} \sum_{j=0,1} (-1)^{i+j} \ln\left\{[l_m + (-1)^i x]^2 + [L_m + (-1)^j (y + L_m)]^2\right\}, \tag{A.1a}$$

$$B_{0y} = \frac{-\sigma^*}{4\pi\mu_0} \sum_{i=0,1} \sum_{j=0,1} (-1)^{i+j} 2\text{atan}\left(\frac{l_m + (-1)^i x}{L_m + (-1)^j (y + L_m)}\right), \tag{A.1b}$$

where $\sigma^* = B_r \mu_0 \mu_{air}$ is the surface charge density of the magnet with the remanent magnetization B_r, $\mu_0 = 4\pi 10^{-7}$ is the vacuum permeability and $\mu_{air} = 1$ is the relative permeability of the air. Inside the magnet, the field is calculated with same expressions as Eqs. (A.1) considering now $\sigma^* = B_r \mu_0 \mu_m$ where $\mu_m = 1.05$ is the relative permeability of a permanent neodymium magnet. Then, the density of magnetic field is given by $B_0 = \sqrt{B_{0x}^2 + B_{0y}^2}$. Fig. A.1 shows analytical results from Eqs. (A.1) for each component and the density of the magnetic field.

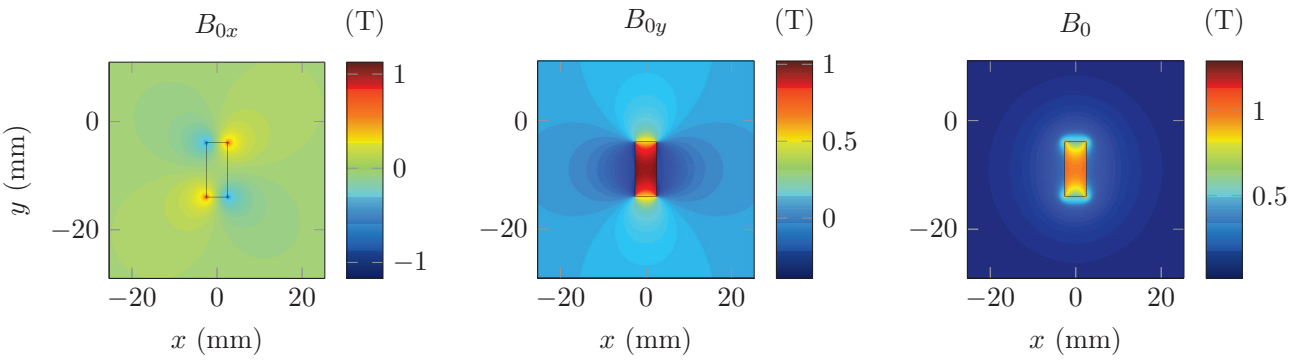

Figure A.1: Analytical magnetic field of one permanent magnet from Eq. (A.1) for x and y components, left and center panels respectively, and the density of magnetic field (right panel).

We turn now to finite element simulations. The magnetic flux lines created by a permanent magnet are circular and thus we chose a surrounding box of air with circular shape in order to minimize the boundary problem which can appear with a square box. Finally, the studied domain consists of a disk with air characteristics ($\mu_{air} = 1$), and a rectangle corresponding to the permanent magnet with $\mu_m = 1.05$ and $B_r = 1.32$ T. The direction of the polarization has to be defined. In our case the polarization is along y-axis. Moreover, a surrounding domain with *infinite elements* is created leading to an unbounded domain, mimicking a free space case, see Fig. A.2. The mesh is built with triangles, for the study domain, and with quadrangle, in the *infinite domain*. The magnetic field of each component and the total density is presented in Fig. A.3.

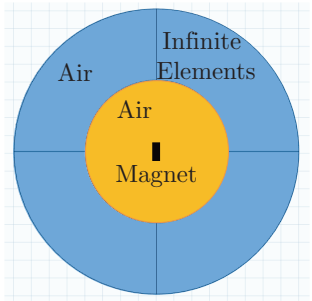

Figure A.2: Simulated geometry in FEM.

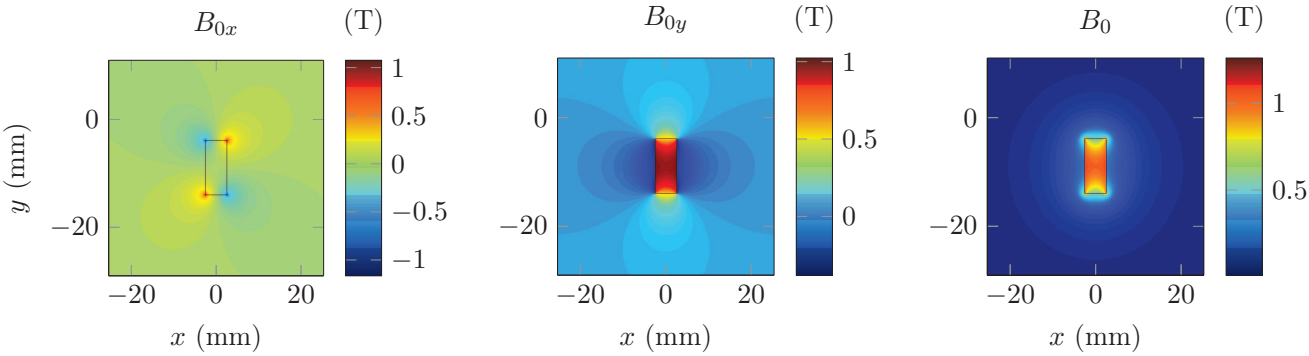

Figure A.3: 2D finite element simulation of the magnetic field of one permanent magnet for the x and y components, left and center panels respectively, and the density of magnetic field (right panel).

In order to compare analytical and numerical results, we define a relative error as

$$Error \quad = \quad 100\frac{(B_a - B_n)}{B_n}, \tag{A.2}$$

where the indexes a and n correspond to analytical and numerical results respectively. The error for each

component and the total density of magnetic are shown in Fig. A.4.

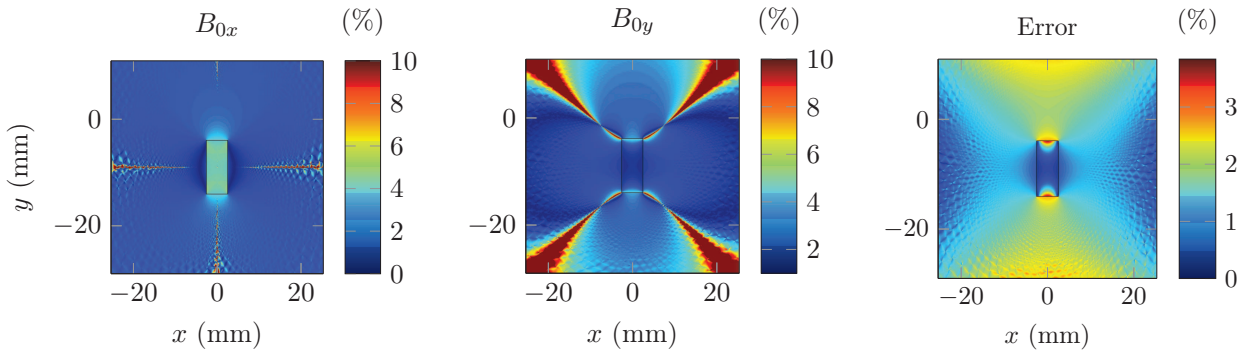

Figure A.4: Error between the analytical model and the finite element simulation magnetic field for one magnet.

The error tends to $+\infty$ when magnetic fields B_{0x} and B_{0y} of the reference tend to 0. Analytics and numerics fields tend to 0 but are never equal to 0 due to numerical errors when interpolations from free mesh (in numerics) to a grid mesh in order to compare the results. We can notice that the global error on the magnetic field density B_0 is less than 4% and as conclusion, the 2D simulated magnetic field from a permanent magnet is well numerically simulated. The next step is to add into this non-uniform magnetic field a sensitive material to magnetism and see the perturbation of the magnetic field by this particle.

One bead - one magnet: calculation of the magnetic force

If we add now a ferromagnetic bead (sensitive to magnetic field) into the previous field. The bead becomes magnetized and the new magnetic field can be see as the initial field $B_0(x, y)$ with a perturbation due to the added particle. This new magnetic field, considering this perturbation, can be expressed outside of the bead for 2D configuration as:

$$B_{1x_{out}} = B_0\left(1 + R^2\frac{\mu_b - 1}{\mu_b + 1}\frac{(x - x_b)(y - y_b)}{((x - x_b)^2(y - y_b)^2)^2}\right), \tag{A.3a}$$

$$B_{1y_{out}} = B_0\left(1 + R^2\frac{\mu_b - 1}{\mu_b + 1}\frac{(y - y_b)^2 - (x - x_b)^2}{((x - x_b)^2(y - y_b)^2)^2}\right), \tag{A.3b}$$

where $\mu_b = 700$ is the relative permeability of the bead (stainless steel material), x_b and y_b are the center coordinates of the bead of radius R. The magnetic field inside the bead is defined as:

$$B_{1x,y_{in}} = \frac{2\mu_b}{\mu_b + 1}B_0. \tag{A.4}$$

Finally, the total density of magnetic field is given by $B_1 = \sqrt{B_{1x}^2 + B_{1y}^2}$. The Fig. A.5 presents analytical and simulated results for the case of ferromagnetic bead inside a magnetic field created by a permanent magnet in 2D configuration. From Fig A.5 (right panel), the error into the bead is very small (less than 2%), the error outside the bead is larger but still reasonable. We are interested in the field inside the

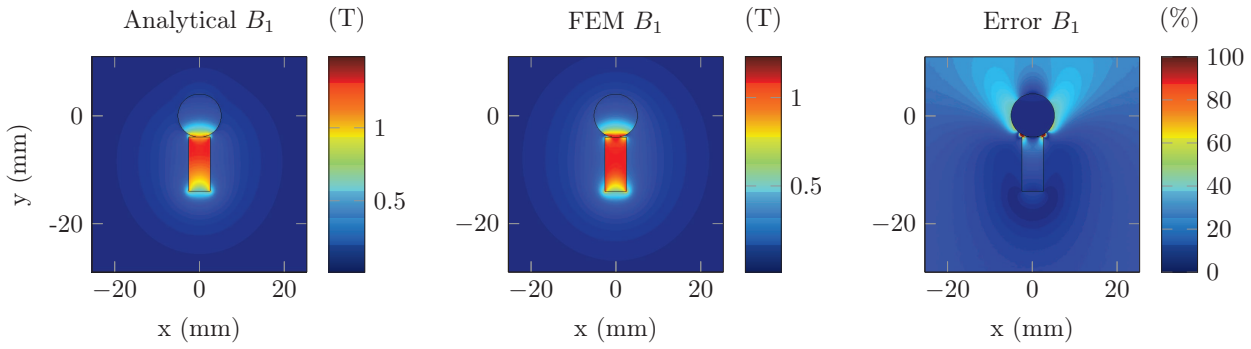

Figure A.5: 2D Magnetic field density created by permanent and perturbed by a ferromagnetic bead analytically solved (left), with finite element simulation (center), and the relative error (right).

bead thus we can say that simulation with finite element method describes well the magnetic field of a permanent magnet. The numerical simulation allow us to determine force acting by the magnet on the bead. In order to determine this attractive force, let us consider a bead (material 1) on the top of a permanent magnet surrounding by air (material 2). The reaction force from the magnet on the bead will be denoted by $\mathbf{r_m}$. The force created by the magnetic field on the bead have to be solved at the boundary bead/air and into the volume of the bead. From Cauchy's equation considering a stationary case (no acceleration), on the boundary bead/air the equations apply

$$\mathbf{n_1}\,(T_2 - T_1) + \mathbf{r_m} = 0, \tag{A.5}$$

where T_1 and T_2 respectively represent the stress tensor for the material 1 and material 2, $\mathbf{n_1}$ is the normal pointing out from the domain containing material 1. Equations for the equilibrium of forces are,

$$\nabla \cdot T_1 + \mathbf{f_{ext}} = 0, \tag{A.6}$$

where $\mathbf{f_{ext}}$ is an external volume force. To obtain the total force $\mathbf{F}$ on the bead, equations Eq. (A.5) and Eq. (A.6) have to be integrated over the entire domain and boundary,

$$\int_{\Omega_1} (\nabla \cdot T_1 + \mathbf{f_{ext}})\, dV + \oint_{\partial\Omega_1} (\mathbf{n_1}\,(T_2 - T_1) + \mathbf{r_m})\, dS = 0.$$

Considering the divergence theorem,

$$\int_{\Omega_1} \nabla \cdot T_1 dV - \oint_{\partial\Omega_1} \mathbf{n_1} T_1 dS = 0, \tag{A.7}$$

the external force can be expressed as,

$$\mathbf{F_{ext}} = \int_{\Omega_1} \mathbf{f_{ext}} dV + \oint_{\partial\Omega_1} \mathbf{r_m} dS = 0. \tag{A.8}$$

Finally keeping the bead in a stationary state ($\mathbf{F_{ext}} + \mathbf{F} = 0$), the total force is a boundary integral of the stress tensor on the outside of the bead and is expressed as,

$$\mathbf{F} = \oint_{\partial\Omega_1} \mathbf{n_1} T_2 dS = 0. \tag{A.9}$$

If we consider a bead composed of stainless steel 440C material with a radius of $R = 4$ mm, Young's modulus $E = 200$ GPa, Poisson's ratio $\nu = 0.3$ and a cylindrical permanent magnet of dimension 4 mm diameter and 10 mm height with a remanent magnetization equal to 1.32 T, the numerical simulation of the force Eq. (A.9) give us $F \approx 4.7$ N by 3D simulation. It should be noticed that parametric analysis are performed on the mesh to ensure the convergence of the results. Now experimentally, as said previously, the force induced by the external magnetic field can be estimated by using a dynamometer. Assuming that the precompression force between bead and magnet is equal to the measured pulling force required to separate two adjacent particles. We obtain $F \approx 4.5$ N which is in a very good agreement with our simulated estimation. One more time, the 2D simulation over-estimate results and gives $F = 6$ N. We can conclude that our numerical simulation is correct.

Magnetic field measurement - plane (x, y)

As additional measurement, we present in Fig. A.6 the experimental magnetic field measured for the plane (x, y) above a line array of 5 permanents magnets.

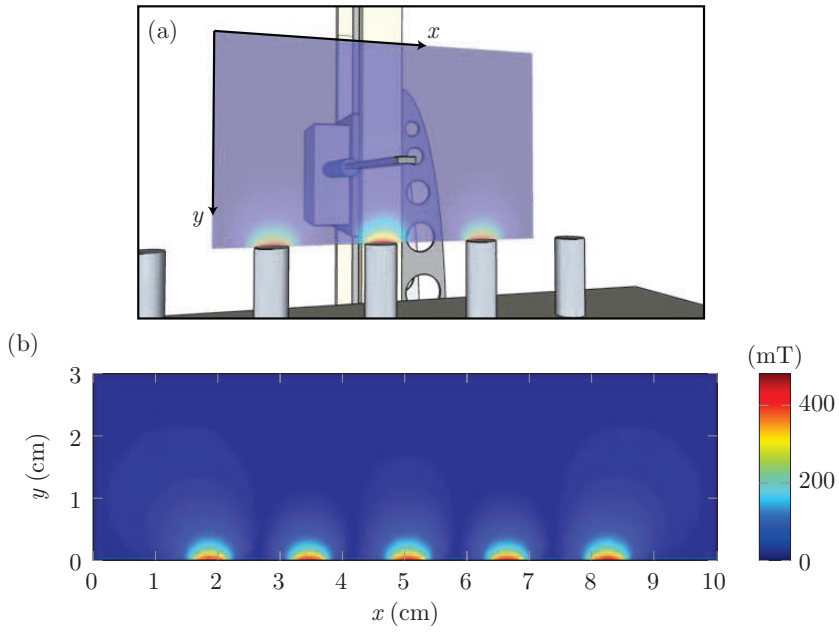

Figure A.6: (a) Experimental setup to measure the magnetic field created by a line array of magnets. The experimental magnetic field measured by the Gauss-meter is superimposed. (b) Experimental magnetic field created by 5 magnets.

Appendix B

Experimental dispersion curves for a linear granular chain coupled to a substrate

To complete the linear study of the chain coupled to a rigid substrate (Fig. B.1), we have performed preliminary experimental dispersion curves.

Figure B.1: Photography of the granular chain coupled to a rigid substrate.

The method, presented in the section 2.4.3, is realized in order to obtain this curves. The chain is now composed of 26 particles. Fig. B.2 presents the experimental dispersion for the modes sagittally polarized (u_x, u_y, ϕ_z). Theoretical dispersion curves are superimposed fitting the precompression force to $F_0 = 2.1$ N (K_N), $F_0' = 1.8$ N (K_S, K_T), $F = 10$ N ($\tilde{K}_N$, $\tilde{K}_T$), $F' = 0.1$ N ($\tilde{K}_S$). Fitted forces F_0 are close to the experimentally measured forces using dynamometer

The theoretical curves depict the existence of translational motion for each component in a color scale. On the panel Fig. B.2(a), a color scale from white (absence) to red (pure existence) of u_x component is represented and on the panel Fig. B.2(b) the color scale displays the absence (white) to pure existence (magenta) of u_y component. The branches containing u_x motion are well detected by our measurement, we can clearly see the forbidden gap at low frequency range and the upper limit is also well describe. However, we don't measure the predicted gap between 4.4 kHz and 5 kHz.

On the panel Fig. B.2(b), the existence of the u_y component is measured and theoretically reported. Experimentally, a low branch is present containing a zero group velocity (ZGV) mode at $k \approx 0.65\pi/a$ while theoretically it appears at $k \approx 0.44\pi/a$. A gap is also observed between the two lower branches

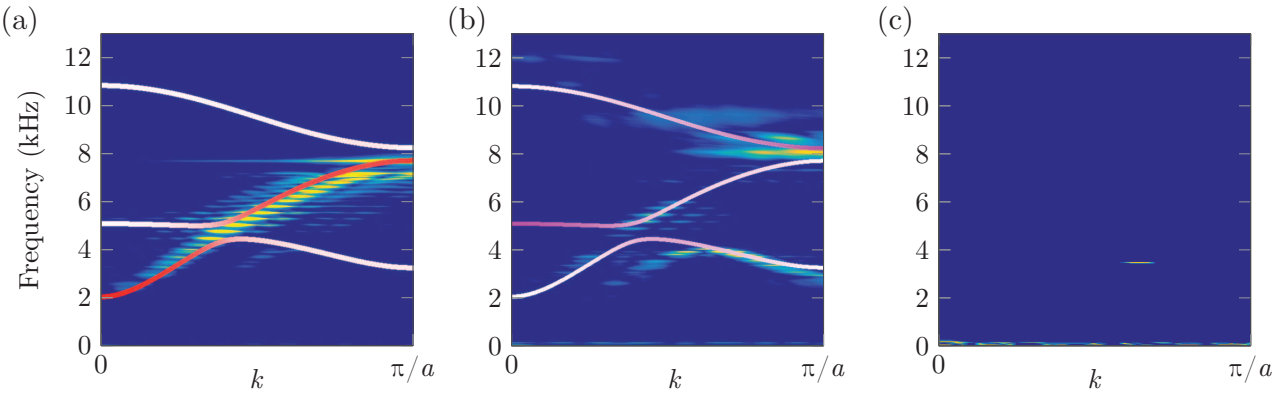

Figure B.2: Experimental dispersion curves for a chain of 26 beads for (a) excitation along x-axis and measurement in Pos. 1 and (b) excitation along y-axis and measurement in Pos. 2. The theoretical existence of translational motion is superimposed on each panel in color scale. (a) Red color means existence of translational motion u_x, (b) Magenta for translational motion u_y component. (c) Detection of the ZGV mode from u_y measurement. Theoretical dispersion curves are fitted using $F_0 = 2.1$ N (K_N), $F_0' = 1.8$ N (K_S, K_T), $F' = 10$ N ($\tilde{K}_N$, $\tilde{K}_T$), $F = 0.1$ N ($\tilde{K}_S$).

form 4000 Hz to 4600 Hz whereas the theoretical gap is from 4430 Hz to 5050 Hz. The second branch is almost flat from $k = 0$ to $k \approx 0.44\pi/a$ with strong presence of translational u_y motion. Experimentally, the measurement of this part of the branch is not achieved but we detect the second part when the branch slope is increasing up to the absence of translational motion. The highest branch is approximately measured, the amplitude increase when k increase corresponding to more and more translational motion.

To ensure the presence of ZGV mode, post-processing delaying the starting point of the bi-dimensional FT is realized. Indeed, such mode has a very slow velocity leading to a delayed arrival time in comparison with the other modes. Thus looking after a certain time in the received signal it should appears only this modes. The results of the ZGV detection is presented on panel Fig. B.2(c). As we can see, only one point is detected at $k \approx 0.65\pi/a$ and $f = 4020$ Hz validating the presence of ZGV mode in our chain. We can also observe some amplitude around $f = 0$ Hz coming from artifact noise during the post-processing.

Finally, the total experimental dispersion curves for both plane is presented in Fig. B.3. The panel (a) represents on the same figure the measurement along x and y from Fig. B.2(a-b) whereas the panel Fig. B.3(b) presents the results in the horizontal plane.

For the modes polarized in horizontal plane, once again the modes detected are only on the lower part of the highest branch. The lowest branch is not be detected by our setup as well as the middle branch, which is containing very small translational motion. It should be noted that at $k = 0$ and $f = 11.4$ kHz the presence of a localized mode is detected and not predicted by the model. A localized mode seems to be present also on the sagittal plane at $f = 7.9$ kHz. Such localized mode could be analytically predicted by taking into account the finite size of the system (boundary conditions). Localized mode in a linear chain considering boundary conditions for transversal and rotational degrees of freedom including bending has been already study in [62].

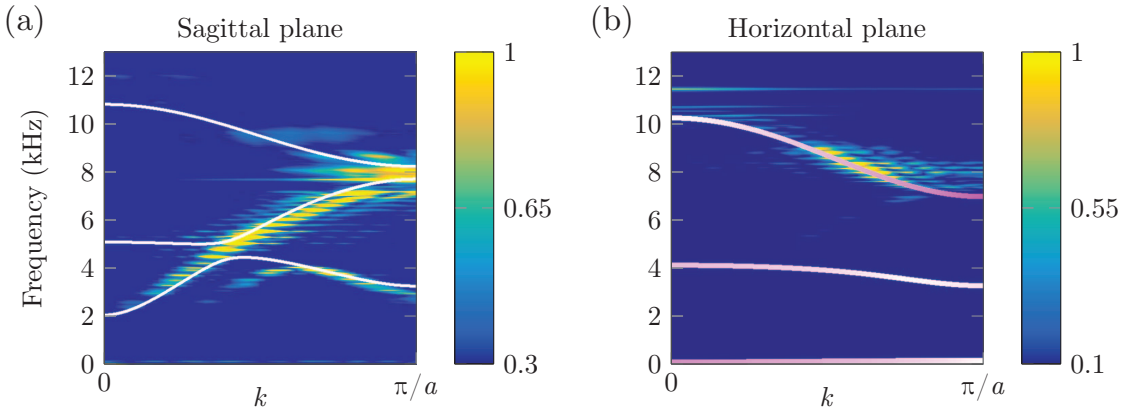

Figure B.3: Experimental dispersion curves for a chain of 26 beads for modes polarized in (a) sagittal and (b) horizontal planes. The theoretical existence of translational motion u_z is superimposed on panel (b) in color scale (white to magenta). Theoretical dispersion curves are plotted using $F_0 = 2.1$ N (K_N), $F_0' = 1.8$ N (K_S, K_T), $F = 10$ N ($\tilde{K}_N$, $\tilde{K}_T$), $F = 0.1$ N ($\tilde{K}_S$).

To conclude on this preliminary results, we are able to detect some part of the predicted branches. A ZGV point at a finite wavelength is clearly present in our setup. Modeling the chain including boundary limits could enable the prediction of localized modes and adding bending rigidity could improve the comparison between experimental and theoretical results.

Bibliography

[1] P. A. Deymier. *Acoustic Metamaterials and Phononic Crystals.* Springer Series in Solid-State Sciences. Springer London, Limited, 2013.

[2] K. Bertoldi and M. C. Boyce. Mechanically triggered transformations of phononic band gaps in periodic elastomeric structures. *Phys. Rev. B*, 77(5):052105–4, February 2008.

[3] J.-Y. Yeh. Control analysis of the tunable phononic crystal with electrorheological material. *Physica B: Condensed Matter*, 400(1-2):137–144, November 2007.

[4] K. L. Jim, C. W. Leung, S. T. Lau, S. H. Choy, and H. L. W. Chan. Thermal tuning of phononic bandstructure in ferroelectric ceramic/epoxy phononic crystal. *Appl. Phys. Lett.*, 94(19):193501–4, May 2009.

[5] J. F. Robillard, O. B. Matar, J. O. Vasseur, P. A. Deymier, M. Stippinger, A. C. Hladky-Hennion, Y. Pennec, and B. Djafari-Rouhani. Tunable magnetoelastic phononic crystals. *Appl. Phys. Lett.*, 95(1):124104, September 2009.

[6] E. Cosserat and F. Cosserat. Theorie des corps dédormables. Herman et Fils, Paris, 1909.

[7] A. Merkel, V. Tournat, and V. Gusev. Experimental evidence of rotational elastic waves in granular phononic crystals. *Phys. Rev. Lett.*, 107(22):225502, 2011.

[8] M. Hiraiwa, M. Abi Ghanem, S. P. Wallen, A. Khanolkar, A. A. Maznev, and N. Boechler. Complex Contact-Based Dynamics of Microsphere Monolayers Revealed by Resonant Attenuation of Surface Acoustic Waves. *Phys. Rev. Lett.*, 116(1):198001, May 2016.

[9] S. P. Wallen, A. A. Maznev, and N. Boechler. Dynamics of a monolayer of microspheres on an elastic substrate. *Phys. Rev. B*, 92(17):174303–9, November 2015.

[10] J. Cabaret, P. Béquin, G. Theocharis, V. Andreev, V. E. Gusev, and V. Tournat. Nonlinear Hysteretic Torsional Waves. *Phys. Rev. Lett.*, 115(5), 2015.

[11] V. F. Nesterenko. *Dynamics of Heterogeneous Materials.* Springer Science, New York, 2001.

[12] V. F. Nesterenko. Propagation of nonlinear compression pulses in granular media. *Journal of Applied Mechanics and Technical Physics*, 1983.

[13] C. Coste, E. Falcon, and S. Fauve. Solitary waves in a chain of beads under Hertz contact. *Phys. Rev. E*, 56(5):6104–6117, November 1997.

[14] E. B. Herbold, J. Kim, V. F. Nesterenko, S. Y. Wang, and C. Daraio. Pulse propagation in a linear and nonlinear diatomic periodic chain: effects of acoustic frequency band-gap. *Acta Mechanica*, 205(1-4):85–103, April 2009.

[15] A.-C. Hladky-Hennion and M. d. Billy. Experimental validation of band gaps and localization in a one-dimensional diatomic phononic crystal. *The Journal of the Acoustical Society of America*, 122(5):2594–7, 2007.

[16] N. Boechler, G. Theocharis, S. Job, P. G. Kevrekidis, M. A. Porter, and C. Daraio. Discrete Breathers in One-Dimensional Diatomic Granular Crystals. *Phys. Rev. Lett.*, 104:244302, June 2010.

[17] S. Job, F. Santibanez, F. Tapia, and F. Melo. Wave localization in strongly nonlinear Hertzian chains with mass defect. *Phys. Rev. E*, 80(2):025602–4, August 2009.

[18] C. Daraio, V. F. Nesterenko, E. B. Herbold, and S. Jin. Energy Trapping and Shock Disintegration in a Composite Granular Medium. *Phys. Rev. Lett.*, 96(5):058002–4, February 2006.

[19] J. Hong. Universal Power-Law Decay of the Impulse Energy in Granular Protectors. *Phys. Rev. Lett.*, 94(10):108001–4, March 2005.

[20] R. Doney and S. Sen. Decorated, Tapered, and Highly Nonlinear Granular Chain. *Phys. Rev. Lett.*, 97(15):155502–4, October 2006.

[21] A. Spadoni and C. Daraio. Generation and control of sound bullets with a nonlinear acoustic lens. *Proceedings of the National Academy of Sciences*, 107(16):7230–7234, April 2010.

[22] N. Boechler, G. Theocharis, and C. Daraio. Bifurcation-based acoustic switching and rectification. *Nature Materials*, 10(8):1–4, July 2011.

[23] T. Devaux, V. Tournat, O. Richoux, and V. Pagneux. Asymmetric Acoustic Propagation of Wave Packets Via the Self-Demodulation Effect. *Phys. Rev. Lett.*, 115(23):234301–5, December 2015.

[24] F. Allein, V. Tournat, V. E. Gusev, and G. Theocharis. Tunable magneto-granular phononic crystals. *Appl. Phys. Lett.*, 108(16):161903, April 2016.

[25] F. Allein, V. Tournat, V. E. Gusev, and G. Theocharis. Transversal–rotational and zero group velocity modes in tunable magneto-granular phononic crystals. *Extreme Mechanics Letters*, 12:65–70, April 2017.

[26] A. Lardeau, J.-P. Groby, and V. Romero-García. Broadband Transmission Loss Using the Overlap of Resonances in 3D Sonic Crystals. *Crystals*, 6(5):51–12, May 2016.

[27] M. S. Kushwaha, P. Halevi, L. Dobrzynski, and B. Djafari-Rouhani. Acoustic band structure of periodic elastic composites. *Phys. Rev. Lett.*, 71(13):2022–2025, September 1993.

[28] M. Sigalas and E. N. Economou. Band structure of elastic waves in two dimensional systems. *Solid state communications*, 86(3):141–143, 1993.

[29] E. N. Economou and M. Sigalas. Stop bands for elastic waves in periodic composite materials. *The Journal of the Acoustical Society of America*, 95(4):1734–1740, April 1994.

[30] R. Martinez-Sala, J. Sancho, J. V. Sánchez, V. Gómez, J. Llinares, and F. Meseguer. Sound attenuation by sculpture. *Nature*, 378(6554):241–241, 1995.

[31] F. R. Montero de Espinosa, E. Jimenez, and M. Torres. Ultrasonic Band Gap in a Periodic Two-Dimensional Composite. *Phys. Rev. Lett.*, 80(6):1208–1211, February 1998.

[32] J. V. Sánchez-Pérez, D. Caballero, R. Martinez-Sala, C. Rubio, J. Sánchez-Dehesa, F. Meseguer, J. Llinares, and F. Gálvez. Sound Attenuation by a Two-Dimensional Array of Rigid Cylinders. *Phys. Rev. Lett.*, 80(24):5325–5328, June 1998.

[33] J. O. Vasseur, P. A. Deymier, G. Frantziskonis, G. Hong, B. Djafari-Rouhani, and L. Dobrzynski. Experimental evidence for the existence of absolute acoustic band gaps in two-dimensional periodic composite media. *J. Phys.: Condens. Matter*, 10(2):6051–6064, July 1998.

[34] A. Sukhovich, L. Jing, and J. H. Page. Negative refraction and focusing of ultrasound in two-dimensional phononic crystals. *Phys. Rev. B*, 77(1):014301–9, January 2008.

[35] S. Yang, J. H. Page, Z. Liu, M. L. Cowan, C. T. Chan, and P. Sheng. Focusing of Sound in a 3D Phononic Crystal. *Phys. Rev. Lett.*, 93(2):024301–4, July 2004.

[36] D. Torrent and J. Sánchez-Dehesa. Anisotropic mass density by two-dimensional acoustic metamaterials. *New Journal of Physics*, 10(2):023004–11, February 2008.

[37] C. Faure, O. Richoux, S. Félix, and V. Pagneux. Experiments on metasurface carpet cloaking for audible acoustics. *Appl. Phys. Lett.*, 108(6):064103–5, February 2016.

[38] H. Hertz. On the Contact of Rigid Elastic Solids. *J. Reine Angew. Math.*, 92, 1882.

[39] R. Lifshitz and M. C. Cross. Nonlinear dynamics of nanomechanical and micromechanical resonators. *Review of nonlinear dynamics and ...*, 2008.

[40] Y. Forterre and O. Pouliquen. Flows of Dense Granular Media. *Annu. Rev. Fluid Mech.*, 40(1):1–24, January 2008.

[41] H. J. Herrmann and S. Luding. Modeling granular media on the computer. *Continuum Mechanics and Thermodynamics*, 10(4):189–231, 1998.

[42] S. Luding. Towards dense, realistic granular media in 2D. *Nonlinearity*, 22(1):R101–R146, December 2009.

[43] N. Kumar, V. Magnanimo, M. Ramaioli, and S. Luding. Tuning the bulk properties of bidisperse granular mixtures by small amount of fines. *Powder Technology*, 293(C):94–112, May 2016.

[44] A. N. Lazaridi and V. F. Nesterenko. Observation of a new type of solitary waves in a one-dimensional granular medium. *Journal of Applied Mechanics and Technical Physics*, 26(3):405–408, 1985.

[45] S. Job, F. Santibanez, F. Tapia, and F. Melo. Nonlinear waves in dry and wet Hertzian granular chains. *Ultrasonics*, 48:506–514, 2008.

[46] C. Coste and B. Gilles. On the validity of Hertz contact law for granular material acoustics. *The European Physical Journal B-Condensed Matter and Complex Systems*, 7(1):155–168, 1999.

[47] C. Daraio, V. F. Nesterenko, E. B. Herbold, and S. Jin. Tunability of solitary wave properties in one-dimensional strongly nonlinear phononic crystals. *Phys. Rev. E*, 73(2):026610–10, February 2006.

[48] N. Boechler, J. Yang, G. Theocharis, P. G. Kevrekidis, and C. Daraio. Tunable vibrational band gaps in one-dimensional diatomic granular crystals with three-particle unit cells. *Journal of Applied Physics*, 109(7):074906–8, April 2011.

[49] F. Li, D. Ngo, J. Yang, and C. Daraio. Tunable phononic crystals based on cylindrical Hertzian contact. *Appl. Phys. Lett.*, 101(17):171903–5, October 2012.

[50] J. Cabaret, V. Tournat, and P. Béquin. Amplitude-dependent phononic processes in a diatomic granular chain in the weakly nonlinear regime. *Phys. Rev. E*, 86(4):041305, 2012.

[51] V. Tournat, V. E. Gusev, and B. Castagnède. Self-demodulation of elastic waves in a one-dimensional granular chain. *Phys. Rev. E*, 70(5):056603–14, November 2004.

[52] G. Theocharis, N. Boechler, P. G. Kevrekidis, S. Job, M. A. Porter, and C. Daraio. Intrinsic energy localization through discrete gap breathers in one-dimensional diatomic granular crystals. *Phys. Rev. E*, 82(5):056604–11, November 2010.

[53] G. James, P. G. Kevrekidis, and J. Cuevas. Breathers in oscillator chains with Hertzian interactions. *Physica D: Nonlinear Phenomena*, 251(0):39–59, 2013.

[54] S. Job, F. Melo, A. Sokolow, and S. Sen. How Hertzian Solitary Waves Interact with Boundaries in a 1D Granular Medium. *Phys. Rev. Lett.*, 94(17):178002–4, May 2005.

[55] S. Job, F. Melo, F. Santibanez, and F. Tapia. Nonlinear waves in Hertzian granular chains: Effects of inertial and stiffness heterogeneities. In *2007 ICU Vienna*. Vienna University of Technology, 2007.

[56] L. Ponson, N. Boechler, Y. M. Lai, M. A. Porter, P. G. Kevrekidis, and C. Daraio. Nonlinear waves in disordered diatomic granular chains. *Phys. Rev. E*, 82(2):021301–9, August 2010.

[57] V. F. Nesterenko, C. Daraio, E. B. Herbold, and S. Jin. Anomalous Wave Reflection at the Interface of Two Strongly Nonlinear Granular Media. *Phys. Rev. Lett.*, 95(15):158702–4, October 2005.

[58] I. D. Mayergoyz. Mathematical Models of Hysteresis. *Phys. Rev. Lett.*, 56(15):1518–1521, April 1986.

[59] V. Aleshin and K. Van Den Abeele. Preisach analysis of the Hertz–Mindlin system. *Journal of the Mechanics and Physics of Solids*, 57(4):657–672, April 2009.

[60] V. Tournat, V. E. Gusev, and B. Castagnède. Subharmonics and noise excitation in transmission of acoustic wave through unconsolidated granular medium. *Phys. Lett. A*, 326:340–348, June 2004.

[61] V. Tournat, C. Inserra, and V. Gusev. Non-cascade frequency-mixing processes for elastic waves in unconsolidated granular materials. *Ultrasonics*, 48(6-7):492–497, November 2008.

[62] H. Pichard, A. Duclos, J.-P. Groby, V. Tournat, and V. E. Gusev. Localized transversal-rotational modes in linear chains of equal masses. *Phys. Rev. E*, 89(1):013201, 2014.

[63] A.-C. Hladky-Hennion, G. Allan, and M. de Billy. Localized modes in a one-dimensional diatomic chain of coupled spheres. *Journal of Applied Physics*, 98(5):054909–8, September 2005.

[64] A.-C. Hladky-Hennion, J. Vasseur, B. Djafari-Rouhani, and M. de Billy. Sonic band gaps in one-dimensional phononic crystals with a symmetric stub. *Phys. Rev. B*, 77(1):104304, March 2008.

[65] A.-C. Hladky-Hennion, C. Granger, J. Vasseur, and M. de Billy. Propagation of elastic waves in one-dimensional periodic stubbed waveguides. *Phys. Rev. B*, 82(10):104307–7, September 2010.

[66] G. Theocharis, M. Kavousanakis, P. G. Kevrekidis, C. Daraio, M. A. Porter, and I. G. Kevrekidis. Localized breathing modes in granular crystals with defects. *Phys. Rev. E*, 80:066601, December 2009.

[67] N. Iikawa, M. M. Bandi, and H. Katsuragi. Sensitivity of Granular Force Chain Orientation to Disorder-Induced Metastable Relaxation. *Phys. Rev. Lett.*, 116(12):128001–5, March 2016.

[68] J. D. Joannopoulos. Self-assembly lights up. *Nature*, 414(6861):257–258, November 2001.

[69] M. Brzeziński, T. Biedroń, and A. Tracz. Spontaneous formation of colloidal crystals of PLA stereocomplex microspheres and their hierarchical structure. *MCP*, 215(1):27–31, 2014.

[70] I. S. Pavlov, A. I. Potapov, and G. A. Maugin. A 2D granular medium with rotating particles. *International Journal of Solids and Structures*, 43(20):6194–6207, October 2006.

[71] V. Tournat, I. Pèrez-Arjona, A. Merkel, V. Sanchez-Morcillo, and V. Gusev. Elastic waves in phononic monolayer granular membranes. *New Journal of Physics*, 13(7):073042, 2011.

[72] H. P. Rossmanith and A. Shukla. Photoelastic investigation of dynamic load transfer in granular media. *Acta Mechanica*, 42(3-4):211–225, 1982.

[73] A. Shukla, M. H. Sadd, Y. Xu, and Q. M. Tai. Influence of loading pulse duration on dynamic load transfer in a simulated granular medium. *Journal of the Mechanics and Physics of Solids*, 41(1):1795–1808, November 1993.

[74] S. Sen and R. S. Sinkovits. Sound propagation in impure granular columns. *Phys. Rev. E*, 54(6):6857–6865, December 1996.

[75] B. Gilles and C. Coste. Low-Frequency Behavior of Beads Constrained on a Lattice. *Phys. Rev. Lett.*, 90(17):174302–4, May 2003.

[76] A. Leonard, C. Daraio, A. Awasthi, and P. Geubelle. Effects of weak disorder on stress-wave anisotropy in centered square nonlinear granular crystals. *Phys. Rev. E*, 86(3):031305–10, September 2012.

[77] C. Daraio, D. Ngo, V. F. Nesterenko, and F. Fraternali. Highly nonlinear pulse splitting and recombination in a two-dimensional granular network. *Phys. Rev. E*, 82(3):036603–8, September 2010.

[78] D. Ngo, F. Fraternali, and C. Daraio. Highly nonlinear solitary wave propagation in Y-shaped granular crystals with variable branch angles. *Phys. Rev. E*, 85(3):036602–10, March 2012.

[79] L. Cai, J. Yang, P. Rizzo, X. Ni, and C. Daraio. Propagation of highly nonlinear solitary waves in a curved granular chain. *Granular Matter*, 15(3):357–366, 2013.

[80] A. Leonard, L. Ponson, and C. Daraio. Exponential stress mitigation in structured granular composites. *Extreme Mechanics Letters*, 1:23–28, December 2014.

[81] A. Leonard, F. Fraternali, and C. Daraio. Directional Wave Propagation in a Highly Nonlinear Square Packing of Spheres. *Exp. Mech.*, 53(3):327–337, October 2011.

[82] G. Wang, X. Wen, J. Wen, L. Shao, and Y. Liu. Two-Dimensional Locally Resonant Phononic Crystals with Binary Structures. *Phys. Rev. Lett.*, 93(15):154302–4, October 2004.

[83] H. Zhao, Y. Liu, G. Wang, J. Wen, D. Yu, X. Han, and X. Wen. Resonance modes and gap formation in a two-dimensional solid phononic crystal. *Phys. Rev. B*, 72(1):012301–4, July 2005.

[84] P. Peng, J. Mei, and Y. Wu. Lumped model for rotational modes in phononic crystals. *Phys. Rev. B*, 86:134304, 2012.

[85] A. Merkel. *Étude Théorique et Expérimentale de la Propagation Acoustique dans les Cristaux Phononiques Granulaires Tridimensionnels*. Thèse de Doctorat, Université du Maine, 2010.

[86] M. A. Koenders. The incremental stiffness of an assembly of particles. *Acta Mechanica*, 70(1-4):31–49, 1987.

[87] A. Suiker, R. De Borst, and C. S. Chang. Micro-mechanical modelling of granular material. Part 2: Plane wave propagation in infinite media. *Acta Mechanica*, 149:181–200, 2001.

[88] L. M. Schwartz, D. L. Johnson, and S. Feng. Vibrational Modes in Granular Materials. *Phys. Rev. Lett.*, 52(1):831–834, March 1984.

[89] A. S. J. Suiker, R. De Borst, and C. S. Chang. Micro-mechanical modelling of granular material. Part 1: Derivation of a second-gradient micro-polar constitutive theory. *Acta Mechanica*, 149(1-4):161–180, 2001.

[90] A. S. J. Suiker and R. de Borst. Enhanced continua and discrete lattices for modelling granular assemblies. *Philos Trans A Math Phys Eng Sci*, 363(1):2543–2580, November 2005.

[91] A. Suiker, A. V. Metrikine, and R. De Borst. Comparison of wave propagation characteristics of the Cosserat continuum model and corresponding discrete lattice models. *International Journal of Solids and Structures*, 38(9):1563–1583, 2001.

[92] S. A. Lisina, A. I. Potapov, and V. F. Nesterenko. A Nonlinear Granular Medium with Particle Rotation: A One-Dimensional Model. *Acoustical Physics*, 47(5):598–606, September 2001.

[93] O. Mouraille, W. A. Mulder, and S. Luding. Sound wave acceleration in granular materials. *Journal of Statistical Mechanics: Theory and Experiment*, 07(0):07023, July 2006.

[94] B. Velický and C. Caroli. Pressure dependence of the sound velocity in a two-dimensional lattice of Hertz-Mindlin balls: Mean-field description. *Phys. Rev. E*, 65(2):021307–14, January 2002.

[95] A. S. J. Suiker, A. V. Metrikine, and R. De Borst. Dynamic Behaviour of a Layer of Discrete Particles, Part 1: Analysis of Body Waves and Eigenmodes. *Journal of Sound and Vibration*, 240(1):1–18, February 2001.

[96] A. S. J. Suiker, A. V. Metrikine, and R. De Borst. Dynamic Behaviour of a Layer of Discrete Particles, Part 2: Response to a Uniformly Moving, Harmonically Vibrating Load. *Journal of Sound and Vibration*, 240(1):19–39, February 2001.

[97] O. Mouraille. *Sound propagation in dry granular materials: discrete element simulations, theory, and experiments*. Thèse de Doctorat, University of Twente, University of Twente, 2009.

[98] H. Pichard, A. Duclos, J.-P. Groby, V. Tournat, and V. E. Gusev. Two-dimensional discrete granular phononic crystal for shear wave control. *Phys. Rev. B*, 86:134307, October 2012.

[99] L.-Y. Zheng, H. Pichard, V. Tournat, G. Theocharis, and V. Gusev. Zero-frequency and slow elastic modes in phononic monolayer granular membranes. *Ultrasonics*, pages 1–14, November 2015.

[100] A. Merkel, V. Tournat, and V. Gusev. Dispersion of elastic waves in three-dimensional noncohesive granular phononic crystals: Properties of rotational modes. *Phys. Rev. E*, 82(3):031305, 2010.

[101] E. Dintwa, E. Tijskens, and H. Ramon. On the accuracy of the Hertz model to describe the normal contact of soft elastic spheres. *Granular Matter*, 10(3):209–221, November 2007.

[102] R. D. Mindlin. Compliance of elastic bodies in contact. *ASME J. Appl. Mech.*, 16:259–268, 1949.

[103] R. D. Mindlin and H. Deresiewica. Elastic spheres in contact under varying oblique forces. *ASME J. Appl. Mech.*, 75:327–342, 1953.

[104] J. Duffy and R. D. Mindlin. Stress-Strain Relations and Vibrations of a Granular Medium. *ASME J. Appl. Mech.*, 24:585–593, 1958.

[105] K. L. Johnson. *Contact Mechanics*. Cambridge University Press, 1985.

[106] A. Pankov. *Travelling Waves And Periodic Oscillations In Fermi-pasta-ulam Lattices*. World Scientific, Singapore, 2005.

[107] S. Flach and A. Gorbach. Discrete breathers in Fermi Pasta Ulam lattices. *Chaos: An Interdisciplinary Journal of Nonlinear Science*, 15(1):015112, 2005.

[108] G. James and P. Noble. Breathers on diatomic Fermi-Pasta-Ulam lattices. *Physica D: Nonlinear Phenomena*, 196(1):124–171, September 2004.

[109] L. Brillouin. *Wave Propagation in Periodic Structures: Electric Filters and Crystal Lattices*. Dover books on engineering and engineering physics. Dover, 1953.

[110] M. Molerón, A. Leonard, and C. Daraio. Solitary waves in a chain of repelling magnets. *Journal of Applied Physics*, 115(18):4901, 2014.

[111] B. P. Bernard, B. A. M. Owens, and B. P. Mann. Uncertainty Propagation in the Band Gap Structure of a 1D Array of Magnetically Coupled Oscillators. *J. Vib. Acoust.*, 135(4):041005, August 2013.

[112] F. M. Russell, Y. Zolotaryuk, J. C. Eilbeck, and T. Dauxois. Moving breathers in a chain of magnetic pendulums. *Phys. Rev. B*, 55(1):6304–6308, March 1997.

[113] A. Mehrem, N. Jiménez, L. Salmerón-Contreras, X. García-Andrés, L. M. García-Raffi, R. Picó, and V. Sánchez-Morcillo. Nonlinear dispersive waves in repulsive lattices. *arXiv*, page preprint arXiv:1703.03628., March 2017.

[114] J. O. Vasseur, O. B. Matar, J. F. Robillard, A. C. Hladky-Hennion, and P. A. Deymier. Band structures tunability of bulk 2D phononic crystals made of magneto-elastic materials. *AIP Advances*, 1(4):041904–13, 2011.

[115] O. Bou Matar, J. F. Robillard, J. O. Vasseur, A. C. Hladky-Hennion, P. A. Deymier, P. Pernod, and V. Preobrazhensky. Band gap tunability of magneto-elastic phononic crystal. *Journal of Applied Physics*, 111(5):054901–15, 2012.

[116] F. J. Sierra-Valdez, F. Pacheco-Vázquez, O. Carvente, F. Malloggi, J. Cruz-Damas, R. Rechtman, and J. C. Ruiz-Suárez. Acoustic gaps in a chain of magnetic spheres. *Phys. Rev. E*, 81(1):011301–4, January 2010.

[117] A. Mehdizadeh, R. Mei, J. F. Klausner, and N. Rahmatian. Interaction forces between soft magnetic particles in uniform and non-uniform magnetic fields. *Acta Mechanica Sinica*, 2010.

[118] T. Fujita and M. Mamiya. Interaction forces between nonmagnetic particles in the magnetized magnetic fluid. *Journal of Magnetism and Magnetic Materials*, 65(2-3):207–210, 1987.

[119] J. M. D. Coey. *Rare-earth iron permanent magnets*. Oxford University Press, 2016.

[120] R. Fuchs, T. Weinhart, J. Meyer, H. Zhuang, T. Staedler, X. Jiang, and S. Luding. Rolling, sliding and torsion of micron-sized silica particles: experimental, numerical and theoretical analysis. *Granular Matter*, 16(3):281–297, 2014.

[121] L. Bureau, C. Caroli, and T. Baumberger. Elasticity and onset of frictional dissipation at a non-sliding multi-contact interface. *Proceedings of the Royal Society A: Mathematical, Physical and Engineering Sciences*, 459(2039):2787–2805, November 2003.

[122] T. Baumberger and C. Caroli. Solid friction from stick–slip down to pinning and aging. *Advances in Physics*, 55(3-4):279–348, May 2006.

[123] R. P. Moiseyenko and V. Laude. Material loss influence on the complex band structure and group velocity in phononic crystals. *Phys. Rev. B*, 83(6):064301, February 2011.

[124] G. Theocharis, O. Richoux, V. Romero-Garcia, A. Merkel, and V. Tournat. Limits of slow sound propagation and transparency in lossy, locally resonant periodic structures. *New Journal of Physics*, 16(9):093017, September 2014.

[125] A. Geslain, S. Raetz, M. Hiraiwa, M. Abi Ghanem, S. P. Wallen, A. Khanolkar, N. Boechler, J. Laurent, C. Prada, A. Duclos, P. Leclaire, and J.-P. Groby. Spatial Laplace transform for complex wavenumber recovery and its application to the analysis of attenuation in acoustic systems. *Journal of Applied Physics*, 120(13):135107–9, October 2016.

[126] S. N. Gurbatov, O. V. Rudenko, and A. I. Saichev. *Waves and Structures in Nonlinear Nondispersive Media: General Theory and Applications to Nonlinear Acoustics*. Nonlinear Physical Science. Springer, Berlin, 2012.

[127] V. J. Sanchez-Morcillo, I. Perez-Arjona, V. Romero-Garcia, V. Tournat, and V. E. Gusev. Second-harmonic generation for dispersive elastic waves in a discrete granular chain. *Phys. Rev. E*, 88:043203, October 2013.

[128] G. Kuwabara and K. Kono. Restitution coefficient in a collision between two spheres. *Japanese Journal of Applied Physics*, 26(Part 1, No. 8):1230–1233, 1987.

[129] N. V. Brilliantov, F. Spahn, J.-M. Hertzsch, and T. P oschel. Model for collisions in granular gases. *Phys. Rev. E*, 53:5382–5392, May 1996.

[130] N. V. Brilliantov, A. V. Pimenova, and D. S. Goldobin. A dissipative force between colliding viscoelastic bodies: Rigorous approach. *EPL*, 109(1):14005, January 2015.

[131] V. Tournat, V. E. Gusev, V. Y. Zaitsev, and B. Castagnède. Acoustic second-harmonic generation with shear to longitudinal mode conversion in granular media. *EPL*, 66(6):798–804, January 2007.

[132] S. P. Wallen and N. Boechler. Shear to longitudinal mode conversion via second harmonic generation in a two-dimensional microscale granular crystal. *Wave Motion*, 68:22–30, January 9999.

[133] A. Novak, P. Lotton, and L. Simon. Dynamic measurement of loudspeaker suspension parameters using an active harmonic control technique. *Audio Engineering Society Convention 136*, 2014.

UNIVERSITE BRETAGNE LOIRE

Université du Maine

Thèse de Doctorat

Florian Allein

Linear and Nonlinear Waves in Magneto-Granular Phononic Structures: Theory and Experiments

Propagation d'Ondes Linéaires et Non Linéaires dans les Structures Phononiques Magnéto-Granulaires : Théories et Expériences

Résumé

Les cristaux granulaires sont des arrangements périodiques ou structurés de particules élastiques en contact. Ce travail de thèse porte sur l'étude théorique et expérimentale de la propagation d'ondes élastiques à travers de telles structures.
Un cristal granulaire unidimensionnel composé d'une chaîne de billes d'acier couplées à des aimants permanents fixes est tout d'abord étudié. Les forces statiques de contact entre les billes, déterminantes pour les caractéristiques de la propagation et la dispersion des ondes élastiques, sont créées par le champ magnétique des aimants. Cette configuration permet donc d'adapter la réponse dynamique du milieu en modifiant les forces magnétiques des aimants. Un modèle linéaire prenant en compte tous les degrés de liberté en translations et rotations des billes et les couplages élastiques (longitudinal, de cisaillement et de torsion) entre billes et entre les billes et un substrat est développé. Il permet d'obtenir les relations de dispersion des modes de propagation dans ce système en fonction des différents paramètres de couplage. Les expériences réalisées mettent en évidence la propagation de modes élastiques avec micro-rotation des billes et démontrent la pertinence du modèle pour la description de ce système. Plusieurs effets de dispersion intéressants sont observés et discutés, modes à vitesse de groupe nulle, modes mous...
Dans un second temps, une étude prenant en compte les non-linéarités de contact permet de prédire et d'observer expérimentalement la génération d'harmonique, le filtrage d'harmoniques ainsi que la conversion de modes longitudinaux vers des modes couplés de translation-rotation dans des structures granulaires s'écartant des chaines unidimensionnelles simples.
Ces travaux ouvrent des perspectives intéressantes pour le contrôle d'ondes élastiques, dans le régime non linéaire, avec des structures granulaires architecturées.

Mots-clés

cristal phononique granulaire, modes rotationnels, non-linéarité, structures granulaires, contrôle d'ondes.

Abstract

Granular crystals are periodic or structured arrangements of elastic particles in contact. This work is devoted to theoretical and experimental study of the elastic wave propagation through such structures.
A one-dimensional granular crystal composed of steel spherical beads coupled to permanent magnets placed in a substrate is first studied. Static forces at the contact between beads, determining the wave propagation and dispersion characteristics, are induced by the magnetic field from the magnets. This configuration enables tuning the dynamic response of the chain by modifying the magnetic strength of the magnets. A linear model taking into account all degrees of freedom of the beads (three translations and three rotations) as well as all elastic couplings (longitudinal, shear and torsional), between the beads and between the beads and the substrate is developed. This model provides the dispersion relations of the modes in the system for different coupling parameters. The associated experiments confirm the elastic propagation of modes with micro-rotation of beads and demonstrate the pertinence of the model for the system description. Several interesting effects on the dispersion are observed and discussed, zero group velocity modes, soft modes...
In a second part, we take into account the nonlinearities originating from the contacts to predict and then observe experimentally the second harmonic generation. The filtering of harmonics along with conversion from longitudinal to coupled transversal-rotational modes in granular structures, is also observed for a configuration deviating from simple one-dimensional chains. This work opens the way for interesting applications in elastic wave control, in the nonlinear regime, with structured granular devices.

Keywords

granular phononic crystal, rotational modes, nonlinearity, granular structures, wave control.